UNIVERSITY OF Southampton

Faculty of Engineering and Physical Sciences
School of Physics and Astronomy

Coherent Networks of Polariton Condensates in Microcavities

Julian Dominic Töpfer

A thesis for the degree of
Doctor of Philosophy

October 2021

University of Southampton

Abstract

Faculty of Engineering and Physical Sciences
School of Physics and Astronomy

Doctor of Philosophy

Coherent Networks of Polariton Condensates in Microcavities

by Julian Dominic Töpfer

The study of interacting many-element systems is as vital for our understanding of complex organisms, as it is important for the modelling of disease spreading in pandemics, and is a key element in the search for materials with novel properties. The presence of nonlinearities and interaction time-lags critically influences the dynamics and complicates control over these systems. Moreover, complexity in network structures rapidly scales with a larger number of elements and increasing degrees of freedom, often making them computationally intractable.
Artificially engineered networks, on the other hand, can be used for the simulation and study of interacting systems, and pave the way for novel and unconventional computing paradigms. The implementation of these schemes is being explored in various fields such as electronics, photonics and quantum systems. In particular, lattices of polariton condensates in optical microcavities present a promising platform for the realisation of coupled network structures. Microcavity polaritons are light-weight bosonic quasi-particles formed by the strong coupling of cavity photons and quantum well excitons. Their hybrid light-matter character facilitates macroscopically accessible quantum degenerate states (condensates) at elevated temperatures. Large optical malleability, picosecond-timescale dynamics, and strong intrinsic nonlinearities highlight the potential of polariton lattices for future technological applications.
The work presented in this PhD thesis investigates the interactions of coupled polariton condensates, and shows substantial advancements in both, the engineering and the manipulation of optically generated condensate lattices. In particular, the introduction of a laser feedback scheme for condensate density stabilisation makes it possible to accurately build macroscopic lattices of tuneable size and network architecture. The nonlinear dynamics and synchronisation phenomena of coupled condensates are explored in various coupling topologies, ranging from simply-connected structures to one- and two-dimensional periodic systems. Shaping of the polariton potential landscape by using spatially patterned lasers opens up an all-optical method of controlling couplings, interaction time-lags, and coherence properties in condensate lattices. The results and methods presented support the realisation of an ultra-fast delay-coupled nonlinear oscillator network, with precise control over individual couplings.

Contents

List of Figures

Declaration of Authorship

I declare that this thesis and the work presented in it is my own and has been generated by me as the result of my own original research.

I confirm that:

1. This work was done wholly or mainly while in candidature for a research degree at this University;
2. Where any part of this thesis has previously been submitted for a degree or any other qualification at this University or any other institution, this has been clearly stated;
3. Where I have consulted the published work of others, this is always clearly attributed;
4. Where I have quoted from the work of others, the source is always given. With the exception of such quotations, this thesis is entirely my own work;
5. I have acknowledged all main sources of help;
6. Where the thesis is based on work done by myself jointly with others, I have made clear exactly what was done by others and what I have contributed myself;
7. Parts of this work have been published as:
   J. D. Töpfer, et al., Communications Physics **3**, 2 (2020)
   S. Alyatkin, et al., Physical Review Letters **124**, 207402 (2020)
   J. D. Töpfer, et al., Optica **8**, 106-113 (2021)

Signed:..... Date:.....

Publications

- J. D. Töpfer, H. Sigurdsson, L. Pickup, P. G. Lagoudakis, *Time-delay polaritonics*, Communications Physics **3**, 2 (2020)
- S. Alyatkin, J. D. Töpfer, A. Askitopoulos, H. Sigurdsson, P. G. Lagoudakis, *Optical control of couplings in polariton condensate lattices*, Physical Review Letters **124**, 207402 (2020)
- J. D. Töpfer, S. Alyatkin, H. Sigurdsson, P. G. Lagoudakis, *Lotka-Volterra population dynamics in coherent and tunable oscillators of trapped polariton condensates*, Physical Review B **102**, 195428 (2020)
- J. D. Töpfer, I. Chatzopoulos, H. Sigurdsson, T. Cookson, Y. G. Rubo, P. G. Lagoudakis, *Engineering spatial coherence in lattices of polariton condensates*, Optica **8**, 106-113 (2021)
- L. Pickup, J. D. Töpfer, H. Sigurdsson, P. G. Lagoudakis, *Polariton spin jets through optical control*, Physical Review B **103**, 155302 (2021)
- T. Cookson, K. Kalinin, H. Sigurdsson, J. D. Töpfer, S. Alyatkin, M. Silva, W. Langbein, N. G. Berloff, P. G. Lagoudakis, *Geometric frustration in polygons of polariton condensates creating vortices of varying topological charge*, Nature Communications **12**, 2120 (2021)
- S. Alyatkin, H. Sigurdsson, A. Askitopoulos, J. D. Töpfer, P. G. Lagoudakis, *Quantum fluids of light in all-optical scatterer lattices*, Nature Communications **12**, 5571 (2021)
- I. Gnusov, H. Sigurdsson, J. D. Töpfer, S. Baryshev, P. G. Lagoudakis, *All-optical linear-polarization engineering in single and coupled exciton-polariton condensates*, Physical Review Applied **16**, 034014 (2021)

Abbreviations

AOM	Acousto optic modulator
BEC	Bose Einstein condensate
BS	Beam splitter
CCD	Charge-coupled device
cw	Continuous wave
DBR	Distributed Bragg reflector
FFT	Fast Fourier transform
FSR	Free spectral range
FWHM	Full width at half maximum
GPE	Gross-Pitaevski equation
GPU	Graphics processing unit
GS	Gerchberg-Saxton
IFFT	Inverse fast Fourier transform
LP	Lower polariton branch
MO	Microscope objective
NA	Numerical aperture
NN	Nearest neighbour
ODLRO	Off-diagonal long-range order
PL	Photoluminescence
PSD	Power spectral density
QW	Quantum well
RSD	Relative standard deviation
SLM	Spatial light modulator
UP	Upper polariton branch
VCSEL	Vertical-cavity surface-emitting laser

Chapter 1

Introduction

While we have found efficient ways to describe the motion of a pendulum in a gravitational field or the bound state formed between a proton and an electron, the analysis of real-world structures is often much more complicated as they are formed by many interacting elements. Such structures with many degrees of freedom are omnipresent throughout nature and technology and appear on both, macroscopic (classical) and microscopic (quantum) scales. Their study is therefore, of crucial importance for the description of solid-state physical systems, our understanding of neurological systems, the modelling of socio-biological systems, the forecasting of financial markets, and the managing of power grids. These systems often exhibit nonlinearities and interaction time-lags, which can lead to chaotic behaviour and further complicate the dynamics [1, 2]. As a matter of fact, an exponential growth of necessary computer resources with increasing number of elements (as in the case of quantum many-body systems) can make these systems computationally intractable [3].

Despite their enormous complexity there are however, situations when the dynamical state of a many-element system is greatly simplified by the emergence of dynamical order [4]. In particular, the build-up of rigid correlations between individual constituents can lead to the emergence of a collective state, a process that is commonly referred to as synchronisation. In the simplest case, the dynamics of all elements then becomes identical and the system is said to be fully synchronised. The phenomenon of synchronisation plays a universal role in nature and science; it describes e.g. the picturesque setting of firefly populations flashing in unison, and the functioning of a pacemaker cell to induce a rhythmic heart beat [5].

Besides its wide-spread occurrence in macroscopic classical systems the spontaneous formation of order can also be found in quantum many-body systems consisting of identical bosonic particles. In equilibrium systems the transition from incoherence to coherence is typically controlled by a reduction in temperature and results in the massive occupation of a single quantum state. The spatial expansion of quantum behaviour

onto macroscopic scales is a fascinating subject and has attracted much research in the past century. Prime examples of experiments demonstrating the emergence of macroscopic order at low temperatures are the superfluid phase transition of liquid helium [6, 7], the superconducting phase transition of weakly-bound electron pairs [8], and Bose-Einstein condensation of dilute atomic gases [9, 10].

In the past two decades, exciting directions of macroscopic quantum phenomena under nonequilibrium settings have also been explored in optical microcavities embedded with quantum wells [11]. Progressed fabrication processes have made it possible to enter the regime of strong coupling between quantum well excitons and cavity photons in high-quality microcavities [12], and results in the formation of half-light, half-matter bosonic quasi-particles called polaritons [13]. Owing to their hybrid character, polaritons inherit particle properties from both of their constituents. While their excitonic component facilitates strong nonlinear interactions, their photonic components makes polaritons extremely light quasi-particles ($m \approx 10^{-5} m_e$) with short radiative lifetimes $\tau \approx 1 - 100$ ps. One of their great advantages is that due to their light weight, polaritons are expected to have a much higher critical temperature for reaching condensation than, for instance, atomic gases. Indeed the first demonstrations of a power-driven bosonic phase transition of microcavity polaritons were realised under optical pumping and at cryogenic temperatures $T \approx 10$ K [14, 15]. Amongst other things, this phase transition is described by the spontaneous build-up of coherence and the formation of a macroscopically populated quantum state; the polariton condensate. Like in the case of a laser, the finite cavity losses of a polariton condensate results in the emission of coherent light. The system, therefore often termed polariton laser [16], presents an exciting platform for opto-electronic applications with strong intrinsic nonlinearities [17]. Importantly, polariton condensation has also been demonstrated under electrical injection [18] and at room-temperature in wide-bandgap semiconductor materials [19, 20] and organic structures [21, 22], highlighting the prospect of future polariton devices operating under ambient conditions.

The short radiative lifetime makes polariton condensates an inherent dissipative system, that requires continuous (optical or electrical) pumping to replenish particles leaking out of the cavity. These optical losses, however, enable continuous characterisation of the polariton system (density, momentum, spin, energy, coherence properties) by means of conventional optical measurements. The ease in generation, manipulation, and optical read-out of polariton condensates is one of the striking advantages in terms of technical feasibility. In fact, in the past two decades a plethora of fascinating macroscopic phenomena have been demonstrated in experiments, such as superfluid behaviour [23], quantised vortices [24], propagating solitons [25], bosonic Josephson junctions [26, 27], and others [11].

The experimental accessibility of macroscopic quantum phenomena (e.g. in cold atom

systems or semiconductor microcavities) has further led to implementations of interacting particles in artificial lattices structures, and offers possibilities to study quantum phase transitions and exotic states of matter [28]. As an exciting new direction, the engineering of bosonic many-body systems in controllable potential structures also presents an experimental platform for the realisation of analogue (quantum) simulators [29, 30]. Hereby, a quantum system with controllable network architecture and interactions can be realised in order to emulate computationally intractable problems, such as beforementioned complex many-body systems.

The structuring of synthetic networks and lattices in polariton condensates is typically accomplished by lateral patterning of the microcavity structure during fabrication [31, 32] or, alternatively, by using spatially patterned laser beams to dynamically induce optically formed potentials [33, 34, 35]. Studies on polariton lattices have demonstrated a diverse range of applications, such as the formation of excited state condensates [31, 36], the realisation of topological lasers [37] and topological insulators [38], neuro-inspired computing schemes [39], optically-tunable bandstructures [40], and applications for the simulation of nonlinear oscillator models [41, 42, 43].

This PhD thesis details on the all-optical engineering of polariton condensates in networks and lattices. Experimental advancements in design and manipulation of coupled condensate structures allow the flexible generation of macroscopic lattices, and facilitate precise control over the system's coherence properties. The coupling dynamics of polariton condensates is tunable via optical patterning of the non-Hermitian potential landscape, and makes it possible to explore synchronisation and non-stationary dynamical regimes in structured many-body systems. The results, which are schematically summarised in Fig. 1.1, demonstrate that optically engineered polariton lattices have the potential to emulate networks of delay-coupled nonlinear oscillators with control over individual couplings. The techniques developed present a general toolbox for the optical sculpting of driven-dissipative lattices, with applications in lattices of polariton and photon condensates, and in laser arrays.

Chapter 2 provides a brief introduction into the vast field of nonlinear dynamical systems. In particular, the coupling and synchronisation dynamics of general nonlinear oscillators are described. Effects of frequency detuning and time-delayed coupling are discussed and shown to play a crucial role in the formation of coherence and dynamical stability of coupled nonlinear oscillatory systems. The concepts and phenomena introduced in this first part are essential for the discussion of synchronisation phenomena in polariton lattices presented throughout this thesis.

Next, fundamentals of polaritons and the formation of macroscopic quantum phenomena in semiconductor microcavities are presented in Chapter 3. In detail, the strong

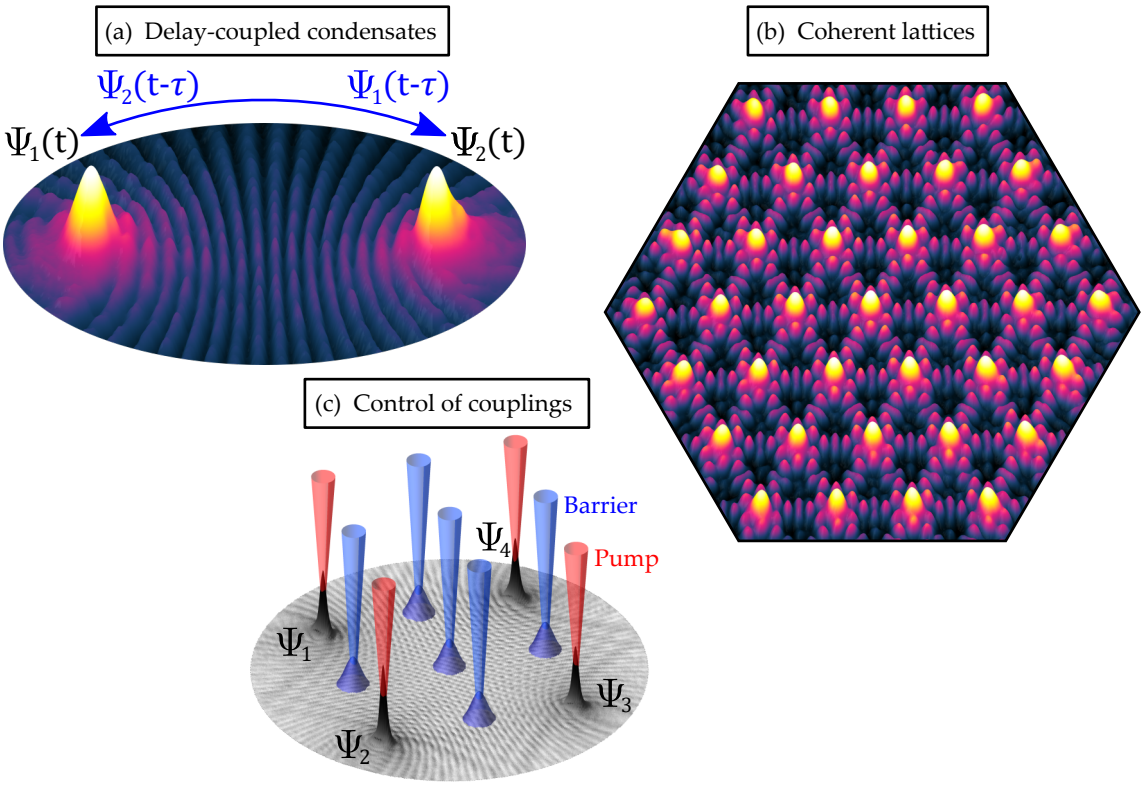

FIGURE 1.1: **Engineering coherence in networks of coupled polariton condensates.** Advanced optical methods facilitate the generation of (a) polariton condensates with time-delayed coupling, (b) macroscopically coherent condensate lattices, and (c) all-optical control over individual couplings via implementation of optical barriers.

coupling regime and hybridisation of photonic and excitonic resonances in microcavities are introduced, and the power-driven bosonic phase transition of a polariton condensate is described. The Chapter further details on characteristics of non-resonantly excited polariton condensates, and discusses measures for the system's finite coherence properties.

Experimental methods for optical excitation and measurement of polariton lattices are given in Chapter 4. Focus is put on the developed closed-loop feedback technique for the stabilisation of particle densities across networks and lattices of polariton condensates. The method allows to counteract experimental aberrations and facilitates the generation of flexible geometries with striking homogeneity. Furthermore, methods for the measurement of temporal and spatial correlations in networks of coupled polariton condensates are presented.

Chapter 4 details on the properties of a single (ballistically expanding) polariton condensate and, subsequently, unravels the coupling and dynamics of two condensates [see Fig. 1.1(a)]. In particular, spectral features and coherence properties of two condensates are studied, and shown to posses universal characteristics of time-delayed coupled nonlinear oscillators. A delay-coupled oscillator model is introduced and fully

reproduces the experimentally observed dynamical features and synchronisation phenomena of ballistically coupled polariton condensates.

The engineering and in-depth characterisation of macroscopic polariton lattices is then demonstrated in Chapter 6. Importantly, the applied optical stabilisation of particle densities [see Fig. 1.1(b)] is shown to significantly increase the spatial coherence properties in polariton lattices, and results in the formation of near-diffraction limited cavity emission. Active compensation of system aberrations allows to accurately study the coherence properties of coupled condensate structures for varying network architectures. The study reveals that dimensionality and connectivity critically affect coherence and power consumption in polariton lattices.

Chapter 7 introduces an experimental method for all-optical control over couplings in lattices of polariton condensates. The method utilises optical injection of potential barriers in-between ballistically coupled condensate nodes [see Fig. 1.1(c)] for accurate control over inter-condensate particle flows. The effect is strong enough to significantly alter the synchronous phases between two condensates, inducing parity flip transitions, as well as the emergence of non-stationary periodic states. The system dynamics can be described by a delay-coupled oscillators model with variable coupling phases. Optical control over couplings is further demonstrated in larger one- and two-dimensional lattices, and proofs the scalability and flexibility of the presented technique.

Chapter 2

Coupling And Synchronisation Of Nonlinear Oscillators

Periodic oscillatory motion of one or multiple interconnected units is an ubiquitous phenomenon in nature and technology. While the periodic motion of a mechanical pendulum serves as the timekeeping element in a clock, the periodic and synchronous firing of neurons determines the neurological functioning of brains [5]. The linear harmonic oscillator is a universal model for the description of small amplitude oscillators. In such system's the amplitude is determined by initial conditions, e.g. the initial spatial displacement of a pendulum, and the oscillation frequency is independent of the amplitude. In nonlinear systems, however, the amplitude is self-regulating and the oscillation frequency is generally amplitude-dependent. Examples of nonlinear oscillatory systems are electromagnetic fields in laser cavities, superconducting Josephson junctions and predator-prey cycles [1, 5]. Just as the harmonic oscillator constitutes a universal model for linear oscillators, the Stuart Landau equation represents a universal mathematical model to describe weakly nonlinear oscillators close to the onset of oscillations [44].

The scope of this Chapter is to present the basics and dynamical regimes of coupled nonlinear oscillators, thus giving the basis for the analysis of coupled exciton-polariton condensates presented in this thesis. We begin our discussion by introducing the Stuart-Landau equation describing the state of a single nonlinear oscillator. Next we describe that, in the regime of weak coupling, two such coupled nonlinear oscillators can be reduced to a system of coupled phase oscillators. The appearing synchronised and desynchronised regimes of two coupled oscillators are discussed and effects of time delayed coupling are presented.

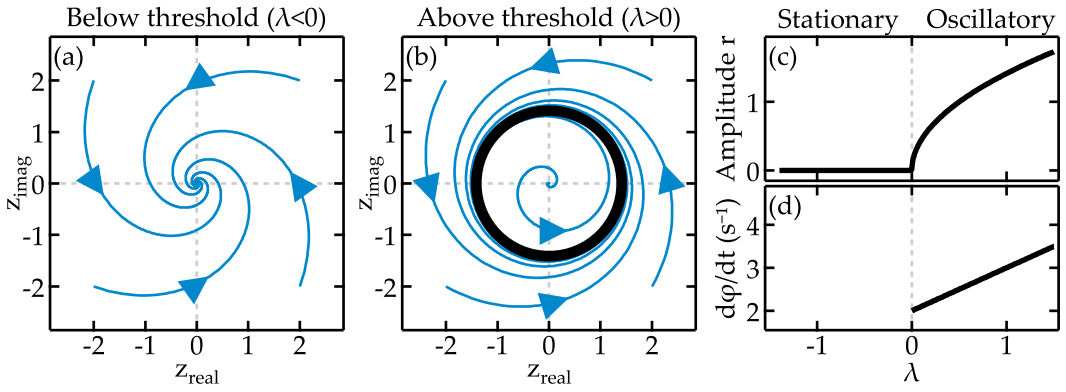

FIGURE 2.1: **A nonlinear Stuart-Landau oscillator.** Phase-space diagrams of the Stuart Landau equation in the complex plane with (a) negative gain and (b) positive gain. The ocurring stable limit cycle for the case of positive gain can be described by a non-vanishing oscillation ampitude $r = |z|$ and an oscillation frequency $\mathrm{d}\phi/\mathrm{d}t$ as shown in (c) and (d). Simulation parameters: $\omega = 2\ \mathrm{s}^{-1}$, $\sigma = 0.5\ \mathrm{s}^{-1}$, $\gamma = 1\ \mathrm{s}^{-1}$ and $\lambda = -1\ \mathrm{s}^{-1}$ for (a) and $\lambda = +1\ \mathrm{s}^{-1}$ for (b).

2.1 Stuart-Landau Oscillator

In the following, we consider a single nonlinear oscillatory system whose state can be described by amplitude r and phase ϕ, or alternatively in complex notation $z = r\exp(i\phi)$. The time-dynamics of this system is goverened by the Stuart-Landau equation,

$$\dot{z} = \left[\lambda + i\omega - (\sigma - i\gamma)\,|z|^2\right] z, \tag{2.1}$$

where the four parameters λ, ω, σ and γ are real-valued. The meaning of these parameters becomes evident when rewriting Eq. 2.1 in polar coordinates,

$$\dot{r} = \lambda r - \sigma r^3, \tag{2.2a}$$

$$\dot{\phi} = \omega + \gamma r^2. \tag{2.2b}$$

While the effective gain $\lambda > 0$ drives an increase in amplitude r, the parameter $\sigma > 0$ leads to a nonlinear gain saturation in the system preventing the amplitude from growing indefinitely. The parameter γ causes a nonlinear modification of the system's oscillation frequency deviating from its natural (small-amplitude) frequency ω.
We only consider the case of positive gain saturation $\sigma > 0$ and determine the system's fixed amplitude points $\dot{r} = 0$ from Eq. 2.2a. For negative gain, i.e. $\lambda < 0$, the Stuart Landau equation has one stable solution given by the equilibrium point $r^{(\mathrm{st})} = 0$. In Fig. 2.1(a) the system's phase-space diagram is shown illustrating the attraction of the origin. However, for $\lambda > 0$ the origin becomes unstable and instead a stable periodic orbit with amplitude $r^{(\mathrm{st})} = \sqrt{\lambda/\sigma}$ and constant phase oscillation frequency $\dot{\phi}^{(\mathrm{st})}$ emerges. Under this latter condition, the dynamical system described in Eq. 2.1 is named Stuart Landau oscillator. Trajectories in phase-space displayed in Fig. 2.1(b)

show attraction to the stable limit cycle (black circle). All orbits except the one starting at the origin converge to the limit cycle for $t \to \infty$. The increase of the limit cycle radius $r^{(\mathrm{st})}$ and oscillation frequency $\dot{\phi}^{(\mathrm{st})}$ of the Stuart-Landau oscillator with growing effective gain $\lambda > 0$ are illustrated in Fig. 2.1(c) and (d).
Besides its universality for the description of single nonlinear oscillators, the Stuart-Landau oscillator presents a paradigm to describe coupled nonlinear systems with a plethora of dynamical effects [45, 46, 47]. Of particular interest for the studies presented in this thesis is the weak mutual coupling of two or more oscillators leading to synchronisation of their periodic orbits.

2.2 Definition of Synchronisation

Synchronisation describes the phenomenon of adjustment of oscillatory motion of two or more oscillators due to their coupling [5]. This effect was already studied in the 17th century by Christiaan Huygens, the inventor of the pendulum clock, who observed that two clocks hanging from a common frame tend to swing at the same frequency yet 180° out of phase [48]. Similarly, synchrony is observed between two metronomes placed on a moveable base [49] as illustrated in Fig. 2.2(a). In this configuration the small motion of the base couples the metronomes and, for small intrinsic frequency differences, causing synchronisation with nearly vanishing phase difference.
When describing two oscillators with intrinsic (uncoupled) frequencies ω_1 and ω_2 we call their coupled system synchronised if both oscillators oscillate at the same frequency due to their coupling, i.e. $\dot{\phi}_1 = \dot{\phi}_2$. On the other hand, if the two units oscillate at different frequencies the system is termed unsynchronised. The tendency for the two oscillators to synchronise depends on both their frequency detuning $\omega_1 - \omega_2$ and their mutual coupling strength. A larger coupling strength generally enables synchronisation for a larger range of frequency detunings. When synchronisation between two coupled oscillators occurs and their phase difference $\phi_{12} = \phi_1 - \phi_2$ remains stable at a definite preferred value against perturbations we denote the system as phase-locked. Phase-locking of two oscillators with vanishing phase difference $\phi_{12} = 0$ is named in-phase synchronisation and phase-locking with $\phi_{12} = \pi$ is named anti-phase synchronisation.

2.3 Two coupled oscillators

Two symmetrically coupled Stuart Landau oscillators can be described by introducing a real-valued linear coupling term J,

$$\dot{z}_1 = \left[\lambda_1 + i\omega_1 - (\sigma_1 - i\gamma_1)\,|z_1|^2\right] z_1 + J z_2, \tag{2.3a}$$

$$\dot{z}_2 = \left[\lambda_2 + i\omega_2 - (\sigma_2 - i\gamma_2)\,|z_2|^2\right] z_2 + J z_1. \tag{2.3b}$$

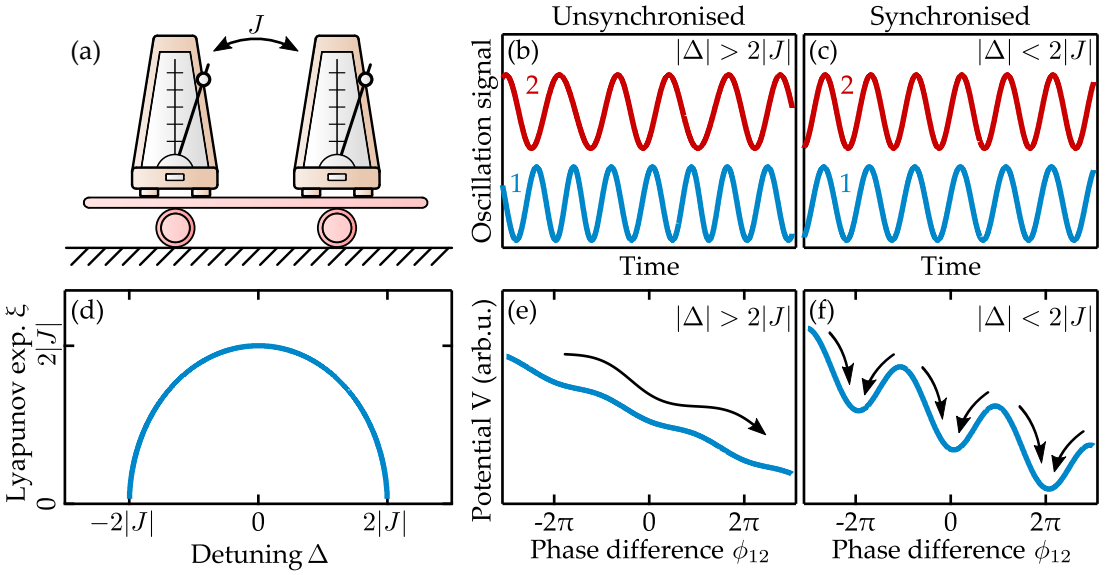

FIGURE 2.2: **Synchronisation of two weakly coupled phase oscillators.** (a) Schematic of two metronomes weakly coupled through a moveable base. (b) When the frequency detuning Δ of the two phase oscillators is too large then no synchronisation is possible. (c) When the coupling strength $|J|$ is large enough to compensate for the oscillators' intrinsic detuning synchronisation is possible and the phase difference $\phi_{12}(t)$ is constant. (d) Lyapunov exponent ξ for varying detuning Δ between the phase oscillators. (e,f) Potential function $V(\phi_{12})$ (Eq. 2.8) in the (e) desynchronised and (f) synchronised regime. The system's descent to lower potential energy is depicted with black arrows.

While this coupled oscillator system features in general complex dynamics [50], the system's degrees of freedom can effectively be reduced to phase dynamics in the case of weak coupling. Hence, we rewrite the coupled oscillator Eqs. 2.3 in polar coordinates,

$$\dot{r}_1 = \lambda_1 r_1 - \sigma_1 r_1^3 + J r_2 \cos(\phi_2 - \phi_1), \tag{2.4a}$$

$$\dot{r}_2 = \lambda_2 r_2 - \sigma_2 r_2^3 + J r_1 \cos(\phi_1 - \phi_2), \tag{2.4b}$$

$$\dot{\phi}_1 = \omega_1 + \gamma_1 r_1^2 + J\frac{r_2}{r_1}\sin(\phi_2 - \phi_1), \tag{2.4c}$$

$$\dot{\phi}_2 = \omega_2 + \gamma_2 r_2^2 + J\frac{r_1}{r_2}\sin(\phi_1 - \phi_2). \tag{2.4d}$$

Without coupling, $J = 0$, each isolated oscillator has a stable limit cycle with constant amplitude $r_{1,2}$ and natural intrinsic frequency $\tilde{\omega}_{1,2} = \omega_{1,2} + \gamma_{1,2} r_{1,2}^2$. In the following we consider the case of weakly coupled oscillators, i.e. small coupling parameter $|J| \ll \lambda_{1,2}$. In this case the amplitude of each oscillator is approximately constant and equal to the oscillation amplitude of an isolated (uncoupled) unit [51], i.e. $r_{1,2} = \sqrt{\lambda_{1,2}/\sigma_{1,2}}$. Hence, when further assuming that both oscillator units have the same amplitude, i.e. $r = r_1 = r_2$, the weakly coupled oscillator system reduces to a system of symmetrically coupled phase oscillators,

$$\dot{\phi}_1 = \tilde{\omega}_1 + J\sin(\phi_2 - \phi_1), \tag{2.5a}$$

$$\dot{\phi}_2 = \tilde{\omega}_2 + J\sin(\phi_1 - \phi_2). \tag{2.5b}$$

In this simplified model we see that while both oscillators try to run independently at their own intrinsic frequencies $\tilde{\omega}_i$, their weak coupling depends on the mutual phase difference and seeks to synchronise the system. The analysis can be readily extended to systems of N weakly coupled oscillators yielding a network of coupled phase oscillators described by the dynamical equations

$$\dot{\phi}_i = \tilde{\omega}_i + J \sum_{j=1}^{N} \sin(\phi_j - \phi_i), \quad i = 1, ..., N. \tag{2.6}$$

This is the paradigmatic Kuramoto model [52]. It is a universal model that describes dynamics and synchronisation phenomena of an ensemble of coupled oscillators with relevance to many fields ranging from physics, social science, chemistry and biology [5, 1]. It is known that the long-term dynamics of any system of weakly coupled limit cycle oscillators can be mapped onto a system of coupled phase equations with the Kuramoto model being the simplest form [53, 54]. In particular, a system comprising near-identical metronomes placed onto a moveable base exhibits synchronisation dynamics governed by coupled phase equations [49].

In the following we investigate the synchronised regime of two coupled phase oscillators described by Eqs. 2.5. The phase difference $\phi_{12} = \phi_1 - \phi_2$ between both phase oscillators evolves according to

$$\dot{\phi}_{12} = \Delta - 2J \sin(\phi_{12}), \tag{2.7}$$

where we have defined the frequency detuning $\Delta = \tilde{\omega}_1 - \tilde{\omega}_2$. It is apparent from Eq. 2.7 that synchronisation, i.e. equally evolving phases with $\dot{\phi}_{12} = 0$, is only possible for small detuning $|\Delta| \leq 2|J|$. The stable values of the phase difference ϕ_{12} can be obtained by noting that Eq. 2.7 has the form of a gradient system, $\dot{\phi}_{12} = -\partial V / \partial \phi_{12}$, with real valued function V

$$V(\phi_{12}) = -\Delta\phi_{12} - 2J \cos(\phi_{12}). \tag{2.8}$$

The function V is also called potential function because the state of the system $\phi_{12}(t)$ only evolves towards smaller values of V, thus dissipating potential energy, as can be seen by the time derivative

$$\frac{\partial V(\phi_{12})}{\partial t} = \frac{\partial V(\phi_{12})}{\partial \phi_{12}} \frac{\partial \phi_{12}}{\partial t} = -\left| \frac{\partial \phi_{12}}{\partial t} \right|^2 \leq 0. \tag{2.9}$$

Stable equilibrium points $\phi_{12}^{(0)}$ of the weakly coupled oscillator system described in Eq. 2.7 with $|\Delta| < 2|J|$ are thus given by the minima of the potential function V and are

located at

$$\phi_{12}^{(0)} = \begin{cases} \arcsin\left(\frac{\Delta}{2J}\right) & \in \left(-\frac{\pi}{2}, \frac{\pi}{2}\right), \quad \text{if } J > 0, \\ \arcsin\left(\frac{\Delta}{2J}\right) + \pi & \in \left(\frac{\pi}{2}, \frac{3\pi}{2}\right), \quad \text{if } J < 0. \end{cases} \tag{2.10}$$

The frequency synchronised units oscillate at the average of their intrinsic frequencies $\dot{\phi}_1 = \dot{\phi}_2 = (\tilde{\omega}_1 + \tilde{\omega}_2)/2$. For identical phase oscillators, i.e. $\Delta = 0$, the two possible synchronised configurations are characterised by a vanishing phase difference $\phi_{12} = 0$ (in-phase synchronisation) for attractive coupling $J > 0$ and $\phi_{12} = \pi$ (anti-phase synchronisation) for repulsive coupling $J < 0$, respectively.

A deeper insight into the stability of the frequency synchronised solutions is obtained by assuming small deviations from the equilibrium points, i.e. $\phi_{12}(t) = \phi_{12}^{(0)} + \eta(t)$, and linearising the dynamical Eq. 2.7 around these points,

$$\dot{\eta} = -\left.\frac{\partial^2 V}{\partial \phi_{12}^2}\right|_{\phi_{12}^{(0)}} \cdot \eta. \tag{2.11}$$

The solution of this ordinary differential equation is an exponential function $\exp(-\xi t)$, where the exponent is given by $\xi = \sqrt{4J^2 - \Delta^2}$. The sign of the real part of the introduced parameter ξ - often denoted as Lyapunov exponent - determines whether a small perturbation $\eta(t)$ is growing or shrinking in time. Therefore, stability of the solution $\phi_{12} = \phi_{12}^{(0)}$ is dependent on a positive value of $\Re(\xi)$ facilitating fast relaxation of perturbations such as noise in the system. In Fig.2.2(d) we show the real-valued Lyapunov exponent ξ as a function of frequency detuning Δ describing the stability of the synchronised states. We can see that largest stability (Lyapunov exponent) of the coupled phase oscillator system is obtained for vanishing detuning $\Delta = 0$ and stability monotonically decreases with increasing detuning $|\Delta|$ until the equilibrium point destabilises at $|\Delta| = 2|J|$. For even larger detunings $|\Delta| > 2|J|$ the coupled oscillator system is desynchronised.

2.4 Delay-coupled oscillators

Often interactions between coupled nonlinear oscillators are subject to finite signal propagation times [55]. Examples are the dendritic and axonal coupling delays in neuronal systems such as in our brain or the inter-cavity coupling of two spatially separated laser cavities. When the relevant coupling time delay τ exceeds the system's characteristic time scale, such as an oscillator's intrinsic oscillation period T, the dynamical complexity of the system can be greatly increased due to an effectively infinite dimensional state space [56]. The presence of delay in coupled nonlinear systems can

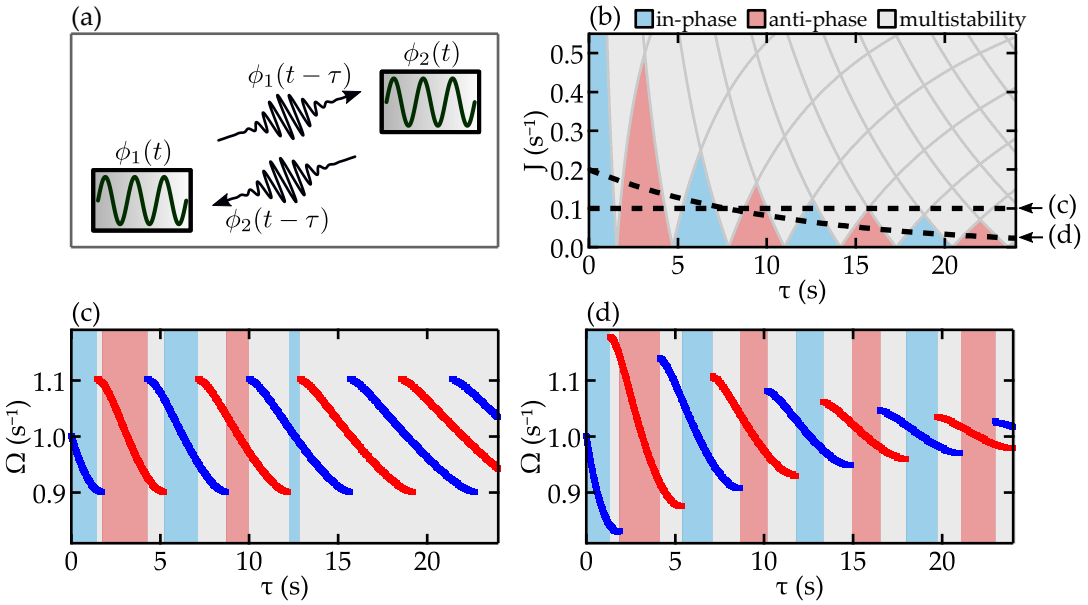

FIGURE 2.3: **Delay-coupled oscillators.** (a) Schematic of two oscillators with time-delayed coupling due to finite signal transfer speed. (b) Stability diagram of two identical delay-coupled phase oscillators (Eqs. 2.12) with eigenfrequencies $\tilde{\omega} = 1$ s^{-1} in the parameter space of coupling strength J and delay τ. (c) Frequencies Ω of the synchronised oscillators with increasing delay τ and fixed coupling strength J. (d) Frequencies Ω of the synchronised oscillators with increasing delay τ and exponentially decaying coupling strength J. In-phase and anti-phase synchronisation states are illustrated as red and blue coloured curves, respectively. Blue, red, and grey shaded areas indicate in-phase monostability, anti-phase monostability, and multistability, respectively. The parameter trajectories for (c) and (d) are illustrated in (b) as black dashed lines.

lead to a plethora of dynamical effects such as amplitude death [57], phase-flip bifurcations [58], chimera states [59] and both stabilisation and destabilisation of periodic orbits [2].

In the following we consider the case of two delay-coupled phase oscillators such as schematically illustrated in Fig.2.3(a). By introducing a time delay τ into the coupled oscillator Eqs. 2.5 the equations of motion for the two phases $\phi_{1,2}$ can be written as

$$\dot{\phi}_1(t) = \tilde{\omega} + J \sin\left(\phi_2(t-\tau) - \phi_1(t)\right), \tag{2.12a}$$

$$\dot{\phi}_2(t) = \tilde{\omega} + J \sin\left(\phi_1(t-\tau) - \phi_2(t)\right), \tag{2.12b}$$

where we have assumed identical eigenfrequencies $\tilde{\omega}$ for both oscillators. Synchronised and phase-locked states of the delay-coupled Kuramoto oscillators in Eqs. 2.12 can be obtained numerically as detailed for example in Ref. [60]. In contrast to the solutions of the instantaneously coupled oscillators described by Eqs. 2.10, due to the delayed coupling there can be more than one stable synchronisation frequency $\Omega = \dot{\phi}_1 = \dot{\phi}_2$ with both in-phase and anti-phase synchronisation configurations. We note that, also in the presence of a delay, in-phase and anti-phase synchronisation refers to

stable equal-time phase differences, i.e. $\phi_1(t) - \phi_2(t) = 0, \pi$ respectively. The stability regions for the mutually delay-coupled oscillator system are shown in Fig. 2.3(b) where blue (red) regions denote configurations with only monostable in-phase (anti-phase) phase-locked solution. Grey regions indicate multistability, i.e. more than one stable phase-locked state exist for the coupled oscillator system. It is apparent that the size of single-solution (monostable) regions is decaying with increasing time-delay, indicating the tendency of delay to enhance the system's dynamic complexity and, in this case, increasing the number of simultaneously stable solutions. A natural question one might ask is - despite the ubiquity of delay in interactions between coupled elements - at what point does a coupling delay effect the system's dynamics and needs to be considered in order to accurately model the system. While for small coupling delays $\tau \ll T = 2\pi/\tilde{\omega}$ there is no significant change in system dynamics and stability of the in-phase state compared to zero delay, the increase of delay τ exceeding the oscillators' intrinsic period $T = 2\pi/\tilde{\omega}$ can lead to destabilisation of the initial in-phase state and stabilisation of an anti-phase state despite a positive coupling parameter $J > 0$.

In Fig. 2.3(c) we show the frequency solutions Ω for increasing coupling delay τ while keeping the coupling constant J constant (see black dashed line in Fig. 2.3(b)). The periodically alternating branches of in-phase and anti-phase synchronisation states are limited in the frequency range $\tilde{\omega} \pm J$ and with increasing time-delay the monostable regions disappear, i.e. the system always features multistability. In a typical physical realisation the increase of time-delay τ between two coupled elements can be implemented by increasing their physical separation distance, however, such a modification often also reduces the coupling strength J due to a spatially decaying coupling signal. Assuming a coupling constant J that is exponentially decaying with increasing coupling delay τ (see black dashed curve in Fig. 2.3(b)) the resulting synchronisation frequencies Ω are shown in Fig. 2.3(d). We notice the exponentially decaying frequency range (size) of the branches with increasing delay τ and the enhancement of monostability even at larger delays due to the decaying coupling parameter. The transition from monostable in-phase to monostable anti-phase synchronisation configuration is always interleaved with a region of bistability, i.e. a region in which both phase-locked states are stable attractors.

2.5 Correlation function and mutual coherence between oscillators

When investigating synchronisation in systems of coupled oscillatory elements it is important to define how to quantify the synchronised state. While the definitions of synchronisation and phase-locking of two oscillators given in Section 2.2 present simple mathematical relations, any realistic system features finite correlation times and

deviations from a perfectly synchronised and phase-locked state e.g. due to noise. A measure for mutual coherence between two oscillators with complex-valued state functions $z_i(t)$ and $z_j(t)$ can be defined by their normalised (first-order) correlation function

$$g_{ij}(\eta) = \frac{\left\langle z_i^*(t+\eta) z_j(t) \right\rangle_t}{\sqrt{\left\langle |z_i(t)|^2 \right\rangle_t \left\langle |z_j(t)|^2 \right\rangle_t}}, \tag{2.13}$$

where $\langle ... \rangle_t$ denotes a time average and η refers to a time-difference between the two oscillator functions at which the average is calculated. The correlation function is a complex quantity from which we denote its modulus at zero time $|g_{ij}(\eta = 0)| \leq 1$ as the mutual coherence between z_i and z_j. For a fully-coherent (or synchronised) system of two oscillators their mutual coherence $|g_{ij}(0)| = 1$, while for an incoherent (unsynchronised) system the correlation function vanishes, $g_{ij}(0) = 0$. The special cases of in-phase and anti-phase synchronisation yield $g_{ij}(0) = 1$ and $g_{ij}(0) = -1$, respectively. For a partially coherent system, i.e. $0 < |g_{ij}(0)| < 1$, the argument $\arg(g_{ij}(0))$ is a measure for the average phase difference between the two oscillators.

The synchronisation phenomena of coupled oscillators presented in this section are of relevance for the discussion of coupled polariton condensates throughout this thesis. While in the context presented in this section we refer to general nonlinear coupled oscillators, the functions $z_i(t)$ and $z_j(t)$ in Eq. 2.13 can also represent the complex-valued mode amplitudes of two polariton condensates, such that $g_{ij}(\eta)$ describes the first-order complex degree of coherence between the two condensates. The rich dynamical regimes and phase-flip transitions presented for delay-coupled phase oscillators appear in our investigation of ballistically coupled polariton condensates in Chapter 5. Furthermore, the presented influence of homogeneity between interacting oscillators (such as their intrinsic frequencies) onto both phase-locking and stability is of importance for our study of coherence in larger arrays of coupled polariton condensates in Chapter 6.

Chapter 3

The Physics Of Semiconductor Microcavities

Microcavities are optical resonator structures with confinement sizes comparable to the wavelength of light. Embedding of resonant absorbers in semiconductor microcavities, such as quantum well (QW) excitons, facilitates light-matter coupling for optoelectronic applications, e.g. in the form of photodetectors or vertical-cavity surface-emitting lasers (VCSELs). In the case of strong coupling between cavity photons and QW excitons, new mixed light-matter quasi-particles called exciton-polaritons are formed. These hybrid quasi-particles inherit characteristics of both their light and matter constituents, e.g. light effective masses and strong nonlinearities. As composite bosons exciton-polaritons can undergo a power-driven phase transition into a macroscopically coherent state, a so-called polariton condensate. In this Chapter we present the fundamentals of strong coupling in planar semiconductor microcavities, describe the condensation process of exciton-polaritons, and detail on the coherence properties of polariton condensates.

3.1 Light-matter coupling in microcavities

Depending on technological application and building material there have been developed various geometries of microresonators, such as micropillar cavities, microtoroid resonators and photonic crystal cavities [61]. The most common microcavity, however, is the planar cavity comprising two parallel flat mirrors. Typically, the mirrors of these Fabry-Perrot-type cavities are either formed by highly reflective metallic surfaces, or by distributed Bragg reflectors (DBRs), i.e. periodically patterned two-dimensional dielectric or semiconductor layers of alternating refractive index. While in the former case the cavity modal field vanishes almost completely at the metallic surface, in the latter case the electric field has a substantial penetration depth into the Bragg mirror.

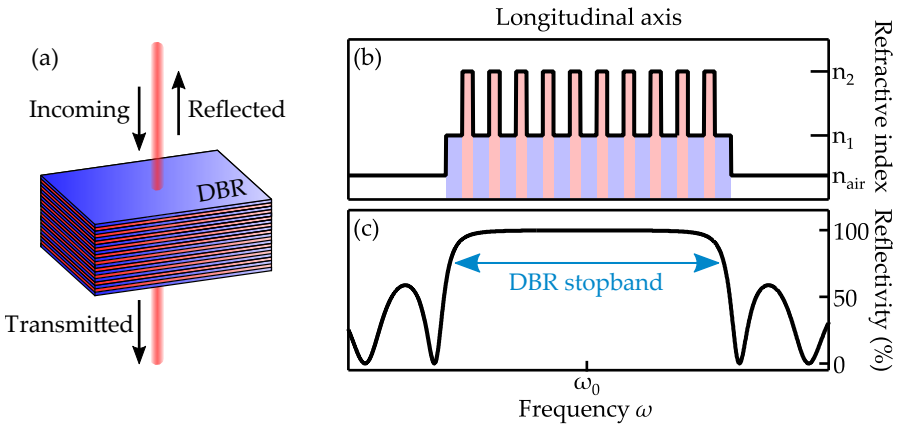

FIGURE 3.1: **Periodically patterned two-dimensional layers for use as a dielectric mirror.** (a) Schematic of the DBR structure with refractive index profile shown in (b). (c) Reflectivity spectrum for light under normal incidence onto the structure.

3.1.1 Distributed Bragg reflectors

Of importance for the design of microcavities is that the reflectivity properties of DBR structures can be tailored by changing the number of mirror stacks or the refractive index difference between the periodically alternating materials. A schematic DBR structure is illustrated in Fig. 3.1 (a) containing 10 pairs of alternating layers (shown in red and blue colour). An incoming electromagnetic wave will generally be partially reflected and partially be transmitted through the structure. The amount of reflected and transmitted energy depends on various parameters such as the signal's frequency ω and polarisation, the DBR's composition and size, and the angle of incidence [13]. The DBR's periodically alternating refractive index profile along its longitudinal (growth) axis is depicted in in Fig. 3.1(b). Each of the layers has a thickness d_i that equals a quarter wavelength, i.e. $d_i = \lambda_0/4n_i$ with $i = 1, 2$. The wavelength λ_0 corresponds to the frequency $\omega_0 = 2\pi c/\lambda_0$ for which the DBR structure is designed, and $n_{1,2}$ are the refractive indices of the DBR composite materials, respectively. The successive patterning of layers with thickness of a quarter wavelength yields constructive interference of reflected beams from each layer-to-layer interface, and causes a large reflectivity at the design frequency ω_0. The resulting reflectivity spectrum contains a photonic stopband centred around ω_0 as shown in Fig. 3.1 (c). The DBR stopband width Ω_{SB} is determined by the refractive index composition [13, Chapter 2],

$$\Omega_{SB} \approx \frac{8c|n_1 - n_2|}{\lambda_0(n_1 + n_2)}, \tag{3.1}$$

and increases with larger contrast between the two refractive indices n_1 and n_2.

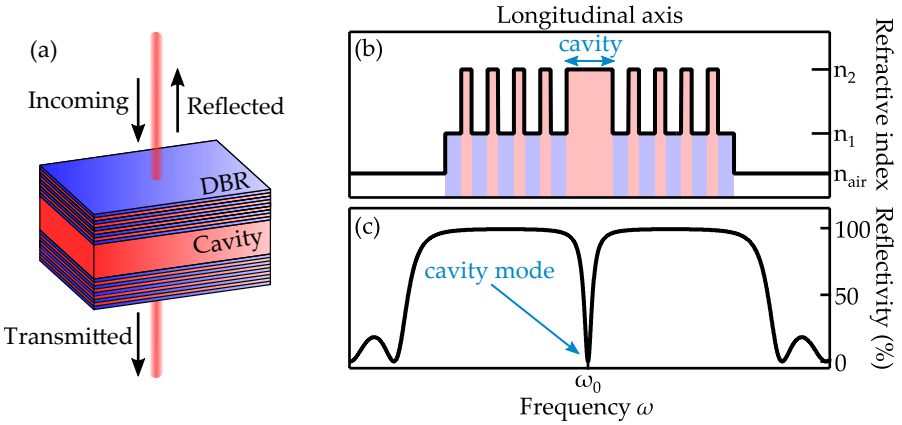

FIGURE 3.2: **Photonic cavity formed by parallel alignment of two DBR mirrors.** (a) Schematic of the microcavity structure with refractive index profile shown in (b). The cavity mode with frequency ω_0 placed within the DBR stopband results in a dip in the reflectivity spectrum depicted in (c).

3.1.2 Confinement of photons in a planar cavity

Starting with the Bragg reflector illustrated in Fig. 3.1 a planar microcavity can be formed by adding an additional layer into the center of the structure as schematically shown in Fig. 3.2(a). Thickness and refractive index of this 'cavity layer' are labelled as d_c and n_c, respectively. This layer can be seen as a "defect" inside a periodically patterned structure giving rise to new (confined) photonic modes. Under the assumption of normal incidence, negligible absorptivity and high reflectivity of the DBR structure the resonance condition for the confined longitudinal Fabry-Pérot modes can be written as

$$\omega_j = j\frac{\pi c}{n_c d_c}, \quad j \in \mathbb{N}^+. \tag{3.2}$$

The free spectral range (FSR) $\Delta\omega$, i.e. the equidistant frequency spacing between the longitudinal cavity modes, is inversely proportional to the cavity thickness d_c and given as

$$\Delta\omega = \frac{\pi c}{n_c d_c}. \tag{3.3}$$

For sufficiently thin resonators, such as microcavities, the FSR $\Delta\omega$ is often much larger than the DBR's stopband width Ω_{SB}. In that case, only one longitudinal mode can be present within the photonic stopband.

A schematic of the reflectivity spectrum of a photonic microcavity under normal incidence is shown in Fig. 3.2(c). The cavity mode with frequency ω_c gives rise to a dip in the reflectivity spectrum and is associated with resonant tunnelling of photons through the structure. For the photonic cavity presented in Fig. 3.2 the cavity resonance frequency ω_c is located in the center of the reflectivity stop band. This symmetric condition is realised when the cavity thickness d_c is chosen to be a multiple of a half-wavelength, i.e. $d_c = j\lambda_0/2n_c$.

The spectral broadening of the resonant mode shown in Fig. 3.2(c) is caused by radiative losses due to the finite mirror reflectivity. It can be associated with the lifetime τ_c of photons inside the cavity, i.e. there is a finite probability of photons to tunnel through the mirrors into the continuum. In any realistic system the cavity resonance is further broadened by additional absorption or scattering channels, e.g. due to defects. A resonator with resonance frequency ω_j and spectral full width at half maximum (FWHM) $\delta\omega_j$ is characterised by its quality factor Q,

$$Q = \frac{\omega_j}{\delta\omega_j}. \tag{3.4}$$

It is a measure for the ratio between the amount of energy that is stored in the cavity and the amount of energy that is lost in each oscillation cycle. The energy loss is linked to the cavity photon lifetime τ_c,

$$\tau_c = \frac{Q}{\omega_j}. \tag{3.5}$$

Taking into account the system's lateral translational invariance, each cavity mode is described by a wavevector $\mathbf{k}$, that is quantized in longitudinal (z) direction but shows continuous dispersion in transverse (x and y) directions. Denoting the lateral wavevector as $\mathbf{k}_\parallel$, the cavity in-plane dispersion can be approximated as parabolic for small angles of incidence,

$$\omega_j(\mathbf{k}_\parallel) = \omega_j\sqrt{1 + \frac{k_\parallel^2}{\omega_j^2 n_c^2/c^2}} \approx \omega_j + \frac{\hbar k_\parallel^2}{2m_c}. \tag{3.6}$$

Here, we have introduced the cavity photon effective mass $m_c = \hbar\omega_j n_c^2/c^2$ (see e.g. Ref. [62, Chapter 9]). In comparison to electronic systems, the effective photon mass in microcavities is very light and typically in the order of $10^{-5}m_e$, where m_e is the free electron mass.

3.1.3 Excitons in quantum wells

Excitons in crystalline solids are electrically neutral compound particles formed by Coulomb attraction between electrons and holes. An exciton is an elementary excitation of a bulk semiconductor, and created when exciting an electron from the valence band to the conduction band, e.g. by optical excitation. Due to its similarity to a bound electron-proton pair, the particle wavefunction and energy spectra of excitons have similar structure to the hydrogen atom [62, Chapter 9]. For a bulk semiconductor with

bandgap energy E_g, free excitons have the energy dispersion relation

$$E_n^{X,3D}(\mathbf{k}) = E_g - \frac{R_0}{n^2} + \frac{\hbar^2 k^2}{2M_X}, \quad n \in \mathbb{N}^+. \tag{3.7}$$

Here, the exciton translational mass $M_X = m_e^* + m_h^*$ is given as the sum of effective electron and holes masses m_e^* and m_h^* of the crystalline solid. The exciton Rydberg energy R_0 defines the scale of the binding energy and, therefore, is a measure for the thermal stability of the quasi particle. It is dependant on material properties such as the permittivity ϵ and reads as

$$R_0 = \frac{2e^4 m_X}{(8\pi)^2 \epsilon^2 \hbar^2}. \tag{3.8}$$

The introduced exciton effective mass $m_X = m_e^* m_h^* / (m_e^* + m_h^*)$ represents the reduced mass of electron and holes masses. Due to their larger effective mass m_X and smaller permittivity ϵ, wide-bandgap semiconductors such as ZnO ($R_0 \approx 62$ meV) or GaN ($R_0 \approx 26$ meV) typically have a larger Rydberg energy than, for instance, GaAs ($R_0 \approx 4.2$ meV) [62, Chapter 9]. Importantly, this means that excitons in wide-bandgap semiconductors can be stable at room-temperature ($k_B T \approx 25$ meV).

A QW is a thin (few nanometers) layer of semiconductor material embedded in between two materials with different conduction band and valence band energies representing an effective potential well structure for electrons and holes. The longitudinal confinement of electrons and holes within the QW causes an additional exciton confinement energy term E_C, and leads to the 2D exciton dispersion relation,

$$E_n^{X,2D}(\mathbf{k}_\parallel) = E_g + E_C - \frac{R_0}{(n-1/2)^2} + \frac{\hbar^2 k_\parallel^2}{2M_X}, \quad n \in \mathbb{N}^+. \tag{3.9}$$

It is important to note, that in comparison with the bulk energy spectrum [Eq. 3.7], excitons in QWs have a ground state binding energy ($n = 1$) that is larger by a factor of 4. Moreover, the increased spatial overlap of electron and hole wavefunctions in confined systems yields a larger exciton oscillator strength f in QWs than in bulk [62, Chapter 9]. The oscillator strength is a dimensionless quantity describing the effective coupling between light and the optically active exciton mode, i.e. the probabilities of absorption and emission of photons. Therefore, low-dimensional structures such as QWs are preferred systems for studying excitonic phenomena with enhanced optical transitions and at elevated temperatures .

The commutator of exciton creation and annihilation field operators $X^\dagger$ and X in 2D systems satisfies [13, Chapter 5]

$$\left\langle \left[X^\dagger, X \right] \right\rangle \approx 1 - \mathcal{O}(n_X a_B^2). \tag{3.10}$$

Here, we have introduced the exciton density n_X and excitonic Bohr radius a_B. Under the assumption of low particle densities $n_X \ll a_B^2$, excitons can be treated as (weakly interacting) Bosons. For larger densities, however, the density-dependent correction term destroys their bosonic character. The critical density $n_X a_B^2 \approx 1$ is also referred to as the Mott density. Beyond the exciton Mott transition $n_X a_B^2 > 1$ the large particle interaction terms causes ionization of excitons into an unbound electron-hole plasma.

3.1.4 Strong coupling and exciton-polaritons

Optoelectronic applications and devices rely on light-matter interactions enabling an interplay of photonic and electronic modes inside the system material. For the presented planar cavity [Section 3.1.2], one can implement an active medium in the form of a semiconductor QW structure [Section 3.1.3] inside the cavity layer, which gives rise to optically active and confined excitonic modes. A schematic of the microcavity structure containing coupled photon and exciton modes is depicted in Figs. 3.3(a) and (b). The coupling strength of cavity photons and QW excitons is characterised by their interaction energy $\hbar\Omega_R$, where the Rabi frequency Ω_R describes the rate at which energy is exchanged between photon and exciton mode. The microcavity reflectivity spectrum of strongly coupled exciton and photon modes under normal incidence is shown in Fig. 3.3(c). Here, the degeneracy of bare cavity and QW exciton mode energies is lifted, and two new resonances split by the Rabi frequency Ω_R appear. These resonances resemble the system's hybridised exciton-polariton modes. The apparent energy repulsion of two coupled resonances can be described in terms of two linearly-coupled harmonic oscillators as described in the following.

The coupled exciton-photon Hamiltonian H can be expressed as [13, Chapter 5]

$$H = \sum_{\mathbf{k}_\parallel} E_C(\mathbf{k}_\parallel) C^\dagger_{\mathbf{k}_\parallel} C_{\mathbf{k}_\parallel} + \sum_{\mathbf{k}_\parallel} E_X(\mathbf{k}_\parallel) X^\dagger_{\mathbf{k}_\parallel} X_{\mathbf{k}_\parallel} + \frac{\hbar\Omega_R}{2} \sum_{\mathbf{k}_\parallel} \left[C^\dagger_{\mathbf{k}_\parallel} X_{\mathbf{k}_\parallel} + C_{\mathbf{k}_\parallel} X^\dagger_{\mathbf{k}_\parallel} \right]. \tag{3.11}$$

Here, cavity mode and QW exciton mode energy dispersion relations are denoted as $E_C(\mathbf{k}_\parallel)$ and $E_X(\mathbf{k}_\parallel)$ with details given in Eqs. 3.6 and 3.9. The first two terms in Eq. 3.11 represent the bare cavity and bare exciton energies with photon and exciton field operators $C_{\mathbf{k}_\parallel}$ and $X_{\mathbf{k}_\parallel}$, respectively. The third term describes exciton-photon interactions, represented by absorption and emission cycles at frequency Ω_R.
Because there is no mixing of inplane wavevectors $\mathbf{k}_\parallel$ present in Eq. 3.11, the Hamiltonian H can be split into the sum, $H = \sum_{\mathbf{k}_\parallel} H_{\mathbf{k}_\parallel}$, where each term $H_{\mathbf{k}_\parallel}$ can be written in matrix notation,

$$H_{\mathbf{k}_\parallel} = \begin{bmatrix} E_C(\mathbf{k}_\parallel) & \hbar\Omega_R/2 \\ \hbar\Omega_R/2 & E_X(\mathbf{k}_\parallel) \end{bmatrix}. \tag{3.12}$$

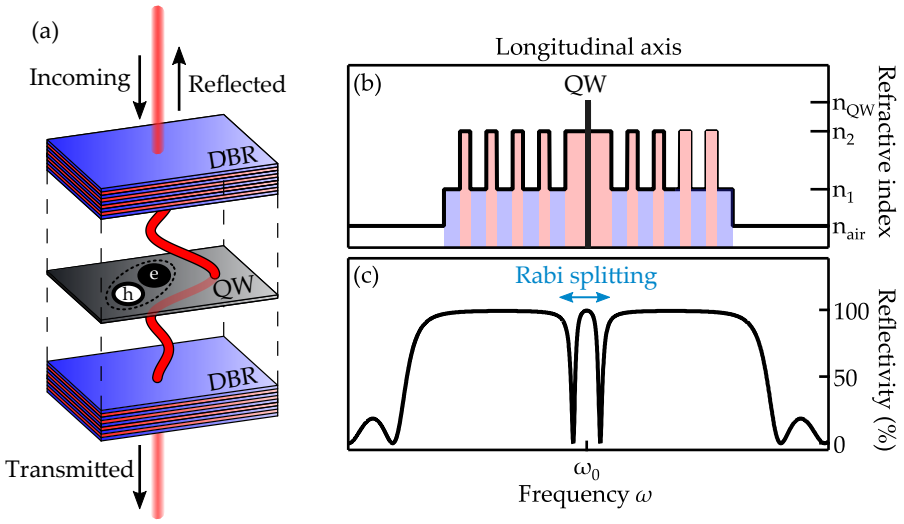

FIGURE 3.3: **Strong coupling of photon and QW exciton modes.** (a) Schematic of the microcavity structure with refractive index profile shown in (b). (c) Reflectivity spectrum for normal incidence. Strong coupling of photon mode and excitonic mode result in the formation of two polaritonic resonances, which are split by the Rabi frequency.

Diagonalisation of the Hamiltonian $H_{\mathbf{k}_\parallel}$ then yields the lower polariton branch (LP) and upper polariton branch (UP) eigenstates

$$|\mathrm{LP}_{\mathbf{k}_\parallel}\rangle = c_{\mathbf{k}_\parallel}\,|\mathrm{C}_{\mathbf{k}_\parallel}\rangle - \chi_{\mathbf{k}_\parallel}\,|\mathrm{X}_{\mathbf{k}_\parallel}\rangle\,, \tag{3.13a}$$

$$|\mathrm{UP}_{\mathbf{k}_\parallel}\rangle = \chi_{\mathbf{k}_\parallel}\,|\mathrm{C}_{\mathbf{k}_\parallel}\rangle + c_{\mathbf{k}_\parallel}\,|\mathrm{X}_{\mathbf{k}_\parallel}\rangle\,. \tag{3.13b}$$

The mixing coefficients $c_{\mathbf{k}_\parallel}$ and $\chi_{\mathbf{k}_\parallel}$ denote the so-called Hopfield coefficients. Their squared norms, $|c_{\mathbf{k}_\parallel}|^2$ and $|\chi_{\mathbf{k}_\parallel}|^2$, represent the fraction of photonic and excitonic component for each polariton branch, respectively. Furthermore, the polariton resonances are characterised by the coupled-mode dispersion relations

$$E_{\mathrm{UP,LP}}(\mathbf{k}_\parallel) = \frac{1}{2}\left[E_C(\mathbf{k}_\parallel) + E_X(\mathbf{k}_\parallel) \pm \sqrt{\left[E_C(\mathbf{k}_\parallel) - E_X(\mathbf{k}_\parallel)\right]^2 + \hbar^2\Omega_R^2}\,\right] \tag{3.14}$$

While the uncoupled bare exciton and cavity modes might be in resonance at some in-plane wavevector $\mathbf{k}_\parallel$, i.e. $E_C(\mathbf{k}_\parallel) = E_X(\mathbf{k}_\parallel)$, their coupling leads to repulsion and the formation of two energy levels split by the Rabi energy $\hbar\Omega_R$. The spectral repulsion and hybridisation of exciton and cavity modes are schematically illustrated in Fig. 3.4(a). One can notice that the bare exciton energy branch $E_X(\mathbf{k}_\parallel)$ seems dispersionless because of the heavy effective mass of excitons compared to cavity photons.

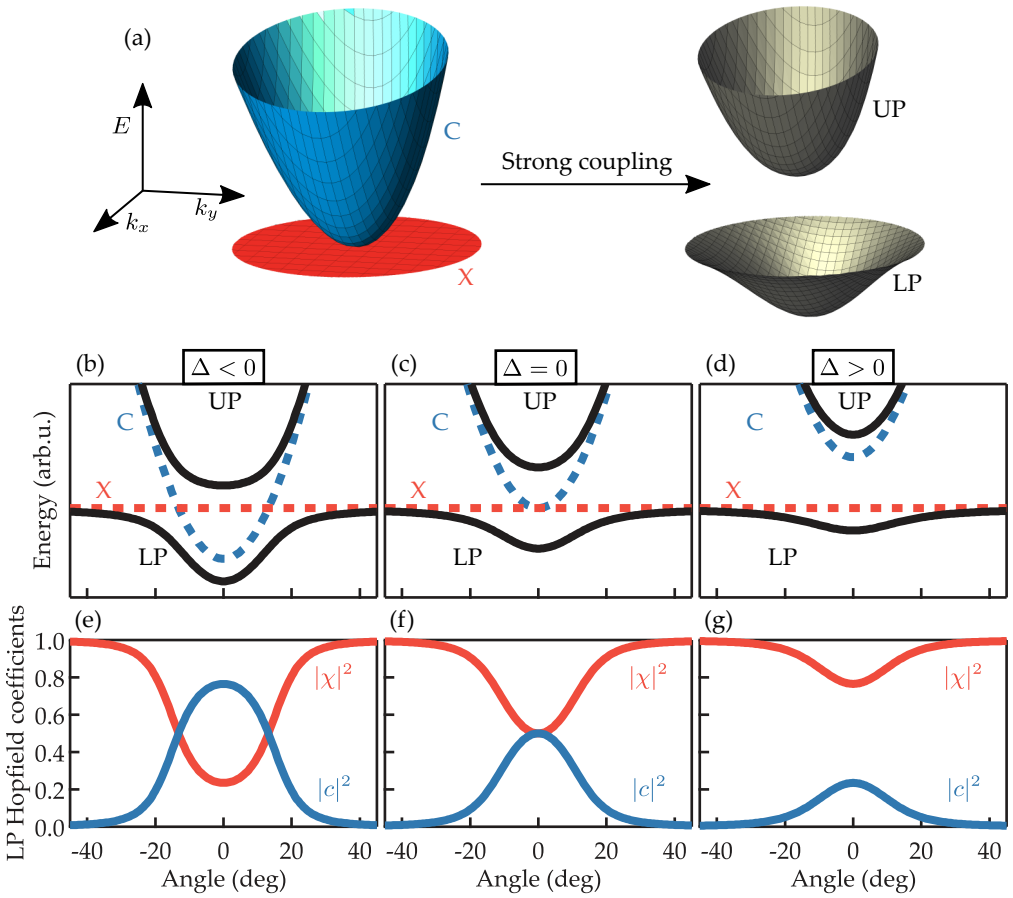

FIGURE 3.4: **Exciton-polariton energy branches in microcavities.** (a) Hybridisation of bare QW exciton (X) and cavity photon (C) mode into upper polariton (UP) and lower polariton (LP) modes. (b-d) Energy dispersion relations and (e-g) calculated LP Hopfield coefficients for (b,e) negative detuning, (c,f) vanishing detuning, and (d,g) positive detuning.

The photonic and excitonic fractions of the polariton modes are given as

$$|c_{\mathbf{k}_\parallel}|^2 = \frac{E_{\mathrm{UP}}(\mathbf{k}_\parallel)E_X(\mathbf{k}_\parallel) - E_{\mathrm{LP}}(\mathbf{k}_\parallel)E_C(\mathbf{k}_\parallel)}{\left[E_C(\mathbf{k}_\parallel) + E_X(\mathbf{k}_\parallel)\right]\sqrt{\left[E_C(\mathbf{k}_\parallel) - E_X(\mathbf{k}_\parallel)\right]^2 + \hbar^2\Omega_R^2}}, \tag{3.15a}$$

$$|\chi_{\mathbf{k}_\parallel}|^2 = \frac{E_{\mathrm{UP}}(\mathbf{k}_\parallel)E_C(\mathbf{k}_\parallel) - E_{\mathrm{LP}}(\mathbf{k}_\parallel)E_X(\mathbf{k}_\parallel)}{\left[E_C(\mathbf{k}_\parallel) + E_X(\mathbf{k}_\parallel)\right]\sqrt{\left[E_C(\mathbf{k}_\parallel) - E_X(\mathbf{k}_\parallel)\right]^2 + \hbar^2\Omega_R^2}}. \tag{3.15b}$$

(3.15c)

Polaritons are hybrid quasi-particles formed by the coherent superposition of bare bosonic cavity and exciton mode with mixing parameters described by Eqs. 3.13 and 3.15. In typical realisations, cavity photons are characterised by a small effective mass $m_c^* \approx 10^{-5} m_e$ and a short lifetime $\tau_c \approx 1 - 100$ ps, while semiconductor excitons such as in GaAs have a larger effective mass $m_X^* \approx 0.2 m_e$ and longer radiative lifetime $\tau_X \approx 0.1 - 1$ ns. Importantly, the particle properties of exciton-polaritons in microcavities can be tuned by variation of their respective Hopfield coefficients. For this purpose,

microcavities are often fabricated with a shallow gradient of the cavity layer thickness, allowing for experimental access to different exciton-photon detuning parameters $\Delta = E_C(0) - E_X(0)$ and, therefore, experimental control over the polariton Hopfield coefficients.

Calculated energy dispersion relations and Hopfield coefficients for varying detuning parameters $\Delta < 0$, $\Delta = 0$, and $\Delta > 0$ are illustrated in Figs. 3.4(b-d) and Figs. 3.4(e-f), respectively. All graphs are plotted versus the cavity polariton emission angle $\theta = \sin^{-1}(k_{\parallel}/k)$. Regardless of the detuning parameter, for large emission angles the upper (lower) polariton branch is asymptotic to the bare cavity (exciton) mode, which is expressed by its Hopfield coefficient $|\chi|^2 \to 1$. At small emission angles, however, a change in detuning parameter Δ can have a strong influence on the polariton properties. Experimental results presented in this thesis are obtained using a negatively detuned microcavity [presented in Chapter 4.1]. For negative detunings, the LP particles with small in-plane wavevector $k_{\parallel} \approx 0$ have a large photonic component, while LP particle at large wavevectors are dominantly excitonic.

It is worth noting that embedding of multiple QWs within the microcavity, typically at the anti-nodes of the cavity electric field distribution, helps to increase the Rabi splitting Ω_R and decreases the exciton density per QW. This, in turn, improves stability of cavity polaritons and lowers the particle density to avoid the critical Mott density.

Next, it should be noted that the energy level repulsion described in Eq. 3.14 occurs, however weak the interaction term $\hbar\Omega_R$ is. In any physical realisation, though there will always be a finite linewidth-broadening dissipation term present for both, cavity mode and exciton mode described by the terms γ_c and γ_X. Strong coupling, i.e. the coherent superposition of exciton and photon mode as in Eqs. 3.13, can then only occur, when the coupling term is larger than any dephasing mechanism. In other words, the coupled-mode frequency splitting Ω_R should be larger than the bare mode linewidths, i.e. $\Omega_R > \gamma_c, \gamma_X$. In the strong coupling regime the energy transfer rate Ω_R between bare cavity and exciton modes is larger than the particle loss rates. In quantum mechanics a system described by a Hamiltonian with large off-diagonal coupling terms cannot be treated using perturbation theory, but rather has to be diagonalised to accurately capture the system dynamics. The polariton modes are then the new eigenstates of the system. When the energy transfer rate is slower than the respective exciton and photon decay rates, $\Omega_R < \gamma_c, \gamma_X$, the system is said to be weakly coupled. A microcavity operating in the weak coupling regime can represent a VCSEL, and the system dynamics can be treated using perturbative methods.

3.2 Condensation of exciton-polaritons in microcavities

Microcavity polaritons are bosonic quasi particles and, as such, can exhibit bosonic phase transitions, e.g. the emerging macroscopic occupation of a single-particle quantum state. Such macroscopic quantum phenomena have attracted many different areas in physics and chemistry due to their bridge between quantum mechanical wave dynamics, and experimental accessibility on a macroscopic scale. Well-known examples of bosonic phase transitions with the emergence of a macroscopically coherent state range from Bose-Einstein condensation (BEC) of ultra cold atomic gases [9, 10], the superfluid phase transition of liquid helium [6, 7], the superconducting transition of solid mercury at cryogenic temperatures [63], and the non-equilibrium phase transition of photons in a laser. General criteria of a bosonic condensate, whether in thermal equilibrium or not, were outlined by Penrose and Onsager [64], and Yang [65], and are summarised in the following section.

3.2.1 Definition and characteristics of a condensate

A general many-body system with fixed particle number N is captured by its density operator $\hat{\rho}(t)$, and can be written as the statistical mixture of pure states $|\Psi_s(t)\rangle$ with weights $p_s(t)$, i.e.

$$\hat{\rho}(t) = \sum_s p_s(t) \left|\Psi_s(t)\right\rangle \left\langle\Psi_s(t)\right| . \tag{3.16}$$

For description of the system's first-order spatial correlation properties we are reducing the analysis to the so-called 'one-particle reduced density matrix' $\rho_1(\mathbf{x}, \mathbf{x}', t)$, which is defined as

$$\rho_1(\mathbf{x}, \mathbf{x}', t) = \langle \hat{\Psi}^\dagger(\mathbf{x}, t)\hat{\Psi}(\mathbf{x}', t)\rangle . \tag{3.17}$$

Here, operators $\hat{\Psi}^\dagger$ and $\hat{\Psi}$ represent particle creation and annihilation field operators and $\langle ...\rangle$ denotes the expectation value in the mixed state. When projecting the operators in Eq. 3.17 onto spatial coordinates, the reduced density matrix becomes apparent as the partial trace of $\hat{\rho}$ over $N-1$ particle coordinates [66];

$$\rho_1(\mathbf{x}, \mathbf{x}', t) = N \sum_s p_s(t) \int \Psi_s^*(\mathbf{x}, \mathbf{x}_2 ..., \mathbf{x}_N, t)\Psi_s(\mathbf{x}', \mathbf{x}_2 ..., \mathbf{x}_N, t) \mathrm{d}\mathbf{x}_2 ... \mathrm{d}\mathbf{x}_N . \tag{3.18}$$

The mathematical presentation in Eq. 3.18 implies the physical meaning of the one-particle reduced density matrix as the product of probability amplitudes to find a particle at positions $\mathbf{x}$ and $\mathbf{x}'$, averaged over the distribution functions of all other $N-1$ particles.
Since the reduced density matrix $\rho_1(\mathbf{x}, \mathbf{x}', t)$ is Hermitian, it can further be written in

diagonal form, i.e. it can be decomposed into a complete and orthonormal set of single-particle wavefunctions $\psi_i(\mathbf{x}, t)$,

$$\rho_1(\mathbf{x}, \mathbf{x}', t) = \sum_i n_i(t)\psi_i^*(\mathbf{x}, t)\psi_i(\mathbf{x}', t). \tag{3.19}$$

The eigenvalues n_i describe the populations of each single-particle quantum state ψ_i, respectively, and the total particle density $n(\mathbf{x}, t)$ is given by the trace (sum of diagonal elements),

$$n(\mathbf{x}, t) = \sum_i n_i(t)|\psi_i(\mathbf{x}, t)|^2. \tag{3.20}$$

Macroscopic population of a specific single-particle state ψ_i, i.e. the existence of a condensate fraction within the many-body system, then means that the population ratio n_i/N of this state is of order unity [64],

$$n_i/N = \mathcal{O}(1) \leftrightarrow \text{condensed state } \psi_i. \tag{3.21}$$

Description of the condensed state is given by the condensate wave function $\Psi(\mathbf{x}, t)$ and defined as

$$\Psi(\mathbf{x}, t) = \sqrt{n_i(t)}\psi_i(\mathbf{x}, t). \tag{3.22}$$

The macroscopically populated wave function $\Psi(\mathbf{x}, t)$ is also called the condensate order parameter. This order parameter is a measure for the system's bosonic phase transition, that vanishes in one phase $|\Psi(\mathbf{x}, t)|^2 = 0$, but has non-vanishing value $|\Psi(\mathbf{x}, t)|^2 > 0$ in the other phase. The phase transition is further characterised by a spontaneous symmetry breaking of the system's continuous global $U(1)$ gauge symmetry; in every realisation the condensate is formed with a random but specific global phase. Examples of control parameters for phase transitions in a many-body system are the temperature T in case of a dilute atomic gas, or the pump power P in case of driven-dissipative systems such as lasers or polariton condensates. The BEC phase transition of an ideal gas is schematically illustrated in Fig. 3.5(a).

Experimentally it can be difficult to provide sufficient evidence of a condensed state by investigating the diagonal elements of the one-particle density matrix $\rho_1(\mathbf{x}, \mathbf{x}, t)$ only, e.g. in form of particle density measurements [Eq. 3.20]. However, an equivalent and generally accepted defining characteristic of a condensed state was given by Penrose and Onsager [64] and Yang [65], and focuses on the off-diagonal terms of the reduced density matrix instead. The existence of a condensed state is then related to the presence of off-diagonal long-range order (ODLRO), i.e.

$$\rho_1(\mathbf{x}, \mathbf{x}', t) \xrightarrow[|\mathbf{x}-\mathbf{x}'|\to\infty]{} \Psi^*(\mathbf{x}', t)\Psi(\mathbf{x}, t), \tag{3.23}$$

which for an infinite system would be non-vanishing even in the limit $|\mathbf{x} - \mathbf{x}'| \to \infty$.

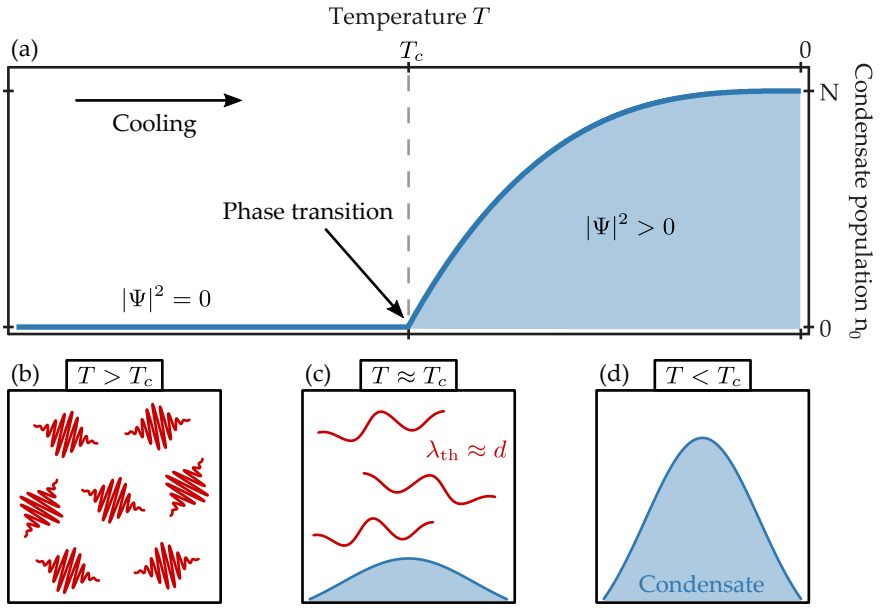

FIGURE 3.5: **Bose-Einstein condensation of an ideal gas.** (a) Emergence and growth of the condensate population n_0 with decreasing temperature T. (b-d) Illustration of the formation of coherence with decreasing temperature. Uncondensed wavepackets with spatial extension given by the thermal de Broglie wavelength λ_{th} are shown in red, and the emerging macroscopically coherent state (condensate) is shown in blue.

In case of a three-dimensional ideal (thermalised) Bose gas above the phase transition temperature ($T > T_c$) the decay of correlations is dominated by thermal fluctuations. In particular, the characteristic length scale of spatial correlations is determined by the thermal de Broglie wavelength λ_{th},

$$\lambda_{\mathrm{th}}(T) = \sqrt{\frac{2\pi\hbar^2}{mk_B T}}, \tag{3.24}$$

and the reduced density matrix (correlation function) decays approximately as $\rho(x,0) \approx \exp\left(-\pi x^2/\lambda_{\mathrm{th}}^2\right)$ [67, 68]. Thus, in a simplified picture, the thermalised bosonic particles can be seen as quantum mechanical Gaussian wavepackets with spatial extension given by the thermal de Broglie wavelength λ_{th} [see Fig. 3.5(b)]. Cooling of the Bose gas leads to an increase of the correlation length up to the point where λ_{th} becomes comparable to the mean particle separation distance d. At this point, particle wavepackets start overlapping and their phases become correlated [see Fig. 3.5(c)]; the gas undergoes a BEC phase transition [69]. More rigorous calculation of the critical temperature T_c for a three-dimensional ideal Bose gas leads to the condition

$$\lambda_{\mathrm{th}}(T_c)/d \approx 1.38 \tag{3.25}$$

One can notice, that the critical temperature T_c scales inversely with the particle mass m. In principle, this means that the BEC phase transition can occur at higher temperatures T for lighter particles such as excitons or polaritons as compared to atoms. Below the

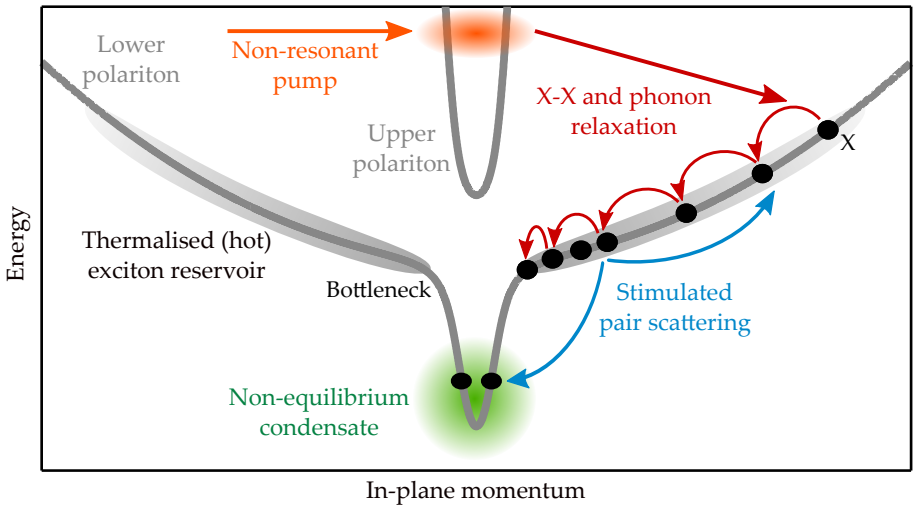

FIGURE 3.6: **Condensation of polaritons under non-resonant optical excitation.**

critical temperature ($T < T_c$) a macroscopically populated quantum state has emerged [see Fig. 3.5(d)] and the correlation function ρ_1 has established ODLRO [Eq. 3.23].

Experimental access to (off-diagonal) spatial correlations is provided, e.g. by momentum-space ('time-of-flight' expansion) measurements in ultra cold atom experiments [70], or by interferometric measurements in polariton systems as described in Sections 3.3 and 4.4.4. The spontaneous build-up of long-range spatial coherence (or ODLRO) is then a defining feature of the condensation threshold.

3.2.2 Build-up of spontaneous coherence in semiconductor microcavities

In contrast to the conserved particle numbers found in ultracold atom experiments, coherent phenomena of exciton-polaritons are subject to an interplay of gain and (mainly radiative) losses. In a typical polariton condensate experiment gain is provided either by optical or electrical injection of carriers. While a coherent population of polaritons can in principle be injected resonantly via an external pump laser, it is only via non-resonant pumping that a phase transition with the spontaneous formation of coherence can be studied. The first demonstrations of spontaneous coherence formation in the LP states under non-resonant optical excitation were conducted on GaAs [14, 71, 72], CdTe [15, 73] and GaN [19, 20] microcavities. Hereby, the excitation laser wavelength is typically blue-detuned towards the first reflection minimum of the DBR stop-band, ensuring efficient optical excitation of free carriers that are energetically located ≈ 100 meV above the LP ground state. Any subsequently appearing (coherent) cavity emission originating from the LP dispersion branch is the result of many de-phasing particle relaxation processes. Importantly, this ensures that the emergence of spatial coherence is indeed due to spontaneous symmetry breaking at the condensation phase transition, and not inherited by the coherence of the excitation laser.

The polariton relaxation kinetics and formation of spontaneous coherence under non-resonant optical excitation are schematically depicted in Fig. 3.6. The optically excited high-energy electron-hole gas quickly dissipates energy on a picosecond time scale mainly by emission of longitudinal-optical phonons, and leads to the population of the exciton dispersion at large in-plane momenta [13, Chapter 8]. Subsequent particle relaxation processes are dominantly based on exciton-exciton and exciton-acoustic phonon interactions. While the former process mainly leads to a redistribution of energy within the exciton cloud, the latter process transfers energy to the host lattice. Since the lifetime of excitonic states ($\tau_X \approx 0.1 - 1$ ns) is much larger than their relaxation time ($\tau \approx 10$ ps), quasi-thermalisation of the incoherent exciton cloud is possible.

However, relaxation processes become less efficient once the particles have reached the edge of the 'polariton momentum space trap', which is formed by the hybridisation of exciton and cavity modes. Beyond this point scattering rates are reduced due to a decrease in density of states and due to a decrease of the excitonic Hopfield coefficient $|\chi|^2$ inside the polariton trap. Moreover, polariton lifetimes are greatly reduced at small momenta due their growing photonic component $|c|^2$, generally preventing the polariton gas from reaching thermal equilibrium. The accumulation of excitonic particles at the 'neck' of the LP dispersion relation is named the 'bottleneck effect' [74].

When reaching sufficiently large particle densities, 'stimulated pair scattering' of bottleneck excitons can become the dominant scattering process, and facilitates population of polariton states within the LP momentum space trap [see Fig. 3.6]. Hereby, two particles with energies $E_{1,2}$ and momenta $\mathbf{k}_{1,2}$ elastically scatter via dipole-dipole interactions into new states with energies $E_{3,4}$ and momenta $\mathbf{k}_{3,4}$, while total energy and momentum are conserved. Bosonic final state stimulation yields a coherent polariton-polariton scattering rate W that is enhanced by the occupation $N_{\mathbf{k}}$ of final states, i.e.

$$W_{\mathbf{k}_1,\mathbf{k}_2\rightarrow\mathbf{k}_3,\mathbf{k}_4} \propto N_{\mathbf{k}_1} N_{\mathbf{k}_2} (N_{\mathbf{k}_3} + 1)(N_{\mathbf{k}_4} + 1). \tag{3.26}$$

Once the occupancy $N_{\mathbf{k}}$ of a final state within the polariton trap exceeds unity, the stimulated scattering rate overtakes its spontaneous counterpart, and a coherent many-body state emerges [15].

It is important to note that, in the case of polariton condensates, the final state that first reaches condensation threshold is not necessarily coinciding with the LP ground state located at $\mathbf{k} = 0$, but can exist at elevated energies and finite momenta $|\mathbf{k}| > 0$. While the use of a large-size pump spot (FWHM $\gtrsim$ 30 μm) and positive detuning parameter ($\Delta > 0$) generally favours ground state polariton condensation [15], optical excitation with narrow laser spots (FWHM $\lesssim$ 20 μm) and negative detuning ($\Delta < 0$) facilitates non-ground state condensation [73, 75]. Details on this phenomenon are given in Section 5.2.

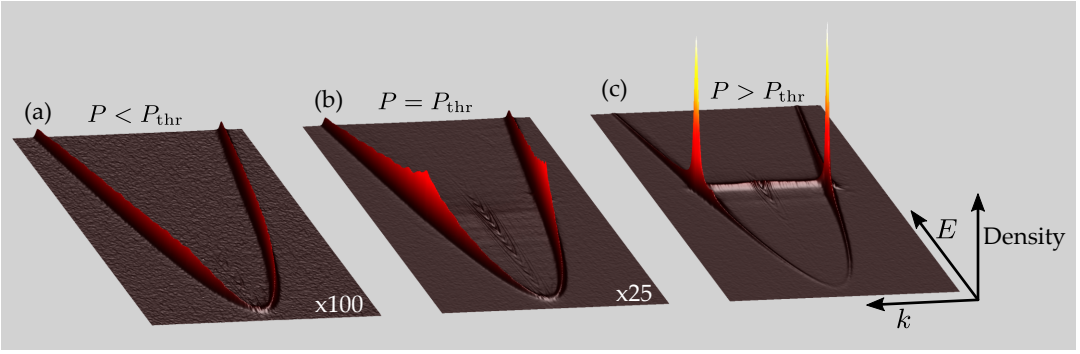

FIGURE 3.7: **Non-equilibrium condensation of exciton-polaritons under non-resonant pumping geometry.** Elevation and false-colour represent condensate spectral density at given in-plane wavevector k and lower polariton branch energy E. Increasing the pump power P (from left to right) above the threshold P_{thr} yields a macroscopic occupation of a single-particle state. The plot elevation below and at condensation power is magnified by factor 100 and 25, respectively.

Typical measurement data of the power-driven phase transition of a polariton gas generated using a narrow pump laser spot (FWHM $\approx$ 2 µm) are illustrated in Fig. 3.7. Here, the LP particle densities are shown in the plane of energy E and in-plane wave vector $\mathbf{k}$ for three different pump powers P. For small pump powers, i.e. small excited LP particle densities, there is a broad spectral occupation of the LP momentum space polariton trap [Fig. 3.7(a)]. With increasing excitation pump power reaching condensation threshold ($P \approx P_{\mathrm{thr}}$) a spectral narrowing of the LP particle density distribution becomes visible, indicating the emergence of a macroscopically populated quantum state [Fig. 3.7(b)]. For larger pump powers ($P > P_{\mathrm{thr}}$) almost all particles occupy the same state [Fig. 3.7(c)]. Importantly, the narrow particle density distribution in both energy, and momentum space above condensation threshold is the result of established temporal and spatial coherence.

3.2.3 Characteristics of polariton condensates

Owing to their light effective mass $m \approx 10^{-5} m_e$, polaritons are promising candidates for the study of macroscopic quantum phenomena at elevated temperatures. However, due to their intrinsic short lifetime $\tau \approx 1$ ps $-$ 100 ps, thermalisation of polaritons can be hindered, such that any occurring phase transition cannot be described in thermal equilibrium. While macroscopic occupation of the polariton ground state in thermal equilibrium is generally referred to as polariton BEC [15, 76], an out-of-equilibrium macroscopically populated state is often termed 'polariton laser' [16]. A comparison of the characteristics of polariton BEC, polariton laser, and photon laser can be found in Reference [11].

Throughout this work, we are denoting our results of out-of-equilibrium coherent many-body states as 'polariton condensates'. These polariton condensates emerge from an incoherent non-resonantly pumped exciton reservoir via a power-driven phase transition with the following properties:

1. Appearance of long-range spatial coherence (ODLRO) across the system at threshold.
2. Narrowing of the spectral density (emission linewidth) at threshold. This effect is inherently connected with an increase of temporal coherence.
3. Nonlinear increase of condensate population with increasing pump power just above threshold.
4. Spectral blue-shift of the LP dispersion branch and condensate frequency with increasing pump power due to (repulsive) nonlinear interactions.
5. Multi-mode condensation is possible, i.e. multiple states at different energies but the same spatial location can simultaneously condense [77]. The nonstationary periodic dynamics in polariton condensates associated with multiple frequency components [34, 78] is generally enhanced by a negative detuning, i.e. polariton condensates with large photonic components [79].

3.2.4 Numerical simulation of polariton condensates

The dynamics of interacting many-body systems are generally computationally intractable problems due to the immensely large degrees of freedom present. However, by approximating the interactions in-between particles with that of an effective 'mean field', these problems can greatly be reduced to a one-body system. Computation and even analytical description of many-body systems can then become possible by self-consistent determination of the mean field. In the case of superfluids and superconductors such simplifications have led to the development of the famous Gross-Pitaevski equation (GPE) and the complex Ginzburg Landau equation [80].

The driven-dissipative nature of non-resonantly pumped polariton condensates has led to the development of a generalised GPE (including gain and losses) for the condensate order parameter $\Psi(\mathbf{x},t)$, which is coupled to a rate equation of the uncondensed (exciton) reservoir $n(\mathbf{x},t)$ [81]:

$$i\frac{\partial\Psi(\mathbf{x},t)}{\partial t} = \left\{-\frac{\hbar\nabla^2}{2m} + g|\Psi(\mathbf{x},t)|^2 + g_R n(\mathbf{x},t) + \frac{i}{2}\left[Rn(\mathbf{x},t) - \gamma\right]\right\}\Psi(\mathbf{x},t), \qquad (3.27)$$

$$\hbar\frac{\partial n(\mathbf{x},t)}{\partial t} = \left\{-\gamma_R - R|\Psi(\mathbf{x},t)|^2 + D\nabla^2\right\} n(\mathbf{x},t) + P(\mathbf{x},t). \tag{3.28}$$

In this parabolic regime, m is the LP effective mass, g the polariton-polariton interaction strength, g_R the interaction strength of polaritons and uncondensed reservoir particles, R the scattering rate of reservoir particles into the condensate, and γ and γ_R are the polariton and reservoir decay rates, respectively. The exciton reservoir is further pumped by the term $P(\mathbf{x},t)$ representing the non-resonant excitation laser profile. The reservoir spatial dynamics is captured by the diffusion coefficient D, but it is often neglected ($D \approx 0$) due to the large effective exciton mass, and despite the long exciton lifetime.

3.3 Measures of coherence in polariton condensate systems

We generalise the expression for coherence of coupled oscillators in Eq. 2.13 for continuous variables, such as the fluctuating bosonic field $\Psi(\mathbf{x},t)$ of a polariton condensate. Because there is direct correspondence between the condensate's state described by the wave function $\Psi(\mathbf{x},t)$ and its associated optical field $E(\mathbf{x},t)$ leaking out of the cavity, we can apply the statistical analysis of optical fields [82] to describe coherence properties in polariton condensates. Throughout this theses we interchangeably use the expressions 'condensate density' and 'intensity' of the emitted light to describe density terms, e.g. $|\Psi(\mathbf{x},t)|^2$. In the following we define the relevant statistical quantities:

1. **Mutual coherence function** $\Gamma(\mathbf{x}_1,\mathbf{x}_2,\eta)$
   The mutual coherence function of a stationary field $\Psi(\mathbf{x},t)$ is defined as

   $$\Gamma(\mathbf{x}_1,\mathbf{x}_2,\eta) = \langle\Psi^*(\mathbf{x}_1,t)\Psi(\mathbf{x}_2,t+\eta)\rangle_t\,. \tag{3.29}$$

   This complex-valued quantity describes the first order spatio-temporal correlations of the field between two spatial locations $\mathbf{x}_1$ an $\mathbf{x}_2$ and with a time-offset η. Details on the measurement of the mutual coherence function are given in Section 4.4.2.

2. **Mutual intensity** $\Gamma(\mathbf{x}_1,\mathbf{x}_2)$
   For vanishing time-offset between the two signals, i.e. $\eta = 0$, we drop the time-offset parameter in Eq. 3.29 and denote the equal-time correlation as the mutual intensity,

   $$\Gamma(\mathbf{x}_1,\mathbf{x}_2) = \langle\Psi^*(\mathbf{x}_1,t)\Psi(\mathbf{x}_2,t)\rangle_t\,. \tag{3.30}$$

   The mutual intensity is a complex-valued function, and its argument, $\arg(\Gamma(\mathbf{x},\mathbf{x}))$, is a measure for the average phase difference between the two spatial locations $\mathbf{x}_1$ and $\mathbf{x}_2$. The mutual intensity $\Gamma(\mathbf{x}_1,\mathbf{x}_2)$ of the coherent cavity emission is equivalent to the reduced density matrix $\rho_1(\mathbf{x}_1,\mathbf{x}_2)$ of the polariton many-body system

described in Section 3.2.1. Experimental access to the spatial correlations of the condensate's emitted light field is detailed in Section 4.4.4.

3. **Intensity** $I(\mathbf{x})$
   The equal-time correlations in Eq. 3.30 at the same spatial location $\mathbf{x}_1 = \mathbf{x}_2 = \mathbf{x}$ represent the field intensity (or average condensate density),

$$I(\mathbf{x}) = \Gamma(\mathbf{x}, \mathbf{x}). \tag{3.31}$$

   We further define the intensity function $\hat{I}(\mathbf{k})$ in reciprocal space,

$$\hat{I}(\mathbf{k}) = \left\langle |\hat{\Psi}(\mathbf{k}, t)|^2 \right\rangle_t, \tag{3.32}$$

   where $\hat{\Psi}(\mathbf{k}, t)$ is the Fourier-transformed wavefunction representing the condensate's state in momentum space. Optical measurements of light intensities (or time-averaged condensate densities) in real space and Fourier space are described in Section 4.4.1.

4. **Complex degree of coherence** $g(\mathbf{x}_1, \mathbf{x}_2, \eta)$
   Normalisation of the mutual coherence coherence function in Eq. 3.29 with respect to the field intensities at locations $\mathbf{x}_1$ and $\mathbf{x}_2$ yield the complex degree of coherence,

$$g(\mathbf{x}_1, \mathbf{x}_2, \eta) = \frac{\Gamma(\mathbf{x}_1, \mathbf{x}_2, \eta)}{\sqrt{I(\mathbf{x}_1) I(\mathbf{x}_2)}}. \tag{3.33}$$

   This normalised statistical quantity ($0 \leq |g(\mathbf{x}_1, \mathbf{x}_2, \eta)| \leq 1$) can describe the temporal decay of coherence between two spatial locations $\mathbf{x}_1$ and $\mathbf{x}_2$ with increasing time-offset η. Measurement of the complex degree of coherence are explained in Section 4.4.2.

5. **Complex coherence factor** $g(\mathbf{x}_1, \mathbf{x}_2)$
   For vanishing time-offset between the two signals, i.e. $\eta = 0$, we drop the time-offset parameter in Eq. 3.33 and denote the normalised equal-time correlation as the complex coherence factor,

$$g(\mathbf{x}_1, \mathbf{x}_2) = \frac{\Gamma(\mathbf{x}_1, \mathbf{x}_2)}{\sqrt{I(\mathbf{x}_1) I(\mathbf{x}_2)}}. \tag{3.34}$$

   This complex-valued function describes the system's spatial decay of coherence with increasing distance $|\mathbf{x}_1 - \mathbf{x}_2| \to \infty$. For equal spatial coordinates, i.e. $\mathbf{x}_1 = \mathbf{x}_2 = \mathbf{x}$, the complex coherence factor becomes $g(\mathbf{x}, \mathbf{x}) = 1$. Details on the experimental measurement of the complex coherence factor are given in Section 4.4.4.

6. **Time-resolved correlation functions**
   In case of a non-stationary system, such as a polariton condensates realised under non-resonant pulsed laser excitation, the time-averages $\langle ... \rangle_t$ appearing in Eq. 3.29

and Eq. 3.30 can be replaced by ensemble averages $\langle ... \rangle$, and the relevant statistical quantities become explicitly dependent on the time t. In particular, we define the time-resolved mutual intensity

$$\Gamma(\mathbf{x}_1, \mathbf{x}_2, t) = \langle \Psi^*(\mathbf{x}_1, t)\Psi(\mathbf{x}_2, t) \rangle , \tag{3.35}$$

and its normalised form, the time-resolved complex coherence factor

$$g(\mathbf{x}_1, \mathbf{x}_2, t) = \frac{\Gamma(\mathbf{x}_1, \mathbf{x}_2, t)}{\sqrt{\Gamma(\mathbf{x}_1, \mathbf{x}_1, t)\Gamma(\mathbf{x}_2, \mathbf{x}_2, t)}}. \tag{3.36}$$

Throughout this thesis we either include or drop the time parameter t in the argument of correlation functions to specify the time-resolved or time-averaged measurement. When using time-averages over many system realisations in case of repetitive pulsed laser excitation, the modulus of the time-integrated factor $|g(\mathbf{x}_1, \mathbf{x}_2)|$ [Eq. 3.34] represents a lower bound for the maximum value of the time-resolved complex coherence factor $|g(\mathbf{x}_1, \mathbf{x}_2, t)|$ [Eq. 3.36].

Of interest for the description of coherence in polariton codensates is the relationship between the spatial coherence properties and the condensate density in momentum space,

$$\hat{I}(\mathbf{k}) = \int\int \Gamma(\mathbf{x}_1, \mathbf{x}_2) e^{i\mathbf{k}\mathbf{x}_1} e^{-i\mathbf{k}\mathbf{x}_2} \mathrm{d}\mathbf{x}_1 \mathrm{d}\mathbf{x}_2. \tag{3.37}$$

In the context of an optical setup with a partially coherent light source this equality is also known as the 'Van Cittert-Zernike theorem'. The Fourier-transform pairing between intensity distribution in reciprocal space and its spatial correlations in real space stated in Eq. 3.37 implies important reciprocal width relations:

- Long-range spatial coherence $\leftrightarrow$ Narrow density in momentum space.

- Short-range spatial coherence $\leftrightarrow$ Broad density in momentum space.

We note that the formation of ODLRO during condensation of exciton polaritons, i.e. formation of long-range spatial coherence, is inherently tied up with a narrowing of the system's angular emission pattern $\hat{I}(\mathbf{k})$. This principle becomes apparent in our discussion of coherence in coupled polariton condensates in Chapter 6, where we compare both condensate momentum density distribution and condensate spatial coherence properties.

Chapter 4

Experimental Methods

In this thesis we present networks and lattices of non-resonantly excited polariton condensates in a planar semiconductor microcavity. Hereby, spatially separated and tightly-pumped polariton condensates show mutual ballistic flow of polaritons from one condensate to another one, giving rise to particle exchange-based interactions. The general scheme for generation of polariton condensate lattices with individual control over couplings is illustrated in Fig. 4.1. We spatially shape two Gaussian laser beams into an optical excitation pattern of polariton condensates (red coloured spots) and potential barriers (blue coloured spots). While each of the condensate nodes is pumped by a tightly-focused laser spot with pump power exceeding the threshold pump power $P > P_{\text{thr}}$, the barrier beams only generate incoherent exciton reservoirs below the condensate threshold $P < P_{\text{thr}}$ affecting the in-plane particle flows. It is the precise optical control over the complex-valued (i.e. non-Hermitian) potential landscape of polariton condensates that allows us to steer and study the synchronisation patterns arising in coupled condensate structures. In the following we describe the experimental methods for optical generation, modulation and read-out of coupled polariton condensates.

We begin in Section 4.1 by describing the planar semiconductor microcavity sample used for the experimental studies presented in this thesis. The methods for laser beam shaping are presented in Section 4.2 including a description of optical feedback for stabilisation of the spatial pump geometry. A general layout for the optical excitation setup is shown and described in Section 4.3. Lastly, the optical techniques for measurements of density, energy, phase, and coherence in coupled polariton condensate systems are presented in Section 4.4.

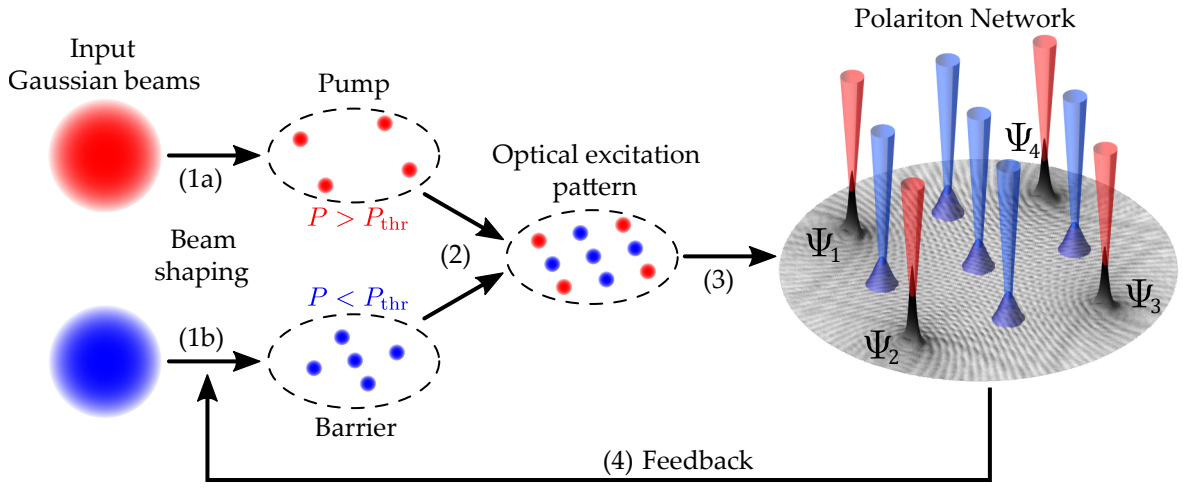

FIGURE 4.1: **Generation of polariton graphs with control over individual coupling parameters using optically generated potential barriers.** Two non-resonant Gaussian beams are modulated (1a,1b) using two SLMs to form the (red coloured) pump geometry of polariton condensates, and the (blue coloured) spatial geometry of potential barriers. Upon combination (2) of the two laser profiles and focusing of the total graph onto the microcavity sample, a network of coupled polariton condensates is generated (3). While each of the pump beams excites a condensate of polaritons with pump power above the condensation threshold $P > P_{thr}$, the barrier beams only generate locallly confined exciton reservoirs below condensation threshold $P < P_{thr}$. Feedback (4) of the polariton emission can be integrated into the beam shaping process leading to a closed-loop algorithm for generation of stabilised polariton lattices.

4.1 Microcavity Sample

Semiconductor microcavities based on GaAs/AlAs heterostructures are preferred systems for realising high Q-factor cavities due to the large bandgap difference and small lattice mismatch between GaAs and AlAs layers. Interestingly, these structures have been reported to yield Q-factors exceeding $300,000$ and polariton lifetimes beyond 100 ps giving access to condensation of exciton-polaritons in thermal equilibrium [76]. Such a low-loss microcavity was realised by increasing the DBR thickness to up to 40 pairs of $\lambda/4$ layers. In another approach, increased quality factors and particle propagation distances can be realised by reducing the strain-induced defects such as crosshatch dislocations present in GaAs/AlAs heterostrucures due to their small remaining lattice mismatch [83]. It was demonstrated that reduction of strain and, thus, suppression of dislocation patterns can be realised by introducing AlP layers into the centre of the AlAs DBR layers [84]. All experiments presented in this thesis are performed on such a strain-compensated planar microcavity [85] facilitating the macroscopic polariton propagation distances and condensate coupling distances exceeding 100 µm described in Chapter 5 and Chapter 6. The structure of this microcavity is grown on a GaAs substrate and its architecture is schematically drawn in Fig. 4.2. It consists of a 2λ-GaAs cavity with 6 embedded $In_{0.08}Ga_{0.92}As$ QWs located at the antinodes of the modal field distribution. Two additional QWs are located at the first and last nodes of

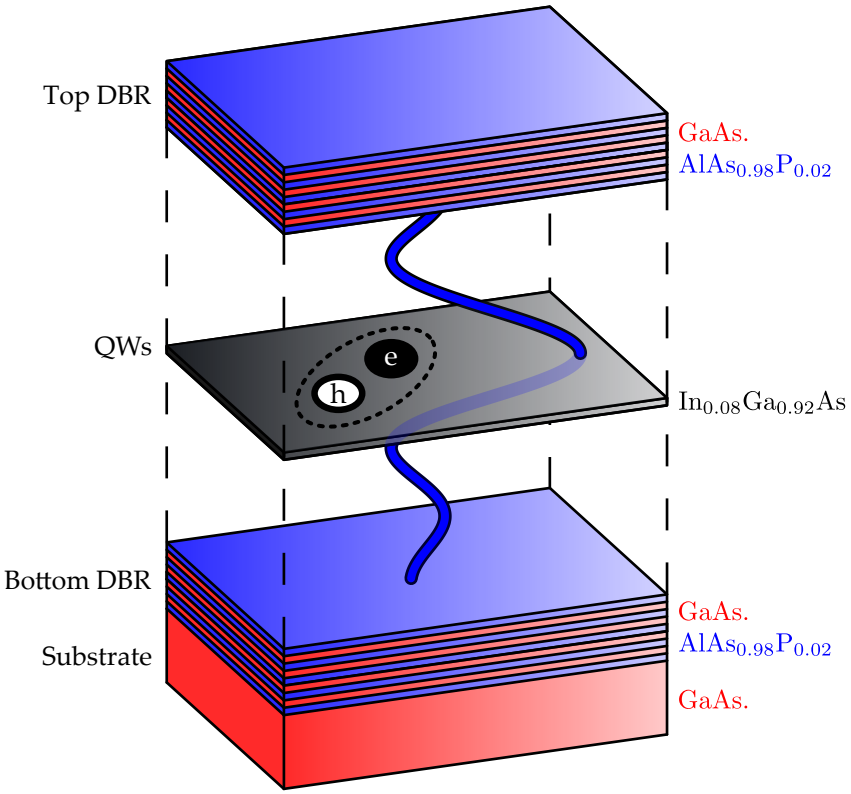

FIGURE 4.2: **Schematic of the microcavity sample used for the results presented throughout this thesis.** Details of the sample are presented in Ref. [85].

the field distribution for carrier collection. The presence of Indium in the QWs lowers the emission energy below the GaAs substrate bandgap energy which allows measurements in transmission geometry. The reflectivity stopband ($\lambda \approx 800 - 900$ nm) of the cavity is formed by 26 pairs of $AlAs_{0.98}P_{0.02}$/GaAs layers for the top DBR and 23 equivalent pairs for the bottom DBR. Strong coupling between bare cavity and exciton modes is provided by a Rabi splitting of 8 meV. An additional wedge in the cavity thickness gives access to a controllable cavity-exciton detuning parameter Δ from -8 meV to 1 meV. Measurements presented throughout this thesis are performed at a detuning of $\Delta \approx -5$ meV with LP ground state emission at $\lambda \approx 858$ nm.

This sample was designed and fabricated under the directions of P. G. Lagoudakis and W. Langbein. Characterisation and demonstration of strong coupling and polariton condensation in this sample are reported in Ref. [85]. The structure's quality factor is experimentally determined as $Q \approx 12,000$. Following from Eq. 3.5, the particle lifetime can be estimated as $\tau \approx 5$ ps.

4.2 Beam shaping using Spatial Light Modulators

The spatial transformations of Gaussian laser beams into designated geometries for pumps and barriers are accomplished using phase-only spatial light modulators (SLMs).

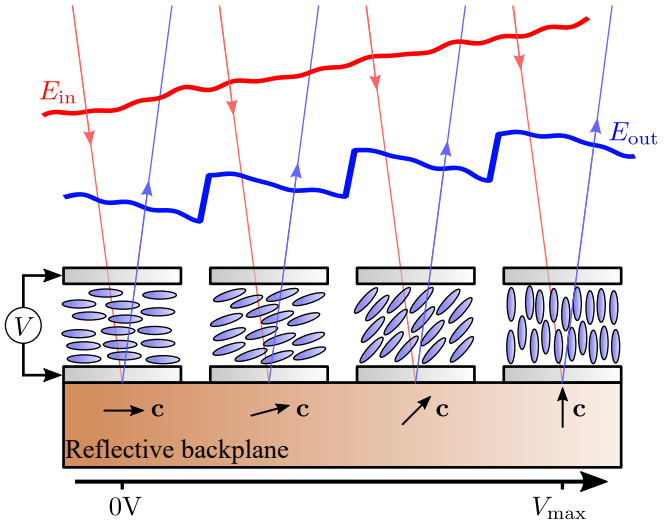

FIGURE 4.3: **Operational principle of a reflective spatial light modulator.** An incoming wavefront E_{in} is phase-modulated upon reflection from the liquid crystal cells, where the voltage V of each cell determines the orientation of its optical axis **c** and phase shift of the outgoing wave E_{out}.

Working principle of phase-only SLMs and iterative algorithms for digital control over the transformed laser beam shape are described in the following.

The computer-controlled spatial wavefront modulators in use throughout this thesis are reflective liquid crystal displays, i.e. electrically-tuneable arrays of liquid crystal cells. A simplified schematic of such an SLM is illustrated in Fig. 4.3. Each cell is filled with rod-like birefringent molecules, whose molecular orientation is controlled through an externally applied voltage V. Birefringence is the optical property of a material having different refractive indices parallel n_o and perpendicular n_e to the material's optical axis **c**. In case of the liquid crystal cells displayed in Fig. 4.3 the optical axis **c** of each cell is determined by the liquid crystals' macroscopic molecular orientation and lies within the image plane. An optical wave with linear polarisation lying in the plane spanned by the orientations of **c**, i.e. in the image plane of Fig. 4.3, feels the effective refractive index

$$n(\alpha) = \frac{n_o n_e}{\sqrt{n_o^2 \sin^2(\alpha) + n_e^2 \cos^2(\alpha)}}, \tag{4.1}$$

where α is the angle between the optical waves propagation direction and **c**. Thus, via a spatial modulation of the externally applied voltage $V(\mathbf{x})$, a tuneable phase-retardance $\phi(\mathbf{x})$ for the reflected electric field $E(\mathbf{x})_{\text{out}}$ can be achieved, i.e.

$$E_{\text{out}}(\mathbf{x}) = E_{\text{in}}(\mathbf{x}) e^{i\phi(\mathbf{x})}. \tag{4.2}$$

Here, we have neglected any losses that appear during reflection of the incoming wave E_{in} from the spatial light modulator. The spatially controllable phase shift in each cell is given as $\phi(\alpha) = 2\pi d n(\alpha)/\lambda$, where λ is the optical wavelength and d is the cells

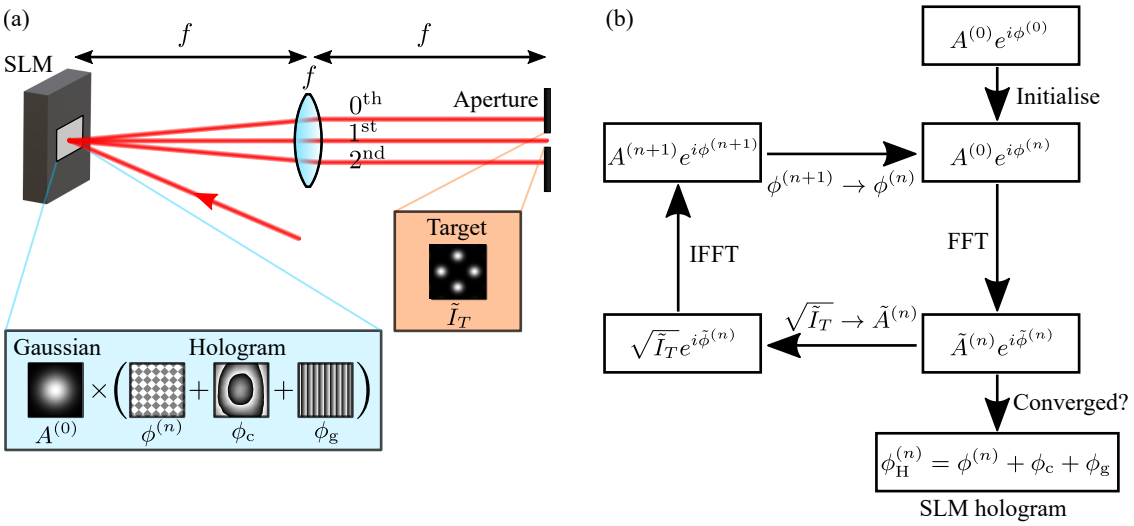

FIGURE 4.4: **Beam shaping using an SLM.** (a) Simple setup depicting the experimental shaping of a Gaussian input beam (SLM plane) into a square arrangement of 4 Gaussian beams (target plane). (b) Iterative Gerchberg-Saxton algorithm for calculation of a phase pattern $\phi^{(n)}$ which is determined by the target intensity map $\tilde{I}_T$.

effective thickness taking into account that the wave is travelling twice through each liquid crystal cell.

The experimental implementation of beam shaping using a reflective phase-only SLM is illustrated in Fig. 4.4(a). The wavefront of an incoming Gaussian beam with field amplitude $A^{(0)}(\mathbf{x})$ is spatially modulated upon reflection from the SLM, where the applied phase-hologram $\phi_H(\mathbf{x})$ (or just hologram) is given by an 8-bit grey level pattern, i.e. a 2π phase modulation is digitized into 256 bit levels. A thin lens of focal length f is used to create the Fourier transform of the phase-modulated field at a distance $2f$ after the SLM. In the following we denote the two planes at a focal distance f before and after the lens as SLM plane and target plane, respectively. While the field at the SLM plane is given as the phase-modulated incoming field, $E_{\text{SLM}} = E_{\text{in}} \exp(i\phi_H)$, the field at the target plane E_T reads as

$$E_T(\mathbf{x}) = \mathcal{F}_s \{E_{\text{SLM}}(\mathbf{s})\} (\frac{2\pi\mathbf{x}}{\lambda f}), \tag{4.3}$$

where $\mathcal{F}_\mathbf{s} \{f(\mathbf{s})\} (\mathbf{x})$ denotes the two-dimensional Fourier transform of function $f(\mathbf{s})$ with respect to $\mathbf{s}$. The inverse relationship of Eq. 4.3 holds,

$$E_{\text{SLM}}(\mathbf{x}) = \mathcal{F}_\mathbf{s}^{-1} \{E_T(\mathbf{s})\} (\frac{2\pi\mathbf{x}}{\lambda f}), \tag{4.4}$$

where $\mathcal{F}_\mathbf{s}^{-1} \{f(\mathbf{s})\} (\mathbf{x})$ denotes the inverse Fourier transform.

4.2.1 Gerchberg-Saxton algorithm

In the following, we describe the computational approach of designing a holographic phase pattern $\phi_H(\mathbf{x})$, which in the experimental realisation depicted in Fig. 4.4(a) allows to transform the incoming Gaussian beam into a designated target intensity pattern $\tilde{I}_T(\mathbf{x})$ at the target plane. Within the work presented in this thesis these target intensity patterns $\tilde{I}_T(\mathbf{x})$ are typically composed of arrays (and lattices) of Gaussian spots, each of them representing either a condensate pump node or a potential barrier. We note that due to the non-resonant excitation scheme applied in our experiment, only the intensity pattern $\tilde{I}_T(\mathbf{x})$ of the target pattern is of concern, while its phase has no implication on the excited condensate system. We utilise the popular Gerchberg-Saxton (GS) algorithm [86], an iterative Fourier-transforming algorithm, to compute SLM phase holograms $\phi_H(\mathbf{x})$ for approximate solutions of the equivalence between the obtained intensity $|E_T(\mathbf{x})|^2$ of the computed target field in Eq. 4.3 and the designated target intensity pattern $\tilde{I}_T(\mathbf{x})$.

The algorithm [schematically shown in Fig. 4.4(b)] begins with the initialisation of a 2D complex-valued field of amplitude $A^{(0)}(\mathbf{x})$ and phase $\phi^{(0)}(\mathbf{x})$, which represent the field of the input laser beam at the SLM plane. We assume a flat phase-front $\phi^{(0)}(\mathbf{x}) = 0$ and a Gaussian amplitude $A^{(0)}(\mathbf{x})$, whose width matches the laser beam width. The core of the algorithm consists of a loop in which cyclic operations of Fourier and inverse Fourier transformations link the fields between SLM and target plane. Each iteration step n begins with propagation of the field $A^{(0)} \exp(i\phi^{(n)})$ from the SLM plane to the target plane by means of a fast Fourier transform (FFT), resulting in the complex-valued field $\tilde{A}^{(n)} \exp(i\tilde{\phi}^{(n)})$. Here, for differentiation between SLM plane and target plane, we add the tilde diacritic to fields in the (Fourier-transformed) target plane. The amplitude $\tilde{A}^{(n)}$ is replaced with the amplitude of the designated target intensity pattern, i.e. $\sqrt{\tilde{I}_T} \rightarrow \tilde{A}^{(n)}$, and back propagation to the SLM is computed by means of an inverse fast Fourier transform (IFFT) yielding a complex field with amplitude $A^{(n+1)}$ and phase $\phi^{(n+1)}$. At the end of each iteration step n, the newly computed phase field $\phi^{(n+1)}$ is kept and replaces the initial phase pattern of the previous iteration step, i.e. $\phi^{(n+1)} \rightarrow \phi^{(n)}$.

Convergence of the algorithm, as well as a certain level of congruence between the obtained intensity target pattern $|\tilde{A}^{(n)}|^2$ and the designated target intensity pattern $\tilde{I}_T(\mathbf{x})$ is usually reached after a few tens of iterations, such that execution can be stopped. The phase pattern $\phi^{(n)}(\mathbf{x})$, that was calculated after n iteration steps of the GS algorithm, is then combined with additional device and setup dependent phase correction terms $\phi_c(\mathbf{x})$, and a blazed grating $\phi_g(\mathbf{x})$ to yield the SLM phase hologram for our experiment, i.e.

$$\phi_H(\mathbf{x}) = \phi^{(n)} + \phi_c(\mathbf{x}) + \phi_g(\mathbf{x}). \tag{4.5}$$

The phase correction term ϕ_c compensates optical aberrations in the optical setup, and aberrations due to the non-flatness of the SLM screen. The phase grating ϕ_g spatially displaces the phase-modulated laser beam (1st diffraction order) in the target plane from the unmodulated reflected beam (0th order) and higher-order diffraction orders and, thus, allows to block the unwanted orders using an aperture as depicted in Fig. 4.4(a).

It is important to note, that even when aiming for a target laser spot pattern with homogeneous spot intensities, due to the technically limited accuracy of the GS algorithm, and unavoidable remaining optical aberrations due to misalignment and device imperfections, the resultant experimentally obtained pump spot intensity distribution can strongly deviate from the homogeneous target. In the next section we describe a method to include feedback of the experimentally recorded laser spot pattern for stabilisation of the spot intensities.

4.2.2 Spatial stabilisation of pump intensity

A schematic of the closed-loop algorithm taking into account feedback from the experimentally measured laser spot intensity distribution is shown in Fig. 4.5. Its implementation is similar to the schemes published in Refs. [87] and [88] with applications in the field of cold atom trapping. The algorithm is a modified version of the conventional GS algorithm presented in Fig. 4.4(b), in which a nonlinear adjustment of the target intensity pattern $\tilde{I}_T(\mathbf{x})$ in each iteration cycle controls the convergence to a homogeneous spot intensity distribution.

Within each iteration cycle n of the conventional GS cycle [orange box in Fig. 4.5(a)] we apply the current phase-hologram ϕ_H [see Eq. 4.5] onto the SLM and, subsequently, record the current spatial distribution of the laser beam in the target plane using a camera. We extract the measured intensity $I_{\mathrm{M},j}^{(n)}$ of each laser spot $j = 1, ..., N$ by integrating the camera counts within the beam waist of each spot. The target intensity $I_{\mathrm{T},j}^{(n+1)}$ for each laser spot j is then updated for the next iteration cycle $n+1$ utilising a nonlinear function,

$$I_{\mathrm{T},j}^{(n+1)} = \frac{I_{\mathrm{T},j}^{(n)}}{1 + \epsilon \left(\frac{I_{\mathrm{M},j}^{(n)}}{\left\langle I_{\mathrm{M}}^{(n)} \right\rangle} - 1 \right)}. \tag{4.6}$$

Here, $\left\langle I_{\mathrm{M}}^{(n)} \right\rangle$ represents the mean of the measured laser spot intensities and $\epsilon \geq 0$ is an adjustable feedback parameter. The nonlinear function in Eq. 4.6 lowers (raises) the target spot power $I_{\mathrm{T},j}^{(n+1)}$ of each spot j, when its measured intensity is larger (lower) than the average. In the next step, the two dimensional target intensity map $\hat{I}_T^{(n+1)}(\mathbf{x})$ is calculated and consists of the superposition of N Gaussian spots, where the amplitude of each spot is determined by the calculated spot intensities $I_{\mathrm{T},j}^{(n+1)}$ and the width of each

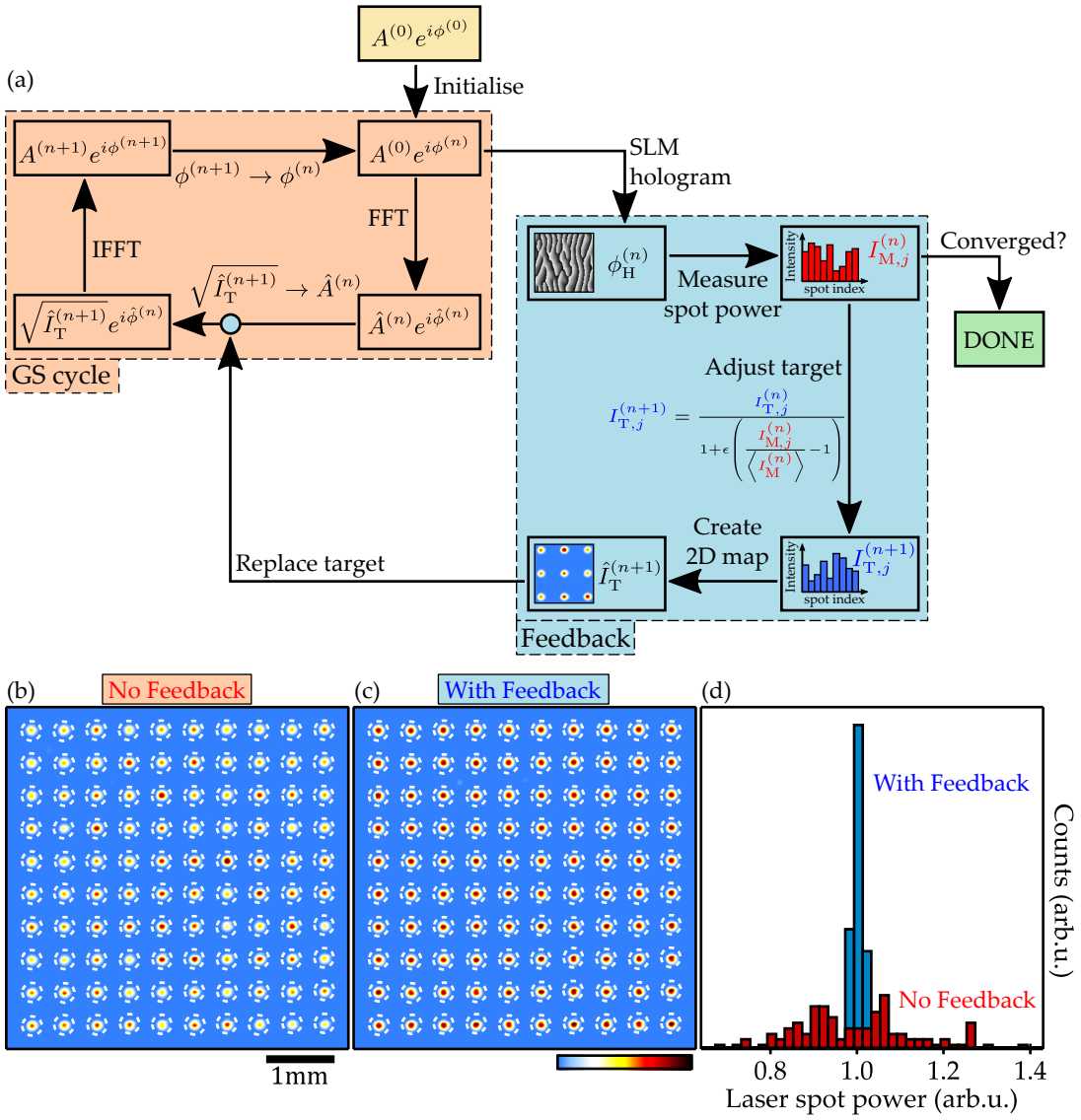

FIGURE 4.5: **Closed-loop feedback algorithm for spatial stabilisation of laser spot intensities.** (a) Schematic of the algorithm. Experimentally recored intensity patterns of a square lattice of laser spots after (b) 100 iterations of the conventional GS algorithm and (c) 100 iterations of the modified GS algrotuhm including feedback. (d) The extracted spread of spot power distribution for both algorithms. Adapted from Ref. [89]

spot is related to the Gaussian width of the laser profile $A^0(\mathbf{x})$ on the SLM by means of a Fourier transform. This updated intensity map then feeds back into the GS cycle, replacing the amplitude function $A^{(n)}(\mathbf{x})$ in the target plane.

The feedback parameter ϵ in Eq. 4.6 controls the speed of convergence to a homogeneous distribution of spot intensities, but cannot be set too large to avoid destabilisation of the algorithm. We find empirically that a value of ϵ in the range of $10^{-2} - 10^{-1}$ allows for both, spatial stabilisation of a laser spot pattern and spatial stabilisation of a non-resonanlty excited lattice of polariton condensates as discussed in Chapter 6. For $\epsilon = 0$ there is no change in target spot intensities, i.e. the pattern is fixed by the initial

target $I_{\mathrm{T},j}^{(n)} = I_{\mathrm{T},j}^{(0)}$, and the algorithm corresponds to the conventional form of the GS algorithm. Execution of the algorithm is stopped once the spread of measured spot intensities $I_{\mathrm{M},j}^{(n)}$ reaches a threshold of 1% relative standard deviation (RSD) typically achieved within less than 100 iterations. Execution of the Fourier transform algorithm on the graphics processing unit (GPU) allows for cycle periods in the order of 100 ms, i.e. spatial stabilisation of laser spot patters (or polariton condensate lattices) within less than 1 minute.

In Figs. 4.5(b) and 4.5(c) we show the experimentally recorded laser spot pattern after 100 iterations of the conventional GS algorithm (no feedback) and after 100 iterations of the modified GS algorithm (including feedback), respectively. In both cases the initial target pattern is a homogeneous 10×10 square lattice with equal spot intensities. Due to device imperfections, optical aberrations and the limited accuracy of the GS algorithm there is a non-homogenous distribution of spot intensities with a spread of 15% RSD as shown in Fig. 4.5(c). These detrimental effects are counteracted when applying the described active spatial stabilisation of spot intensities. The homogeneous lattice depicted in Fig. 4.5(c) shows a reduced spread of spot intensities with only 1% RSD.
While we have mainly focused here on spatial stabilisation of laser spot intensities in the target plane of an experimental setup, the algorithm also allows to stabilise PL intensities in optically excited polariton condensate lattices as presented in Chapter 6 of this thesis. We point out, that demonstration and description of this algorithm for emission intensity stabilisation in lattices of polariton condensates is published in Reference [89] and its supplemental material.

4.3 Excitation of polariton condensate networks

Experiments presented in this thesis rely on optical excitation of polariton condensates using non-resonant lasers. While for smaller-size systems a single-mode continuous wave (cw) laser yields enough excitation power for excitation of up to ≈ 50 coupled condensate nodes, for larger lattices (> 100 condensate nodes) excitation is performed using a mode-locked pulsed laser with 80 MHz repetition rate and ≈ 150 fs pulse duration. A schematic of the experimental setup for excitation of polariton condensate networks is shown in Fig. 4.6. Both coherent excitation light sources (labelled as Laser 1 and Laser 2) operate at the first reflection minimum above the cavity reflection stop band ($\lambda \approx 800$ nm). Using a flippable mirror allows to selectively chose between cw or pulsed excitation. An additional acousto-optic modulator (AOM) is used in connection with the cw laser to generate square wave pulses of typically 10 kHz repetition rate and 5% duty cycle to avoid sample heating under cw excitation. The resulting effective pulse length of ≈ 5 µs is orders of magnitude above the typical picosecond timescale of polariton condensates, i.e. excitation can still be regarded as stationary.

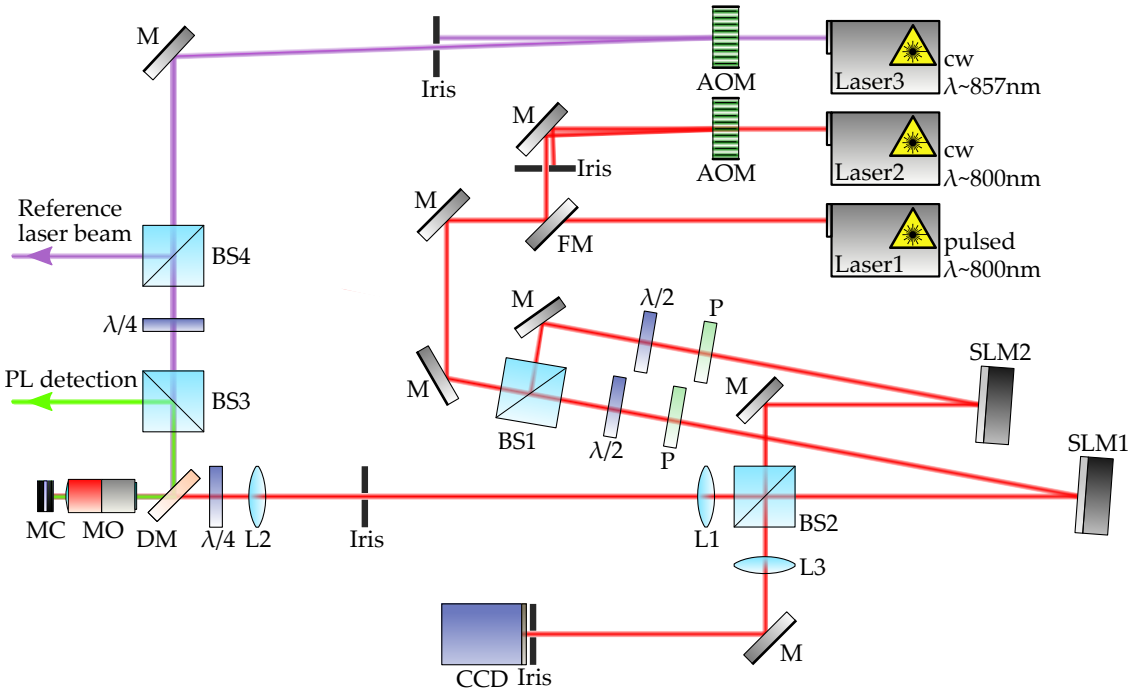

FIGURE 4.6: **Schematic of the optical excitation setup.** Optical paths of the nonresonant pump laser beams are illustrated in red colour, the polariton PL in green colour, and the resonant (seeding) laser beam in purple colour. Abbreviations: Acousto optic modulator (AOM), mirror (M), flippable mirror (FM), lens (L), beam splitter (BS), half-wave plate ($\lambda/2$), quarter-wave plate ($\lambda/4$), polariser (P), spatial light modulator (SLM), dichroic mirror (DM), microscope objective lens (MO), microcavity (MC), charge-coupled device (CCD), photoluminescence (PL).

A beam splitter (BS1) splits the excitation laser source into two paths, each of them containing a reflective SLM. Both SLMs are operated in the Fourier plane of the optical excitation setup and are used to engineer networks (or lattices) of Gaussian laser spots as detailed in Section 4.2. We utilise one of the modulators (SLM1) to generate pump geometries for non-resonantly excited polariton condensate networks, and the other modulator (SLM2) to independently modify non-resonantly imprinted potential barriers for the polariton condensate (see Chapter 7). Rotation of half-wave plates in front of a polariser allows to control the laser power in each path, while the polarisation axis matches the liquid crystal director axis. Two lenses (L1) and (L2) are used to project both SLM planes onto the back aperture of the microscope objective lens (20x, 0.4NA, infinity corrected). An additional quarter-wave plate transforms the excitation laser polarisation in circular polarisation. We project the far field (Fourier plane) of both SLMs onto a charge-coupled device (CCD) image sensor to spatially record both laser geometries. The microcavity sample is held in a cold finger cryostat at low temperatures ($T \approx 6$ K, mounted using thermally conductive silver paste), and polariton PL is collected in reflection geometry and separated from the excitation laser using a dichroic mirror at an angle of 45°. The PL detection schemes (not shown in Fig. 4.6) are presented in Section 4.4.

An additional cw laser source (Laser 3, $\lambda \approx 857$ nm) is used for resonant injection of polaritons in conjunction with our non-resonant excitation schemes. As detailed in Chapter 7 and presented in Ref. [90] we utilise this weak resonant laser matching the ≈ 2 μm beam waist of a non-resonantly excited polariton condensate to lock the phase of one condensate to that of the coherent seed laser. Part of this seeding laser beam is diverted using a beam splitter (BS4) and serves as a coherent reference wave for use in interferometric analysis (phase extraction) of the polariton condensate network (see Section 4.4.3).

4.4 Detection of polariton condensate networks

While the inherited photonic component of microcavity polaritons leads to short (picosecond) particle lifetimes, the optical losses allow in-situ optical characterisation of a polariton condensate with typical measurements of condensate density, energy, polarisation and coherence. The experimental setups and methods for measurement and extraction of these characteristics are presented in the following.

4.4.1 Imaging techniques

Experimental access to the condensate's real space density $|\Psi(\mathbf{x})|^2$ and Fourier space density $|\hat{\Psi}(\mathbf{x})|^2$ is realised by near field and far field imaging techniques as schematically illustrated in Figs. 4.7(a) and 4.7(b). Here, the cavity emission is collected by an infinity corrected microscope objective lens and either the near field (or real space), or the far field (or Fourier space) are projected onto the image plane of our detection setup using either one or two lenses. Using a CCD camera image sensor at the image plane we record then either the time-integrated real space condensate density, i.e. $I(\mathbf{x}) = \langle|\Psi(\mathbf{x})|^2\rangle_t$, or the time-integrated Fourier space density, i.e. $\hat{I}(\mathbf{k}) = \langle|\hat{\Psi}(\mathbf{k})|^2\rangle_t$. In case of pulsed excitation (80 MHz) and with typical camera exposure times in the order of $10 - 100$ ms this corresponds to an average over millions of realisations of the condensate system.

Additionally, by projecting the real space or Fourier space emission signals onto the entrance slit of an imaging spectrometer we can measure the spectrally-resolved condensate densities along the slit direction as shown in Figs. 4.7(c) and 4.7(d). Assuming that the slit is oriented in vertical direction and centred at $x = 0$ or $k_x = 0$, respectively, the measurable quantities are the spectral densities $|\hat{\Psi}(x = 0, y, E)|^2$ and $|\hat{\Psi}(k_x = 0, k_y, E)|^2$, where the latter is also denoted as the systems dispersion image.

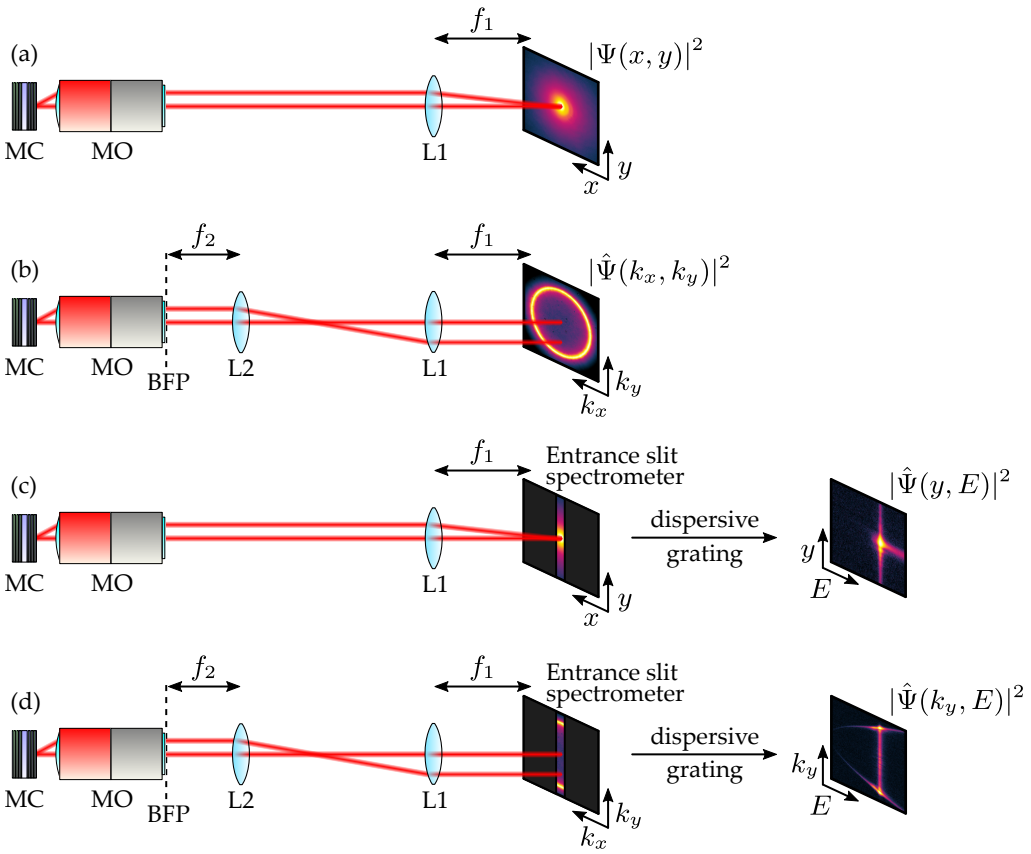

FIGURE 4.7: **Optical detection schemes for analysis of polariton condensates.** Light emitted out of the microcavity (MC) is collected by a microscope objective lens (MO) and imaged via one or two lenses (L1,L2) with focal lengths f_1 and f_2 to project the condensate's (a) real space or (b) Fourier space density onto the image plane. The back focal plane (BFP) of the MO is illustrated as a black dashed line. Placing the entrance slit of an imaging spectrometer at the image plane the spectrally resolved emission in (c) real or (d) Fourier plane can be measured.

4.4.2 Measurement of temporal coherence

In this section we describe an interferometric method to extract both the mutual coherence factor $\Gamma(\mathbf{x}, -\mathbf{x}, \eta)$ and its normalised form, the complex degree of coherence $g(\mathbf{x}, -\mathbf{x}, \eta)$. Scanning of the time-offset parameter η allows to measure the temporal decay of coherence (or coherence time) in polariton condensates.

We utilise a modified Michelson interferometer, which is depicted in Fig. 4.8(d), and contains a retro reflector mounted on a translational stage to control the relative path length between the two interferometer arms. A CCD image sensor records the real space intensity pattern $I_1(\mathbf{x})$ or $I_2(\mathbf{x})$ when either one of the interferometer arms is blocked. Example images of $I_1(\mathbf{x})$ and $I_2(\mathbf{x})$ representing a Gaussian-shaped polariton condensate formed in an optical trap are shown in Fig. 4.8(a) and Fig. 4.8(b). Because the retro reflector placed in arm 2 of the interferometer inverts the intensity pattern

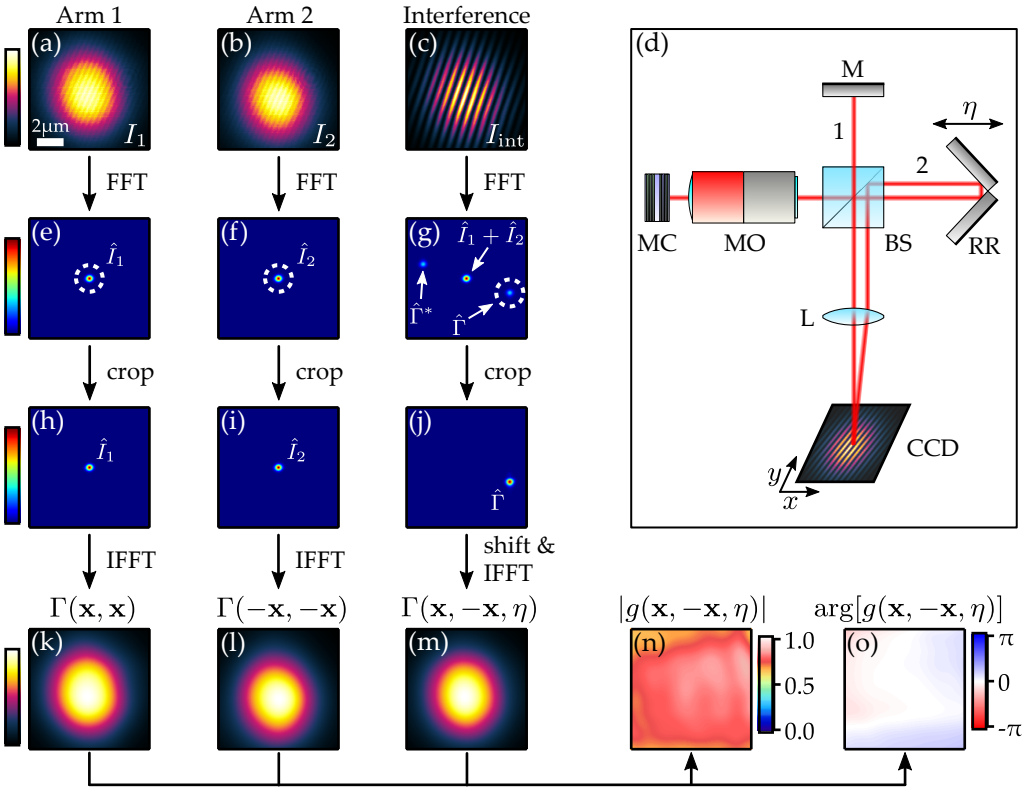

FIGURE 4.8: **Coherence measurements in a Michelson interferometer.** Intensity patterns of the emission a Gaussian polariton condensate passing through (a) arm 1 only, (b) arm 2 only, and (c) both interferometer arms simultaneously. A schematic of the interferometer with adjustable time-delay η is shown in (d). Arm 2 contains a retro reflector inverting the image acquired by the CCD image sensor. (e-g) Digitally computed fast Fourier transforms of (a-c). (h-j) Spatially filtered Fourier images. (k-m) Correlation functions Γ computed by inverse fast Fourier transformation of (h-j). Magnitude (n) and argument (o) of the complex degree of coherence $g(\mathbf{x},-\mathbf{x},\eta)$.

recorded by the CCD image sensor, we can write

$$I_1(\mathbf{x}) = I(\mathbf{x}), \tag{4.7}$$

$$I_2(\mathbf{x}) = I(-\mathbf{x}), \tag{4.8}$$

where $I(\mathbf{x}) = \langle|\Psi(\mathbf{x},t)|^2\rangle_t$ denotes the condensate emission intensity. Importantly, the signal coming from arm 2 impinges onto the recording CCD image sensor at an angle determined by the transverse wavevector $\mathbf{k}_\parallel$. This transverse wavevector is controllable by offsetting the retro reflector lateral position from the optical axis as illustrated in Fig. 4.8(d). The interference signal $I_{\mathrm{int}}(\mathbf{x})$, i.e. neither of the interferometer arms is blocked, is shown in Fig. 4.8(c) and can be written as

$$\begin{aligned} I_{\mathrm{int}}(\mathbf{x}) &= \langle|\Psi(\mathbf{x},t) + e^{i\mathbf{k}_\parallel\mathbf{x}}\cdot\Psi(-\mathbf{x},t+\eta)|^2\rangle_t \\ &= I_1(\mathbf{x}) + I_2(\mathbf{x}) + e^{i\mathbf{k}_\parallel\mathbf{x}}\cdot\Gamma(\mathbf{x},-\mathbf{x},\eta) + e^{-i\mathbf{k}_\parallel\mathbf{x}}\cdot\Gamma^*(\mathbf{x},-\mathbf{x},\eta). \end{aligned} \tag{4.9}$$

It is apparent from Eq. 4.9 that visibility of interference fringes, whose geometrical orientation is defined by $\mathbf{k}_{\parallel}$, depends on the coherence function Γ. Therefore, Fourier-analysis of the recorded interferogram allows extraction of the mutual coherence function as explained in the following.

The two-dimensional Fourier transformation of the interference signal in Eq. 4.9 is written as

$$\hat{I}_{\text{int}}(\mathbf{k}) = \hat{I}_1(\mathbf{k}) + \hat{I}_2(\mathbf{k}) + \hat{\Gamma}(\mathbf{k} - \mathbf{k}_{\parallel}, \eta) + \hat{\Gamma}^*(-\mathbf{k} + \mathbf{k}_{\parallel}, \eta), \tag{4.10}$$

where the hat diacritic denotes the spatial Fourier transform of intensity $I_{1,2}$ and coherence function Γ, respectively. Digital FFT of the recorded interference signal is illustrated in Fig. 4.8(g). One can see that the off-axis displacement of $\hat{\Gamma}(\mathbf{k} - \mathbf{k}_{\parallel}, \eta)$ in Fourier space allows to filter this component as long as the displacement vector $\mathbf{k}_{\parallel}$ is sufficiently larger than any relevant spatial frequency components in $I_{1,2}$ and Γ. We spatially filter the relevant component in the FFT image using a circular mask depicted in Fig. 4.8(g) in white dashed. Subsequent shifting of the Fourier-filtered component into the centre of the image, i.e. $\hat{\Gamma}(\mathbf{k} - \mathbf{k}_{\parallel}, \eta) \rightarrow \hat{\Gamma}(\mathbf{k}, \eta)$, and computation of the IFFT yields the mutual coherence function $\Gamma(\mathbf{x}, -\mathbf{x}, \eta)$ shown in Fig. 4.8(m).

Furthermore, we apply an equivalent circular mask to the Fourier-images of the recorded reference images I_1 and I_2 displayed in Fig. 4.8(e) and Fig. 4.8(f). The spatially centred mask filters large-frequency components in the images of $\hat{I}_1$ and $\hat{I}_2$ analogous to the filtering of spatial frequencies of the interferogram shown in Fig. 4.8(g). The resulting Fourier-filtered intensity patterns $I(\mathbf{x}) = \Gamma(\mathbf{x}, \mathbf{x})$ and $I(-\mathbf{x}) = \Gamma(-\mathbf{x}, -\mathbf{x})$ are displayed in Fig. 4.8(k) and Fig. 4.8(l). Subsequently, we calculate the complex degree of coherence $g(\mathbf{x}, -\mathbf{x}, \eta)$ as described in Eq. 3.33. Extracted magnitude $|g|$ and argument $\arg(g)$ of the Gaussian shaped polariton condensate are shown in Fig. 4.8(n) and Fig. 4.8(o), respectively.

Scanning of the relative path length-difference between the two interferometer arms allows measurement of the temporal change of the complex degree of coherence $g(\eta)$. The system's coherence time τ_c is determined by the decay of coherence and defined as

$$\tau_c = \int_{-\infty}^{\infty} |g(0, 0, \eta)|^2 \mathrm{d}\eta, \tag{4.11}$$

where we have chosen the centre of symmetry $\mathbf{x} = 0$ as a reference point.

4.4.3 Phase Measurement in coupled condensate networks

Measurements using a recording CCD image sensor (such as presented in Fig. 4.7) yield information about the condensate density $|\Psi(\mathbf{x})|^2$, however, access to the condensate phase distribution $\arg[\Psi(\mathbf{x})]$ is not obtained. Instead, interference of the condensate

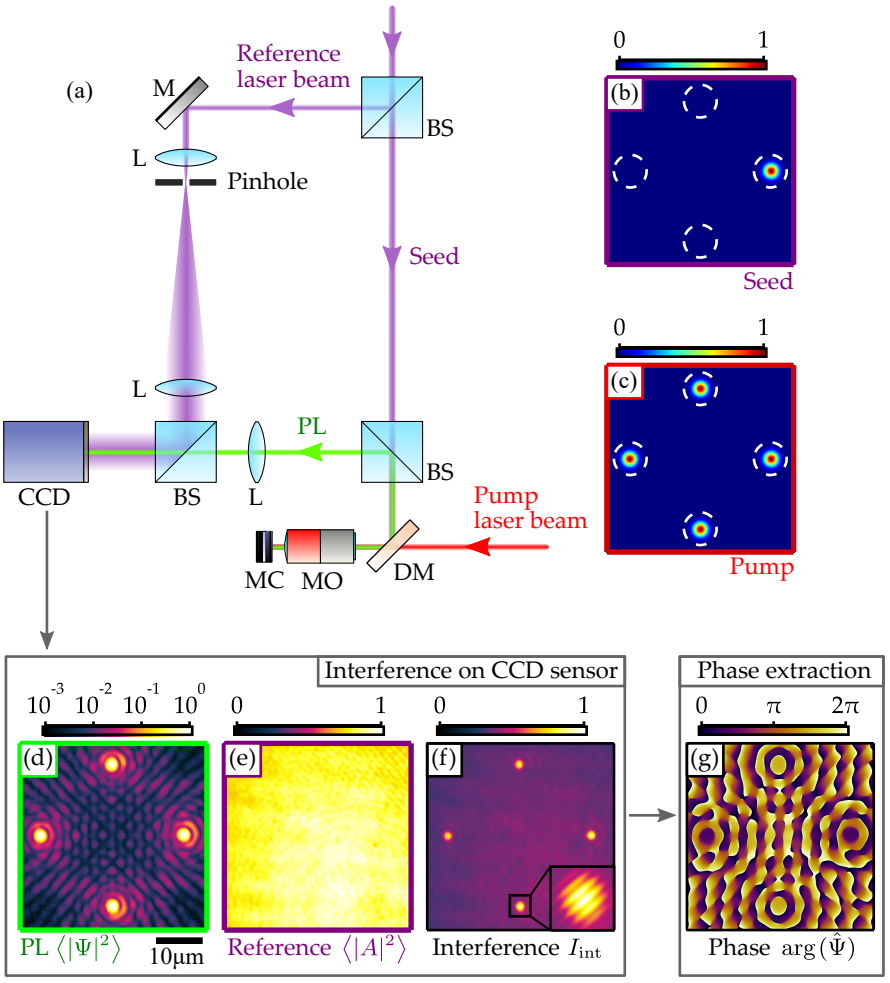

FIGURE 4.9: **Phase measurements in networks of polariton condensate.** (a) Schematic of the homodyne interferometer containing a resonant seed laser injected onto one non-resonantly pumped polariton condensate. Part of the resonant seed laser is used as a reference beam in a Mach-Zehnder interferometer configuration. Illustrations of the real space laser profiles of (b) resonant seed and (c) non-resonant pump exciting four polariton condensates. Recorded (d) real space photoluminescence $\langle|\Psi|^2\rangle$and (e) reference beam profile $\langle|A|^2\rangle$. (f) Interferogram of condensate PL and reference beam. (g) Digitally extracted condensate phase distribution arg $(\hat{\Psi})$.

emission signal Ψ with a coherent reference wave A allows to encode phase information into a spatial amplitude modulation accessible to a recording image sensor. In this section we describe a homodyne interferometric technique to extract the phase distribution arg $[\Psi(\mathbf{x})]$ of a stationary network of coupled polariton condensates. The method and its application for phase extraction in polariton condensate lattices is published in Ref. [90].

The interferometer setup is schematically shown in Fig. 4.9(a). We combine the two cw lasers described in Section 4.3 to excite and manipulate the condensate network. Both laser beams are synchronously modulated using AOMs into square wave trains of ≈ 5 μs duration. While one of the lasers ($\lambda \approx 800$ nm) serves as a spatially modulated non-resonant pump laser exciting a network of polariton condensates [Laser

2 in Fig. 4.6], the second resonant laser ($\lambda \approx 857$ nm) is used as a low-power seed laser to lock the phase of one condensate in the network [Laser 3 in Fig. 4.6]. Example images of the two laser profiles for (resonant) seed and (non-resonant) pump are shown in Fig. 4.9(b) and Fig. 4.9(c), respectively. Here, we excite an array of 4 condensates in square geometry and inject a low-power resonant seed beam onto the rightmost condensate only. The focused laser spots of both seed and pump beam have a FWHM ≈ 2 µm at the cavity plane. The seed laser linewidth (≈ 100 kHz) is more than 5 orders of magnitude narrower than that of the polariton condensate system. It is important to note that the resonant seed laser locks the phase of one condensate only, while any formation of spatial coherence across the condensate array is a result of in-plane coupling (see Chapter 7).

As part of the detection setup illustrated in Fig. 4.9(a) we project the polariton real space PL $\langle|\Psi(\mathbf{x},t)|^2\rangle_t$ onto a CCD image sensor. A portion of the resonant seed laser is being split by a beam splitter and spatially filtered using a combination of a lens and a pinhole. An additional lens, which is positioned at the focal distance away from the pinhole, collimates this reference laser beam and projects a broad beam profile with nearly flat phase front $A(\mathbf{x},t)$ onto the CCD camera filling the whole image sensor. The recorded beam profile $\langle|A(\mathbf{x},t)|^2\rangle_t$ is shown in Fig. 4.9(e). We utilise a beam splitter to combine both signals (PL and reference laser) and record their interference pattern $I_{\text{int}}(\mathbf{x})$ as illustrated in Fig. 4.9(f). The interferogram can be written as

$$I_{\text{int}}(\mathbf{x}) = \left\langle|\Psi(\mathbf{x},t)|^2\right\rangle_t + \left\langle|A(\mathbf{x},t)|^2\right\rangle_t + e^{i\mathbf{k}_\parallel\mathbf{x}}\cdot\left\langle A(\mathbf{x},t)\Psi^*(\mathbf{x},t)\right\rangle_t + e^{-i\mathbf{k}_\parallel\mathbf{x}}\cdot\left\langle A^*(\mathbf{x},t)\Psi(\mathbf{x},t)\right\rangle_t . \tag{4.12}$$

Here, we have included an adjustable tilt $\exp(i\mathbf{k}_\parallel\mathbf{x})$ in the wavefront of the reference beam leading to interference fringes as shown in the inset of Fig. 4.9(f). This tilt enables (off-axis) Fourier-analysis as presented in Section 4.4.2, and makes it possible to digitally extract the mutual coherence function $\left\langle A(\mathbf{x},t)\Psi^*(\mathbf{x},t)\right\rangle_t$ between seed laser and condensate PL. Due to the narrow linewidth of the reference laser we can approximate its optical wave as single-frequency, i.e. $A(\mathbf{x},t) = A_0(\mathbf{x})\exp(-i\omega_0 t)$. The laser's frequency ω_0 is tuned to match the peak of the (non-driven) condensate's power spectral density. The mutual coherence function can then be written as

$$\begin{aligned}\left\langle A(\mathbf{x},t)\Psi^*(\mathbf{x},t)\right\rangle_t &= A_0(\mathbf{x})\lim_{T\to\infty}\frac{1}{2T}\int_{-T}^{T} e^{-i\omega_0 t}\Psi^*(\mathbf{x},t)\mathrm{d}t \\ &= A_0(\mathbf{x})\cdot\hat{\Psi}(\mathbf{x},\omega=\omega_0).\end{aligned} \tag{4.13}$$

Here, we have introduced the time-frequency Fourier-transformed order parameter $\hat{\Psi}(\mathbf{x},\omega)$. We note that $\hat{\Psi}(\mathbf{x},\omega_0)$ is a complex-valued function describing both, spatial distribution of magnitude $|\Psi|$ and phase $\arg(\Psi)$ of the corresponding polariton mode with energy $\hbar\omega_0$. Aberrations in the phasefront of the reference wave (typically low-order Zernike polynomials) are incorporated in $A_0(\mathbf{x})$ and can be corrected from the

result in Eq. 4.13 yielding the condensate phase distribution $\arg(\Psi(\mathbf{x},\omega_0))$. The digitally extracted phase map of the four-condensate array is shown in Fig. 4.9(g).

4.4.4 Measurement of spatial correlations in condensate arrays

Synchronisation phenomena in networks of interacting elements, such as lattices of polariton condensates, can be investigated by means of correlation measurements between pairs of lattice nodes. When studying coupled polariton condensates we assume that the macroscopic order parameter $\Psi(\mathbf{x},t)$ can effectively be written as a sum of individual condensate wavefunctions, i.e.

$$\Psi(\mathbf{x},t)=\sum_i \psi_i(\mathbf{x}-\mathbf{x}_i,t). \tag{4.14}$$

Here, $\psi_i(\mathbf{x},t)$ represents the wavefunction of the ith condensate node within the network. Because of the strongly localised density of each condensate node i at their spatial position $\mathbf{x}_i$, the macroscopic order parameter approximately writes as $\Psi(\mathbf{x}_i,t)\approx\psi_i(0,t)$. Determination of the complex degree of coherence $g(\mathbf{x}_i,\mathbf{x}_i)$, defined in Eq. 3.33, therefore, gives a measure for the synchronisation of two coupled condensate nodes located at $\mathbf{x}_i$ and $\mathbf{x}_j$. We further abbreviate the mutual intensity and complex coherence factor between two condensate nodes i and j as Γ_{ij} and g_{ij}, respectively. In terms of the complex-valued amplitudes ψ_i these correlation functions can then be written as

$$\Gamma_{ij}=\left\langle\psi_i^*(0,t)\psi_j(0,t)\right\rangle_t, \tag{4.15}$$

and

$$g_{ij}=\frac{\left\langle\psi_i^*(0,t)\psi_j(0,t)\right\rangle_t}{\sqrt{\left\langle|\psi_i(0,t)|^2\right\rangle_t\left\langle|\psi_j(0,t)|^2\right\rangle_t}}. \tag{4.16}$$

In this section we describe an experimental technique for determination of the complex coherence factor between any pair of nodes within networks of coupled polariton condensates. The method and its application in measurements of spatial coherence in lattices of polariton condensates has been published in Ref. [89].

We utilise a digitally controllable spatial filter for generation of reconfigurable apertures and spatial modulation of the polariton lattice emission. In particular, we selectively mask the real space polariton emission $\Psi(\mathbf{x},t)$ with an aperture $P(\mathbf{x})$ transmitting only the spatial emission centres of condensate nodes. The masked emission profile writes then as $\Psi'(\mathbf{x},t)=P(\mathbf{x})\Psi(\mathbf{x},t)$. We approximate the aperture function as the sum of point-like holes, i.e.

$$P(\mathbf{x})=A\sum_i \delta(\mathbf{x}-\mathbf{x}_i), \tag{4.17}$$

where A accounts for the finite size of each hole and the sum is performed over the condensate node locations $\mathbf{x}_i$ within the lattice. Then, taking into account Eq. 3.37 we

see that the reciprocal space intensity function $\hat{I}'(\mathbf{k})$ of the spatially masked emission is the superposition of partially-coherent point-like light sources,

$$\hat{I}'(\mathbf{k}) = A^2 \sum_{i,j} \Gamma_{ij} e^{i\mathbf{k}\mathbf{d}_{ij}}. \tag{4.18}$$

Here, we have introduced the in-plane spatial displacement $\mathbf{d}_{ij} = \mathbf{x}_i - \mathbf{x}_j$ between each pair $\{i, j\}$ of condensate nodes. Experimental investigation of the masked far field emission pattern in Eq. 4.18 gives access to information about the spatial correlations Γ_{ij} in arrays of coupled condensates. In particular, for a mask transmitting two condensate centres only, Eq. 4.18 reduces to the double-hole interference pattern,

$$\hat{I}'_{1+2}(\mathbf{k}) = \hat{I}_1(\mathbf{k}) + \hat{I}_2(\mathbf{k}) + 2\sqrt{\hat{I}_1(\mathbf{k})\hat{I}_2(\mathbf{k})}|g_{12}| \cos(\mathbf{k}\mathbf{d}_{12} + \theta_{12}). \tag{4.19}$$

The homogeneous intensity profile $\hat{I}'_{1,2}(\mathbf{k})$ of each masked condensate is taken into account in Eq. 4.19 and arises due to the finite physical aperture hole sizes in our experiment. Measurement of the masked emission profiles $\hat{I}_1(\mathbf{k})$, $\hat{I}_2(\mathbf{k})$ and $\hat{I}_{1+2}(\mathbf{k})$ using three different apertures allows extraction of coherence $|g_{12}|$ and phase difference $\theta_{12} = \arg(g_{12})$ between both condensate nodes by fitting of Eq. 4.19.

In our experiment we utilise a reflective SLM as the core element of the digitally controllable aperture. The optical design is illustrated in Fig. 4.10(a) and is similar to the space-domain lock-in amplifier system presented in Ref. [91]. Working principle of the interferometer is demonstrated with the example of a triangular lattice of coupled polariton condensates. Real space and reciprocal space condensate emission are shown in Fig. 4.10(b) and 4.10(c). The polariton PL is collected using a microscope objective and polarisation-filtered using a quarter waveplate and polariser. The system only transmits the same polarisation as the circular pump polarisation, and the polariser angle coincides with the SLM's optical axis. We project the real space condensate PL onto the SLM surface (magnification $M = 60$) and apply a digital phase-hologram that consists of circularly-masked blazed-phase gratings. Each circular mask coincides with the position of a condensate node within the polariton lattice. The diameter of each circular mask amounts for ≈ 200 μm, and corresponds to an effective diameter of ≈ 3 μm on the sample plane. Example phase-holograms for spatial filtering of condensate node 1, condensate node 2, and condensate nodes $1 + 2$ are shown in Figs. 4.10(d-f).

An iris, which is located at the back focal plane of the collecting lens (L1), transmits only the modulated first diffraction order and blocks any reflected (unmodulated) light. Importantly, this means that any emission not being projected onto one of the circular masks displayed in Figs. 4.10(d-f) is blocked by the iris. By using two additional lenses (L2,L3) we project the masked far field patterns $\hat{I}'_1$, $\hat{I}'_2$ and $\hat{I}'_{1+2}$ onto a recording CCD camera as displayed in Figs. 4.10(g-i). The formation of interference fringes in Fig. 4.10(i) is a result of the mutual coherence between both condensate

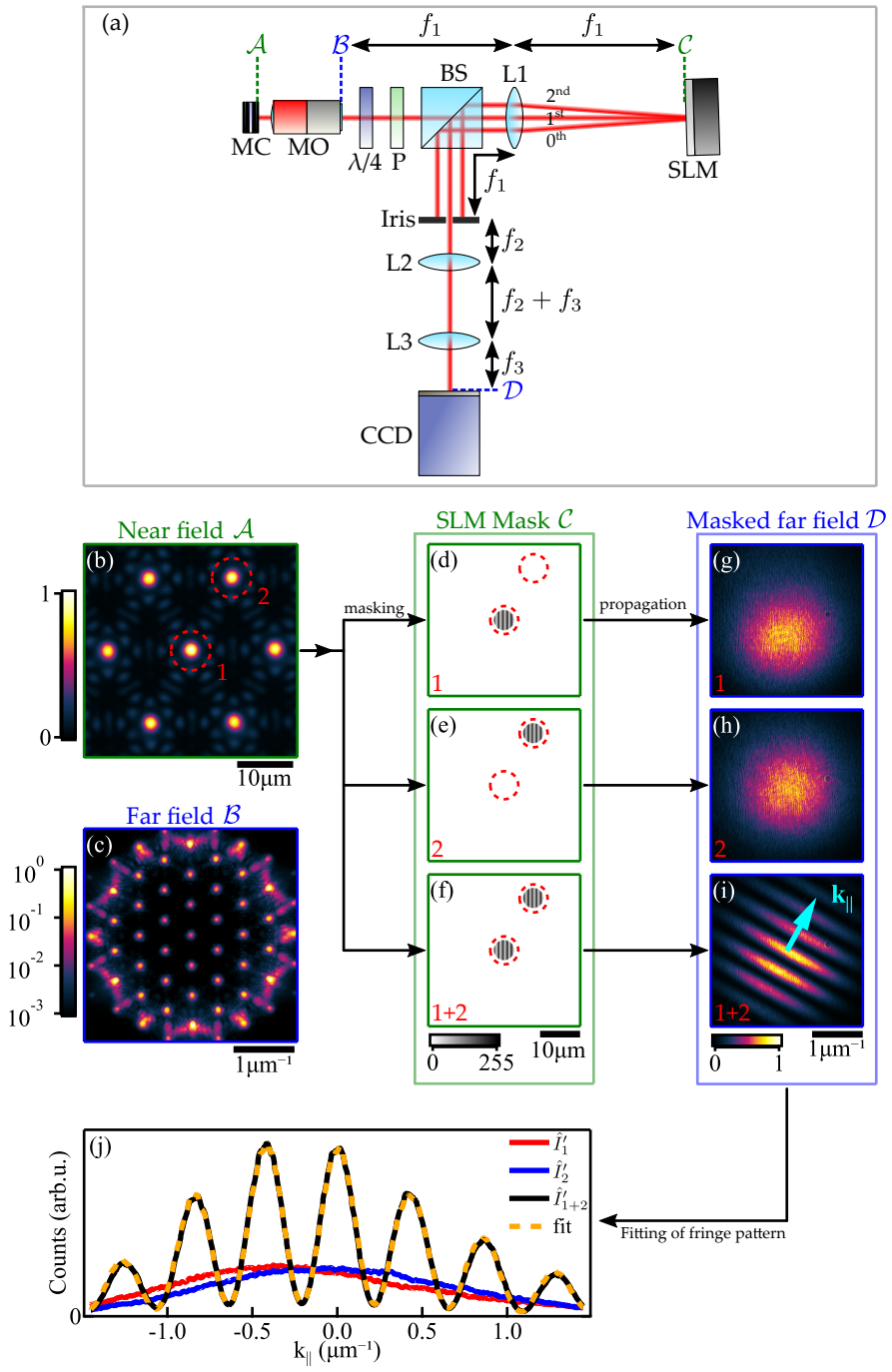

FIGURE 4.10: **Spatial coherence measurements in lattices of polariton condensates.** (a) Schematic of the optical setup for measurements of mutual coherence. (b) Near field and (c) far field profile of a triangular lattice of polariton condensates. (d-f) Three different apertures for filtering of the real space PL of either one or two condensate centres. (g-i) The far field emission patterns after filtering with masks shown in (d-f). (j) The extracted far field intensity profiles $\hat{I}'_1$, $\hat{I}'_2$ and $\hat{I}'_{1+2}$ perpendicular to the interference fringe orientation displayed in (i). Fitting of the interference profile (dashed yellow) yields the complex coherence factor g_{12} between both condensates.

nodes 1 and 2. For each far field measurement $\hat{I}'_i(\mathbf{k})$ we extract a 1-D intensity profile $\hat{I}'_i(k_\parallel)$ along the direction vector $\mathbf{k}_\parallel$, which is defined as co-parallel to the displacement vector $\mathbf{d}_{12}$, i.e. $\mathbf{k}_\parallel \mathbf{d}_{12} = k_\parallel |\mathbf{d}_{12}|$. Fitting of Eq. 4.19 along the direction vector

$\mathbf{k}_{\parallel}$, and each of the extracted intensity profiles $\hat{I}'_1(k_{\parallel})$, $\hat{I}'_2(k_{\parallel})$ and $\hat{I}'_{1+2}(k_{\parallel})$ are shown in Fig. 4.10(j). In this example the fitting yields a coherence $|g_{12}| = 0.86$ and phase difference $\arg(g_{12}) = -0.12$ rad between the two condensate nodes. Scanning of all pairs of condensate nodes i, j within the lattice allows to extract the full coherence map g_{ij} and to characterise the system's spatial coherence properties.

Chapter 5

Delay-Coupled Polariton Condensates

When the intrinsic time scales appearing in a system of coupled elements, such as the oscillation period of coupled pendulums, is much longer than the inter-element signal propagation time, the system is well described as instantaneously coupled. Examples of dynamical systems with vanishing coupling delay range from mechanical systems such as Huygen's clock synchronisation [48], to macroscopic quantum systems such as evanescently coupled polariton condensates [27]. On the other hand, when signal propagation times are comparable or longer than the oscillators intrinsic time scales, the system is subject to time-delayed interactions. The presence of time-delay in coupled dynamical systems is an ubiquitous phenomenon appearing in nature, technological applications, and socio-economic systems. It largely affects the spread of diseases in pandemics, influences traffic flow, dictates the neurological function of brains, defines the population dynamics of biological species in predator-prey systems, and determines the stability of lasers [92]. As previously described in Section 2.4, the appearance of time-delay in-between coupled elements greatly increases their dynamical complexity, and gives rise to dynamical effects such as phase-flip bifurcations [58] and both stabilisation and destabilisation of periodic orbits [2].

In this Chapter the coupling and synchronisation phenomena of spatially separated ballistically expanding polariton condensates is investigated. It is shown that the system can adequately be described by a delay-coupled oscillator model. By controlling the coupling time-delay (separation distance) between two condensates we observe phase-flip transitions and switching between fixed point and periodic orbit solutions. The results have been published in References [78] and [89]. In the following, we begin by summarising the experimental methods and introducing the characteristics of a single ballistically expanding condensate.

5.1 Experimental methods

The experimental techniques for excitation and detection of one or two polariton condensates with controllable spatial separation distance are described in Section 4.3 and Section 4.4 of this thesis. Unless otherwise stated, results presented in this Chapter are acquired using non-resonant cw excitation. The sample in use is a GaAs microcavity, which is described in Section 4.3, and operated at a negative (photonic) detuning ($\Delta \approx -5.5$ meV). The excitation laser is focused onto the sample using a $(0.4\text{NA}, 20x)$ microscope objective lens yielding laser spot sizes of approximately 2 μm FWHM.

5.2 Ballistically expanding condensates

It is known that the use of positive (excitonic) detuning and large-size laser excitation spots (FWHM $\gtrsim$ 30 μm) generally favours polariton ground state condensation [15]. On the other hand, operation at a negative (photonic) detuning and with a tightly-focused excitation laser spot was shown to facilitate non-ground state condensation at finite in-plane momentum $|\mathbf{k}| > 0$ [73, 75]. The origin of this effect lies in the spatially inhomogeneous anti-trapping potential for polaritons introduced by the locally injected exciton reservoir [93, 94]. Using the notation introduced for the generalised GPE [Eq. 3.27] the repulsive potential $V(\mathbf{x})$ felt by polaritons can be written as

$$V(\mathbf{x}) = g_R n(\mathbf{x}) + g|\Psi(\mathbf{x})|^2. \tag{5.1}$$

Condensed polaritons are generated with zero in-plane momentum at the pump spot location coinciding with the maximum of $V(\mathbf{x})$. Subsequent acceleration of particles away from the pump spot centre leads to radial 'ballistic expansion' of the polariton condensate with finite in-plane momentum $|\mathbf{k}| > 0$.

In Fig. 5.1 we illustrate the characteristics of the power-driven phase transition of a ballistically expanding polariton condensate. In particular, we show (a-c) the real space condensate emission, (d-f) the modulus of the system's complex coherence factor, (h-j) the condensate momentum space distribution, and (l-n) the spectrally resolved momentum space emission (dispersion) for varying excitation pump power. Below condensation threshold ($P < P_{\text{thr}}$) the complex coherence factor $g(\mathbf{x}, -\mathbf{x})$ depicted in Fig. 5.1(d) shows a narrow distribution with FWHM $\approx$ 1 μm indicating the absence of ODLRO. The incoherent emission is further evident in momentum space [Fig. 5.1(h)] and dispersion images [Fig. 5.1(l)], illustrating a broad particle density distribution both in reciprocal space and in energy. The condensate phase transition at $P = P_{\text{thr}}$ and the connected emergence of spatial and temporal coherence in the system are discernible by the formation of ODLRO [Fig. 5.1(e)], the narrowing of density distribution in momentum space [Fig. 5.1(i)], and the spectral linewidth narrowing [Fig. 5.1(m)]. We note

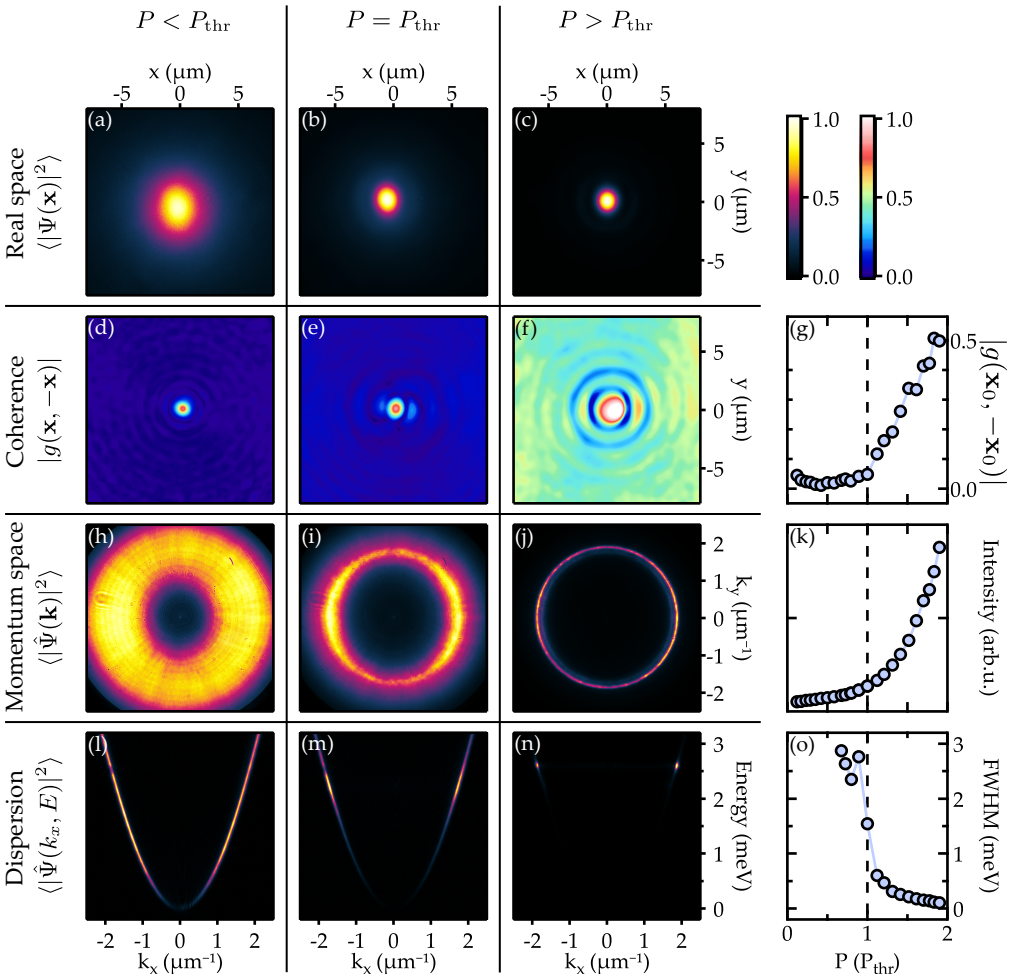

FIGURE 5.1: **Phase transition of a tightly-pumped polariton condensate.** (a-c) Real space particle density, (d-f) modulus of the complex coherence factor, (h-j) momentum space particle density, and (l-n) dispersion images for excitation powers (left column) below threshold, (middle column) at threshold, and (right column) above threshold. (g) Pump power dependency of the modulus of the complex coherence factor $g(\mathbf{x}_0,-\mathbf{x}_0)$ for $\mathbf{x}_0 = (0, 10\ \mu\mathrm{m})^T$. (k) Condensate emission intensity extracted by spatial integration of momentum space emission. (o) Power-dependence of the emission linewidth shown as the spectral FWHM. Small asymmetry in the condensate emission patterns arises from a small ellipticity of the pump laser beam profile.

that the emergence of spatial coherence (ODLRO) and a narrowing of density distribution in reciprocal space are inherently connected as described in Eq. 3.37. The macroscopic occupation of a single quantum state above condensation threshold $P > P_{\mathrm{thr}}$ is evident by the established long-range spatial coherence exceeding the pump spot size [Fig. 5.1(f)] and narrow particle density distributions in reciprocal space [Fig. 5.1(j)] and energy [Fig. 5.1(n)].

Characteristics of the power-driven condensate phase transition are further summarised in Figs. 5.1(g,k,o) showing the spatial coherence $|g(\mathbf{x}_0,-\mathbf{x}_0)|$ with $\mathbf{x}_0 = (0, 10\mu\mathrm{m})^{\mathrm{T}}$, the PL emission intensity, and the extracted spectral linewidth as a function of excitation pump power P. The phase transition at $P = P_{\mathrm{thr}}$ reveals a clear threshold behaviour

of spatial correlations $g(\mathbf{x}_0, -\mathbf{x}_0)$, an exponential increase of emission intensity, and a sharp narrowing of the emission linewidth.

In the presented case of a small excitation pump spot an approximate analytical description of the stationary condensate wave function $\Psi(\mathbf{x})\exp(-iEt/\hbar)$ outside the pump region can be obtained [93]. With increasing distance from the central pump spot location the effective repulsive potential $V(\mathbf{x})$ [Eq. 5.1] vanishes, and the stationary generalised GPE [Eq. 3.27] reduces to the linear Helmholtz equation, i.e.

$$\left[\frac{\hbar^2\nabla^2}{2m} + E + \frac{i\hbar\gamma}{2}\right]\Psi(\mathbf{x}) = 0. \tag{5.2}$$

The physically relevant solution to this equation is given by the 0th order Hankel function of the first kind, $H_0^{(1)}(\tilde{k}_c|\mathbf{x}|)$, and describes radially outgoing waves with complex-valued wave vector $\tilde{k}_c = \sqrt{2m(E + i\hbar\gamma/2)/\hbar^2}$. The asymptotic expansion of $H_0^{(1)}$ reveals the asymptotic form of the condensate wave function at large distances r,

$$\Psi(r \to \infty) \sim e^{ik_c r} \cdot \frac{e^{-\kappa r}}{\sqrt{|\mathbf{x}|}}. \tag{5.3}$$

Here, we have split the complex-valued wave vector $\tilde{k}_c$ into real- and imaginary parts, corresponding to the outflow wave vector $k_c \approx \sqrt{2mE/\hbar^2}$ and the spatial decay rate $\kappa = \gamma m/2\hbar k_c$, respectively.

We find good agreement between the form of an outgoing cylindrical wave and the experimentally measured condensate wave form of a tightly-pumped condensate summarised in Fig. 5.2. Here, we excite a ballistically expanding condensate using a nonresonant laser with approximately 2 µm (FWHM) spot size and pump power $P \approx 1.5P_{\text{thr}}$. In particular, we show the experimentally measured real space condensate density $|\Psi(\mathbf{x})|^2$ [Fig. 5.2(b)], the energy-resolved far field emission [Fig. 5.2(d)], the real space condensate phase map $\arg(\Psi(\mathbf{x}))$ [Fig. 5.2(e)], and the momentum space condensate density $|\hat{\Psi}(\mathbf{k})|^2$ [Fig. 5.2(g)]. The spectrally resolved far field PL depicted in Fig. 5.2(d) reveals single-mode condensation at elevated energy $E \approx 2.22$ meV above the LP ground state. Intersection of the LP dispersion paraboloid $E_{\text{LP}}(\mathbf{k})$ with this blue-shifted iso-energy plane E corresponds to the ring-shaped emission profile visible in momentum space [Fig. 5.2(g)] with radial outflow wave vector $k_c \approx 1.7$ µm^{-1}. The spatial decay of condensate density shown in Fig. 5.2 (c) is fitted with a cylindrical outgoing wave $H_0^{(1)}[(\tilde{k}_c r)]$ (red line) outside the pump spot region and yields a spatial decay rate $\kappa \approx 0.014$ µm^{-1}.

The ballistic expansion of the polariton condensate and its approximate wave form [Eq. 5.3] are particularly perceptible in the extracted radial phase profile $\arg(\Psi(r))$ as shown in Fig. 5.2(f). Outside the central pump region a constant linear phase gradient is clearly visible corresponding to a cylindrically expanding wave front with radial wave

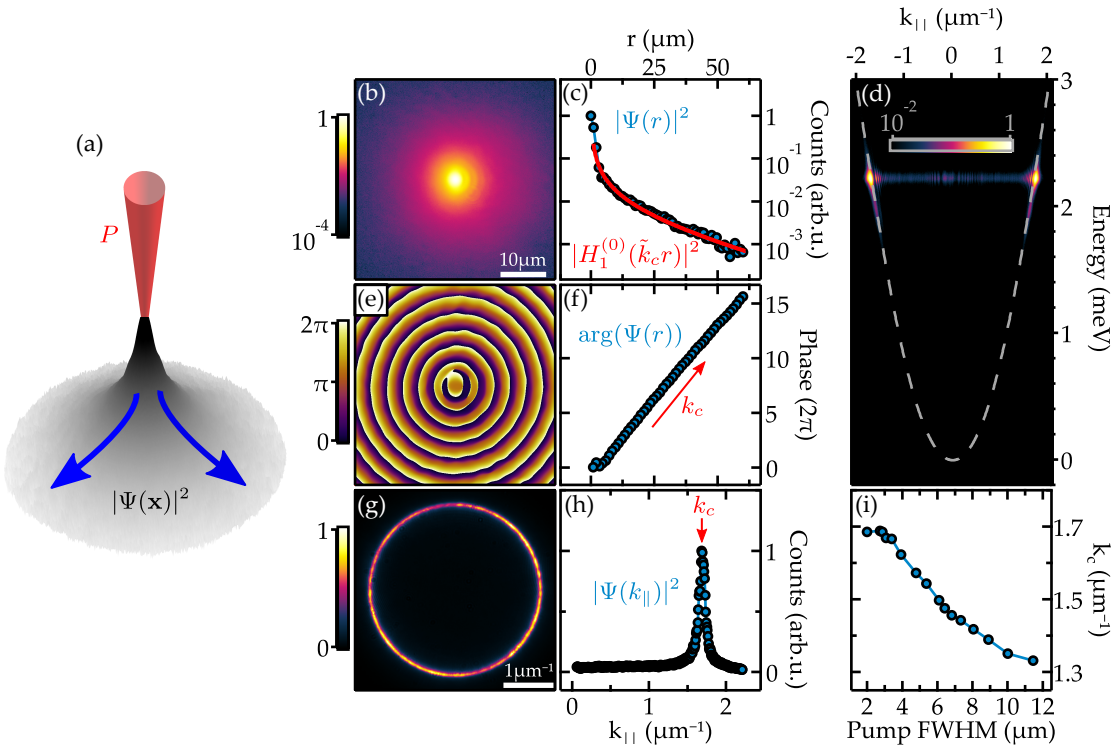

FIGURE 5.2: **Characteristics of a ballistically expanding polariton condensate.** (a) Schematic of the expanding condensate excited by a tightly-focused laser. (b) Measured real space PL and (c) extracted radial intensity profile. (d) Spectrally resolved momentum space PL showing single mode emission at energy $E \approx 2.22$ meV above the LP ground state. (e) Measured real space phase map and (f) extracted radial phase profile. (g) Measured condensate PL in momentum space and (h) extracted radial intensity profile showing density concentration at wave vector $k_c \approx 1.7$ μm^{-1}. (i) Dependence of the outflow wave vector k_c versus the FWHM of the pump laser spot. Results shown in (b-h) correspond to the smallest pump spot size ≈ 2 μm (FWHM).

vector k_c. The condensate gain center acts as a two-dimensional 'antenna' isotropically emitting matter-waves with well defined energy E and wavelength $\lambda = 2\pi/k_c$.

By applying a circular aperture with controllable size onto the SLM diffraction hologram in our optical excitation setup [Section 4.3] we effectively modify the NA of our focusing excitation lens. Via this additional modulation parameter we are able to characterise the dependency of the condensate radial expansion on the excitation pump spot size. The measured reduction of outflow wave vector k_c with increasing pump spot size is shown in Fig. 5.2(i). We note that, while the threshold pump power P_{thr} varies with the excitation laser spot size, in Fig. 5.2(i) the pump power P for each realisation was chosen to match $P = 1.5P_{\text{thr}}$. For large pump spot sizes we expect an asymptotically vanishing wave vector $k_c \to 0$ corresponding to ground state condensation in a spatially homogeneous potential landscape. At small pump spot sizes (≤ 3 μm FWHM) we notice a saturation of the outflow wave vector k_c, which is attributed to the finite diffusion length of the underlying exciton reservoir.

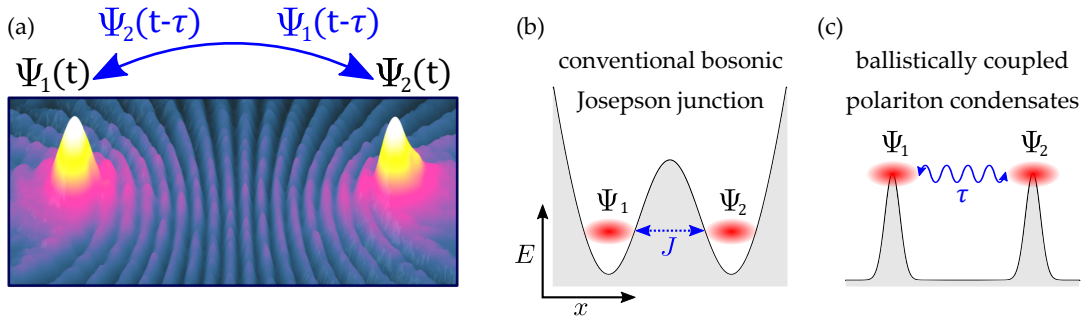

FIGURE 5.3: **Delay-coupled polariton condensates.** (a) Schematic showing the interference of two interfering ballistically expanding polariton condensates with separation distance $d \approx 37$ μm. Finite particle transfer time τ results in time-delayed coupling between condensates Ψ_1 and Ψ_2. Unlike in the case of (b) a conventional bosonic Josephson junction, the reported time-delayed coupling mechanism between (c) two ballistically coupled polariton condensates is not mediated by a tunnelling current J (blue dashed line) but by a radiative transfer of particles (blue wavy line). Figure adapted from Reference [78].

5.3 Ballistically coupled polariton condensates

Conventionally, coupled condensate structures consisting of ultra cold atoms [95], Cooper pairs [96], photons [97] or polaritons [27, 36] are realised in trapping potentials, and weakly coupled via tunneling currents (evanescent waves). Here, we detail on the inverse case, wherein two ballistically coupled polariton condensates act as freely expanding matter-wave sources (or antennas) experiencing dynamics reminiscent to macroscopic delay-coupled systems such as externally coupled semiconductor lasers [98]. Wave propagation from one polariton condensate centre to another results in a substantial phase accumulation, interpreted as a retardation of information flow between the condensates. A schematic of the time-delayed coupling scheme of two ballistically expanding polariton condensates is shown in Fig. 5.3(a). The differences between a bosonic Josephson junction and ballistically coupled polariton condensates are further highlighted in Figs. 5.3(b) and (c), where we show the conventional regime of coupled condensates separated by a potential barrier and described by a tunneling current J, and macroscopically coupled polariton condensates interacting via radiative particle transfer and subject to a finite propagation time τ.

The ballistic outflow of tightly-pumped polariton condensates facilitates particle exchange and (phase-)coupling of spatially separated condensation centers. This form of coupling has been investigated in previous studies [33, 41, 99, 100], and manifests itself in the formation of coherence across a multiplet of condensates. The synchronised state and established fixed phase differences θ_{ij} between each linked pair of condensates i and j was shown to depend on parameters such as the condensate separation distance d_{ij}, the outflow wave vector k_c, and sample disorder potential $V(\mathbf{x})$. The coupling mechanism has been described with parameters describing instantaneous coupling in the form of real-valued Josephson coupling [99], imaginary-valued gain-dissipative

coupling [101], complex-valued coupling [43] or qualitatively as a parameter that maximizes the particle number [41, 100] in a system that is driven by bosonic stimulation.

In the following, we present an in-depth study on the ballistic coupling and dynamics of tightly-pumped polariton condensates. We address in detail the system's spectral properties, the formation of synchronised and desynchronised (periodic) states, and the coherence of two condensates. We show that all features are best reproduced by coupled-mode equations with time-delayed interaction with strong similarity to the Lang-Kobayahsi equation [102, 103].

5.3.1 Synchronisation and interference of ballistic condensates

We investigate a system of two tightly-pumped polariton condensates with pump centers located at $\mathbf{x}_1$ and $\mathbf{x}_2$, and assume, that the presence of a second spatially displaced condensate node does not significantly alter the wave form of a ballistically expanding condensate [Eq. 5.3]. A synchronised state of the two matter-wave antennas is described by a common frequency $\omega = E/\hbar$ and a fixed phase difference $\theta_{12} = \text{const}$ between the two condensation centres. For such a state, one can express the total condensate wave function $\Psi(\mathbf{x}, t)$ as the sum of two terms,

$$\Psi(\mathbf{x}, t) = \psi_1(\mathbf{x})e^{-i\omega t} + e^{i\theta_{12}}\psi_2(\mathbf{x})e^{-i\omega t}, \tag{5.4}$$

where ψ_1 and ψ_2 represent the cylindrically expanding wave forms of a ballistic polariton condensate centred at their respective locations $\mathbf{x}_1$ and $\mathbf{x}_2$. For a symmetric system, $\psi_2(\mathbf{x}) = \psi_1(\mathbf{x} - \mathbf{d}_{12})$ with displacement vector $\mathbf{d}_{12} = \mathbf{x}_2 - \mathbf{x}_1$, and the stationary condensate densities in real and momentum space can be expressed as

$$|\Psi(\mathbf{x})|^2 = |\psi_1(\mathbf{x}) + e^{i\theta_{12}}\psi_1(\mathbf{x} - \mathbf{d}_{12})|^2, \tag{5.5a}$$

$$|\hat{\Psi}(\mathbf{k})|^2 = 2|\hat{\psi}_1(\mathbf{k})|^2 \left[1 + \cos\left(\mathbf{k}\mathbf{d}_{12} - \theta_{12}\right)\right], \tag{5.5b}$$

where $|\hat{\psi}_1(\mathbf{k})|^2$ denotes the ring-shaped momentum space density of a ballistic condensate [see Fig. 5.2(g)]. A synchronised state of the condensate nodes is described by the presence of interference fringes in both real space [Eq. 5.5a] and momentum space [Eq. 5.5b] as a result of stable counter-propagating polariton currents originating from the condensation centres. It is further apparent that the position of interference fringes in real and momentum space depends on the phase difference θ_{12}. In particular, a bright (dark) interference fringe at centre of symmetry, i.e. $\mathbf{x} = (\mathbf{x}_1 + \mathbf{x}_2)/2$ or $\mathbf{k} = 0$, occurs due to constructive (destructive) interference for an in-phase (anti-phase) synchronised system. Such states with in-phase ($\theta_{12} = 0$) or anti-phase ($\theta_{12} = \pi$) synchronisation can equivalently be classified by even or odd parity of the condensate wave function $\Psi(\mathbf{x}, t)$ described in Eq. 5.4.

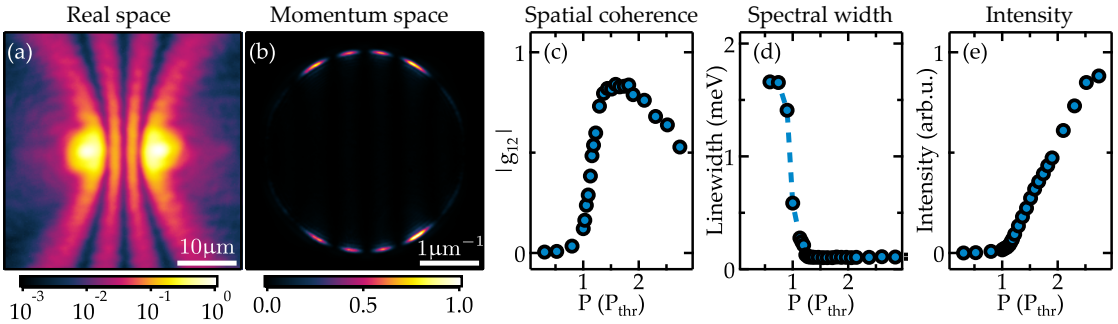

FIGURE 5.4: **Synchronisation of two ballistically coupled polariton condensates under cw laser excitation.** (a) Real space and (b) momentum space PL of two condensates separated by $d = 12$ μm. (c) Measured modulus of the complex coherence factor g_{12} between the two condensation centres versus laser pump power P. (d) Full width at half maximum of the measured power spectral density. (e) Spatially averaged PL intensity. Data shown in (a,b) correspond to pump power $P = 1.6P_{\text{thr}}$.

An experimental example of two ballistically expanding and coupled polariton condensates with separation distance $d = 12$ μm is pictured in Fig. 5.4. Anti-phase synchronisation of the two matter-wave antennas is evidenced by the formation of interference fringes with large visibility in real space [Fig. 5.4(a)] and momentum space [Fig. 5.4(b)]. It is important to note that the depicted near field and far field emission patterns represent time and ensemble averages over thousands of system realisations and, therefore, the phase difference $\theta_{12} = \pi$ is deterministically established.

The coherence between the two condensate nodes can be quantified by the modulus of their complex coherence factor $|g_{12}|$ as described in Eq. 4.16. In Fig. 5.4(c) we show the pump power-dependence of $|g_{12}|$ revealing absence of coherence below threshold ($P < P_{\text{thr}}$), a sharp increase of mutual coherence at condensation threshold $P = P_{\text{thr}}$, and a maximum of coherence $|g_{12}| = 0.84$ above threshold $P \approx 1.6P_{\text{thr}}$. The decrease of equal-time correlations expressed by $|g_{12}|$ for larger pump powers $P > 1.6P_{\text{thr}}$ arises due to the transition to multi-mode lasing and will be discussed in the following Sections. As expected and shown in Figs. 5.4(d) and (e) the phase transition is also characterised a sharp reduction in emission linewidth and an exponential increase in PL intensity.

We note, that while the separation distance $d = 12$ μm in Fig. 5.4 was chosen to yield a stationary state of two polariton condensates with $\theta_{12} = \pi$, a change in d can significantly alter the synchronisation state. In fact, we observe that opposite to the two-fold hybridisation of two evanescently coupled polariton condensates [27], the ballistically coupled system is characterised by a multitude of accessible modes of even and odd parity (i.e. 0 and π phase difference) that alternate continuously between opposite parity states with increasing separation distance d. For a range of separation distances only one resonant mode is present in the gain region of the system, wherein the polariton dyad is phase-locked, occupying a single energy level. Between the separation distances where only one mode is present, we observe the coexistence of two resonances with opposite parity resulting in non-stationary periodic states, i.e. $\theta_{12}(t) \neq$ const.

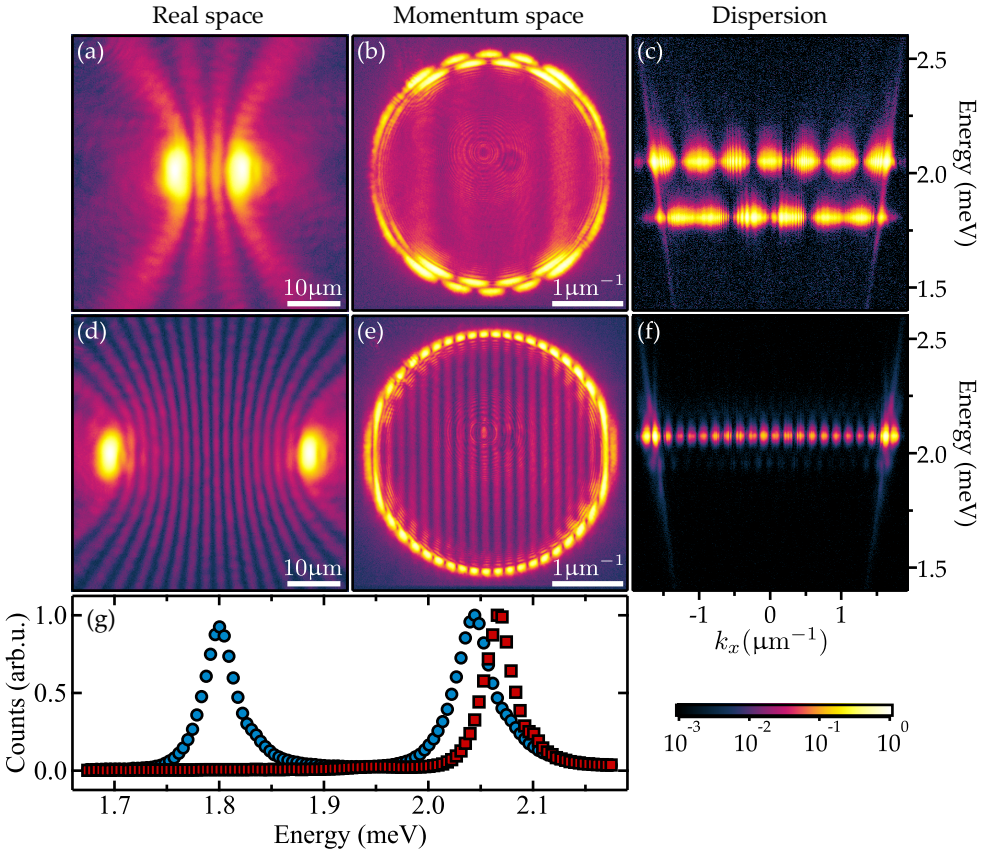

FIGURE 5.5: **Characteristics of two ballistically coupled polariton condensates.** (a,d) Real space, (b,e) momentum space, and (c,f) spectrally-resolved momentum space emission for two condensates with separation distances (a-c) $d = 12.7$ μm and (d-f) $d = 37.3$ μm. (g) Normalised power spectral densities shown as blue circles and red squares, respectively. Absolute values of the energy are given as a blue-shift with respect to the lower polariton ground state energy. Each condensate is excited by a non-resonant laser with power $P = 1.5P^{(1)}_{\text{thr}}$, where $P^{(1)}_{\text{thr}}$ is the threshold pump power of a single isolated condensate. Figure adapted from Reference [78].

Examples of the two regimes, stationary and non-stationary, are pictured in Fig. 5.5. In particular, Figs. 5.5(a,d) show real space PL, Figs. 5.5(b,e) show momentum space PL, and Figs. 5.5(c,f) show the spectrally resolved momentum space emission along the dyad symmetry axis $k_y = 0$ for the separation distances $d = 12.7$ μm and $d = 37.3$ μm, respectively. Each condensate node is pumped by a non-resonant laser spot with power $P = 1.5P^{(1)}_{\text{thr}}$, where $P^{(1)}_{\text{thr}}$ is the threshold pump power of a single isolated condensate. In the case of the non-stationary state ($d = 12.7$ μm), two lasing modes are clearly visible in momentum space [Fig. 5.5(b)] and dispersion [Fig. 5.5(c)]. Both of these modes have well defined but opposite parity to the other. We note that as long as the two condensate nodes are pumped with equal power, we do not observe formation of any non-trivial phase configurations. The power spectral densities (PSDs) of single-mode and dual-mode regimes are compared in Fig. 5.5(g), revealing a general red-shift (reduction in energy) compared to the emission energy $E \approx 2.22$ meV of a single ballistic

condensates excited with the same pump power $P = 1.5P_{\text{thr}}^{(1)}$ [see Fig. 5.2(d)]. The origin of this red-shift is the reduced exciton reservoir population and interaction energy due to a lower condensation threshold for ballistically coupled polariton condensates (see Section 6.3.4).

5.3.2 Spectral characterisation

Deeper insight into the dynamics and synchronisation of two ballistically coupled polariton condensates is obtained by investigating the system's spectral features for continuously varying condensate node separation distance d. We record the spectrally-resolved far field emission (dispersion) for more than 400 sample points between $d = 5$ μm and $d = 55$ μm while keeping the excitation pump power per condensate node constant at $P = 1.5P_{\text{thr}}^{(1)}$. The extracted and normalised power spectral densities are illustrated in Fig. 5.6(a), and show that for each distance d the dominant PL signal is formed by either one or two lasing modes. We note that there also exist configurations with more than two detectable occupied energy levels, but with a relative spectral weight of the third peak always less than a few percent. In the following, we focus our analysis to the two brightest lasing modes for each configuration.

Spectral weights and extracted spectral blue-shift of the two brightest lasing modes for each condensate node separation distance d are illustrated in Figs. 5.6(b) and (c) using red dots and blue squares to distinguish even and odd parity modes, respectively. We find that the system follows and oscillatory behaviour between the two parity states, thus giving rise to continuous parity transitions of the condensate order parameter Ψ with increasing distance d. In other words, this means that the synchronisation state of the two ballistic condensates periodically alternates between stable in-phase ($\theta_{12} = 0$) and anti-phase ($\theta_{12} = \pi$) configurations, with non-stationary regimes ($\theta_{12}(t) \neq$ const) appearing in-between. Each period of these parity oscillations (starting and ending with a vanishing spectral weight) displays an 'energy branch' featuring a notable reduction in energy with increasing pump spot separation distance d. The spectral range of each energy branch, i.e. its measurable red-shift with increasing d, is decaying branch-to-branch, and can be linked to a decaying coupling strength between the two condensates with increasing distance. In the limit of large separation distances $d \to \infty$ the system emission energy coincides with that of uncoupled (isolated) condensates [black dashed horizontal line in Fig. 5.6(c)].

We note the strong similarity between the experimentally recorded spectral composition of two ballistically coupled polariton condensates for varying distance d shown in Fig. 5.6 and the presented spectra of two delay-coupled Kuramoto oscillators for

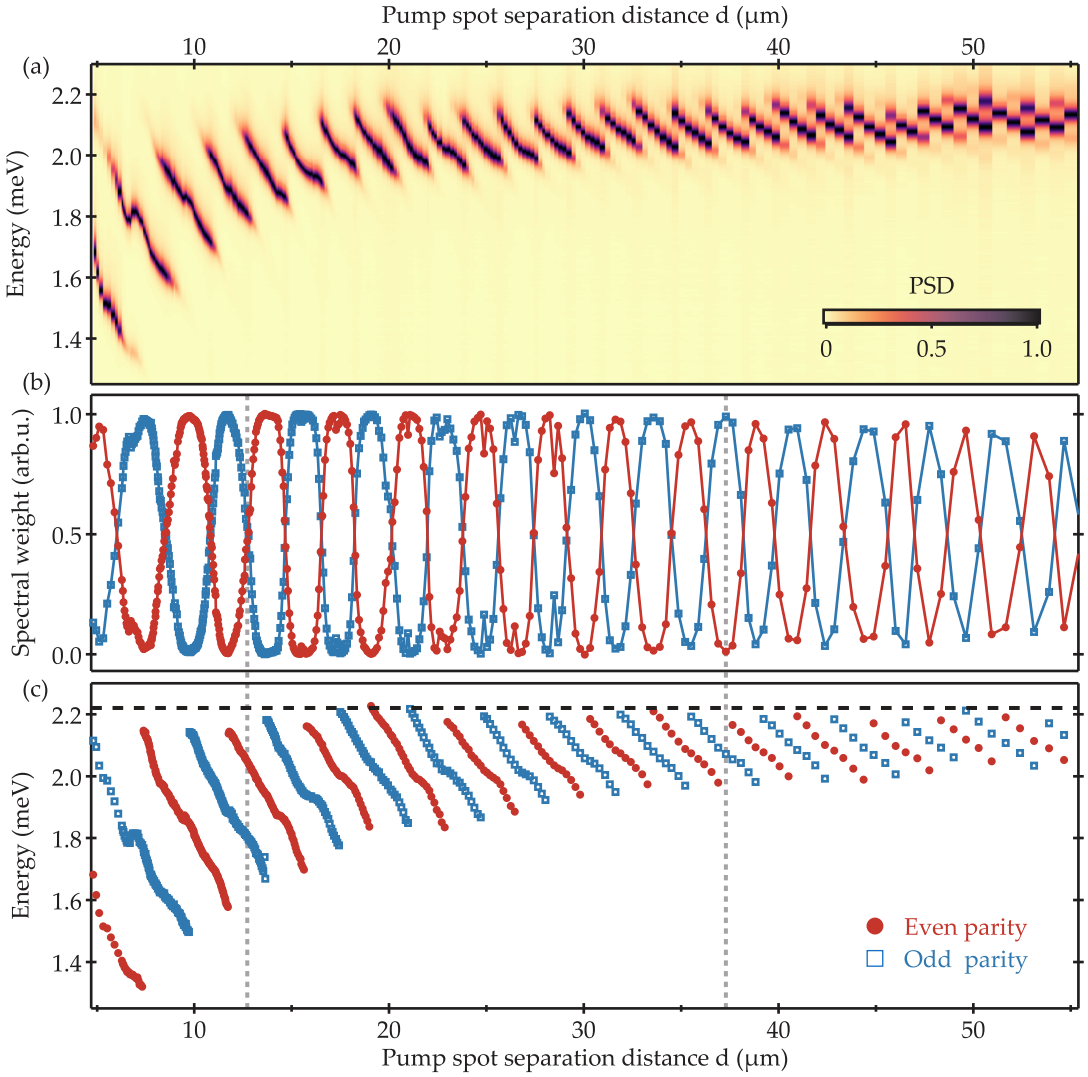

FIGURE 5.6: **Spectral characterisation of two ballistically coupled polariton condensates.** (a) Measured normalised power spectral densities (PSD) of two coupled polariton condensates with separation distance d. The non-resonant excitation pump power P for each condensate node is fixed at $P = 1.5P_{\text{thr}}^{(1)}$, where $P_{\text{thr}}^{(1)}$ is the threshold pump power of a single isolated condensate. (b) Spectral weights and (c) blue-shift of the two most dominant even (red dots) and odd (blue squares) parity modes for each separation distance d. The emission energy $E \approx 2.22$ meV of a single ballistic condensates pumped with the same pump power $P = 1.5P_{\text{thr}}^{(1)}$ is illustrated as a black dashed horizontal line in (c). Vertical grey dashed lines indicate to the two configurations presented in Fig. 5.5. Figure adapted from Reference [78].

varying time delay τ presented in Fig. 2.3(d). Moreover, it has been shown that phase-flip transitions in non-linear oscillatory systems, accompanied with changes in oscillation frequency to another mode are universal characteristics of time-delayed coupling [56, 104]. Such dynamics are often linked to non-linear electronic circuits [104] and coupled semiconductor lasers [98], but have also been demonstrated experimentally for other types of time-delayed coupled systems such as living organisms [105], chemical oscillators [106] and candle-flame oscillators [107].

5.3.3 Periodic population transfer

Non-stationary states of the coupled two condensate system [as shown in Figs. 5.5(a-c)] involve periodic transfer of condensate population due to the admixture of even and odd parity states. Such coherent population oscillations between two polariton condensates have been reported for evanescently coupled polariton condensates forming a bosonic Josephson junction [26, 27] as schematically illustrated in Fig. 5.3(b). While the oscillations in these trapped systems have been realised under pulsed and asymmetric pumping, the oscillations for ballistically coupled condensates are realised under symmetric cw excitation, i.e. the oscillations emerge spontaneously.

In the following, we consider the case of a coherent polariton dyad with two co-existing lasing modes of equal amplitude but opposite parity. The complex amplitudes $\psi_1(t)$ and $\psi_2(t)$ of the two coupled condensates can then be expressed as

$$\psi_1(t) = \psi_0 \left(e^{-i\omega_e t} + e^{-i\omega_o t} \right) /2, \tag{5.6a}$$

$$\psi_2(t) = \psi_0 \left(e^{-i\omega_e t} - e^{-i\omega_o t} \right) /2, \tag{5.6b}$$

where we have introduced the time-independent complex amplitude ψ_0, and the oscillation frequencies of even and odd parity modes as ω_e and ω_o. While the total population is conserved, $|\psi_1(t)|^2 + |\psi_2(t)|^2 = |\psi_0|^2$, the finite frequency splitting $\Delta = |\omega_e - \omega_o|$ leads to the periodic population oscillations

$$|\psi_1(t)|^2 = |\psi_0|^2 \cos^2(\Delta t/2), \tag{5.7a}$$

$$|\psi_2(t)|^2 = |\psi_0|^2 \sin^2(\Delta t/2). \tag{5.7b}$$

For the dual-mode states in the investigated range of condensate separation distances from $d = 5$ µm to $d = 55$ µm [see Fig. 5.6] we measure an energy splitting in the range of $\hbar\Delta = 80$ µeV to $\hbar\Delta = 450$ µeV. The expected oscillation periods $T \approx 10$ ps $- 50$ ps are well below the $\sim$ µs minimum exposure times of CCD or CMOS sensors, and thus cannot be directly resolved.

However, indirect assessment of the coherent population oscillations between two coupled polariton condensates can be conducted by measuring first-order temporal correlations between the condensate nodes [for experimental methods see Section 4.4.2]. In particular, the complex degree of coherence [see Eq. 3.33] between two condensate nodes with complex amplitudes ψ_i and ψ_j is written as

$$g_{ij}(\eta) = \frac{\left\langle \psi_i^*(t)\psi_j(t+\eta) \right\rangle_t}{\sqrt{\left\langle |\psi_i|^2 \right\rangle_t \left\langle |\psi_j|^2 \right\rangle_t}}. \tag{5.8}$$

The complex degree of coherence $g_{ij}(\eta)$ is a Hermitian matrix, and describes auto- and cross-correlations in the two-condensate system for $i = j$ and $i \neq j$, respectively.

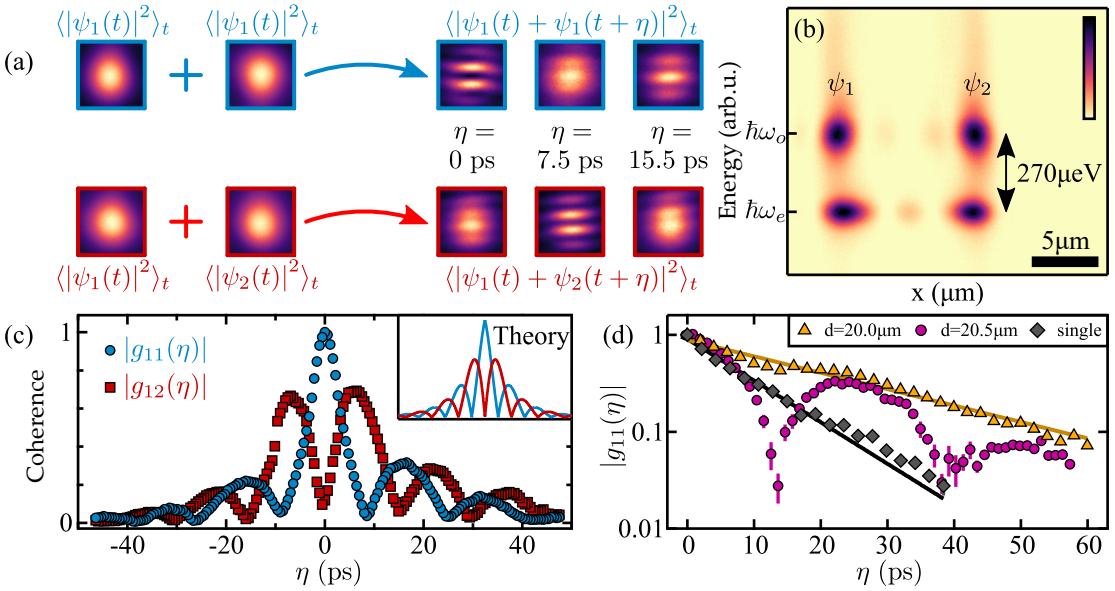

FIGURE 5.7: **Periodic (two-colour) states of two ballistically coupled polariton condensates.** (a) Interferograms of the real space PL of one condensate ψ_1 with a delayed version of itself, or with a delayed version of the second spatially displaced condensate ψ_2. (b) Spectrally resolved real space emission of the two condensate system. (c) Modulus of the complex degree of coherence $|g_{11}(\eta)|$ and $|g_{12}(\eta)|$ for vaying time offset. Inset shows the expected coherence oscillations multiplied with an exponential decaying envelope. The two condensates shown in (a-c) are separated by a distance $d = 10.3$μm. (d) Measured modulus of the complex degree of self-coherence $|g_{11}(\eta)|$ in a two condensate system with distance $d = 20.0$ μm and $d = 20.5$μm, and for a single (isolated) condensate. Solid lines represent exponential fits with $1/e$ decay times of $\tau_c = 25.5$ ps and $\tau_c = 10.2$ ps. Figure adapted from Reference [78].

The periodic population oscillations of the dual-mode system, which are described in Eqs. 5.6 and Eqs. 5.7, are innately linked to the periodic coherence relations of diagonal and off-diagonal elements

$$|g_{11,22}(\eta)| = |\cos(\Delta\eta/2)|, \tag{5.9a}$$

$$|g_{12,21}(\eta)| = |\sin(\Delta\eta/2)|. \tag{5.9b}$$

In our experiment we determine the behaviour of the complex degree of coherence $g_{ij}(\eta)$ in a polariton dyad with distance $d = 10.3$ μm via interferometric measurements as summarised in Fig. 5.7(a) for diagonal elements (top row) and off-diagonal elements (bottom row). Energy-resolved real space PL along the axis of the dyad reveals occupation of an even and odd parity mode with energy splitting $\hbar\Delta = 270$ μeV [see Fig. 5.7(b)]. The experimentally extracted values of mutual coherence $|g_{12}(\eta)|$ and self-coherence $|g_{11}(\eta)|$ are shown in Fig. 5.7(c), and demonstrate periodic disappearance and revival of coherence with period $T = 15.3$ ps, which is consistent with the observed energy splitting. In good agreement with the expected behaviour [Eqs. 5.9] there is a strong equal-time auto-correlation signal $g_{11}(0) \approx 1$, and a vanishing cross-correlation signal $g_{12}(0) \approx 0$ due to the antisymmetric temporal population beatings

in $|\psi_1(t)|^2$ and $|\psi_1(t)|^2$. In the inset of Fig. 5.7(c) we illustrate the calculated coherence oscillations [Eqs. 5.9] multiplied with an exponential decay accounting for the system's finite coherence time.

A comparison of the temporal decay of coherence for a single polariton condensate, and both single-mode and dual-mode polariton dyad configurations is depicted in Fig. 5.7(d). Here, we show the measured decay of self-coherence $|g_{11}(\eta)|$ for a stationary (single-mode) dyad with separation distance $d = 20$ μm, an oscillatory (dual-mode) dyad with distance $d = 20.5$ μm, as well as the decay of self-coherence of a single ballistically expanding polariton condensate. All configurations are pumped equally with power $P = 1.7P_{\text{thr}}^{(1)}$ per condensate node. Interestingly, the ballistic coupling of two condensates results in an enhanced coherence time: In case of the single-mode polariton dyad and the isolated condensate the coherence time τ_c is extracted from exponential fits yielding $\tau_c = 25.5$ ps and $\tau_c = 10.2$ ps, respectively. The origin of these enhanced coherence properties is the previously mentioned reduced exciton reservoir population for ballistically coupled polariton condensates, and is further discussed in Section 6.3.4.

5.3.4 Time-resolved synchronisation

The time-resolved formation of spatial coherence in polariton condensates under non-resonant pulsed laser excitation has been investigated for both single-[108, 109, 110] and two-condensate systems [99, 100]. However, in the latter case, a detailed description of the synchronisation process between two condensates in terms of their complex coherence factor has not been reported. Here, we explicitly address the (time-resolved) build-up of the complex coherence factor,

$$g_{ij}(t) = \frac{\langle \psi_i^*(t)\psi_j(t)\rangle}{\sqrt{\langle|\psi_i|^2\rangle \langle|\psi_j|^2\rangle}}, \tag{5.10}$$

for two ballistically coupled condensates with complex amplitudes ψ_i and ψ_j.

The experimentally recorded time-averaged real space emission profile of a polariton dyad under sub-picosecond pulsed laser excitation with separation distance $d = 8$ μm and pump power $P = 1.2P_{\text{thr}}$ is shown in Fig. 5.8(a). The bright interference peak located at the geometrical centre of the two-condensate system $(x, y = 0)$ indicates in-phase synchronisation of the two condensate nodes. The synchronisation state is confirmed by the Young's double hole far field interference pattern as shown in Fig. 5.8(b) [methods detailed in Section 4.4.4], and reveals a large (time-averaged) complex coherence factor $|g_{12}| \approx 0.94$. By projecting the far field emission pattern onto the entrance slit of a streak camera with time resolution $\Delta t = 2$ ps we can record the time-resolved and ensemble-averaged emission of each individual condensate node and their mutual interference as shown in Figs. 5.8(c-e). The origin of the time axis $t = 0$ is set by

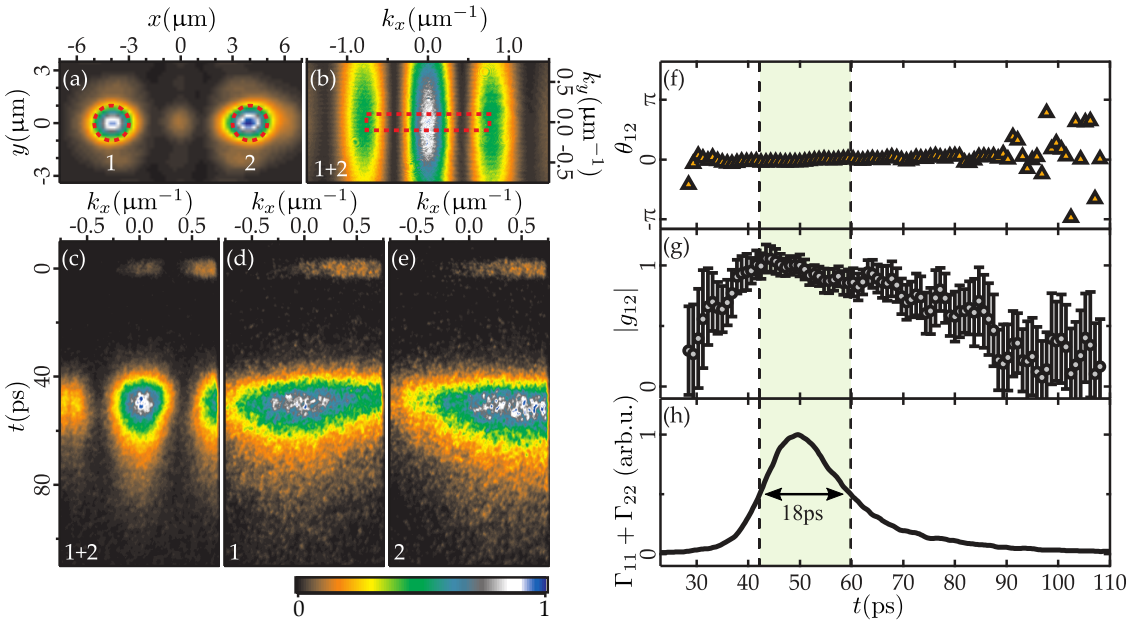

FIGURE 5.8: **Time-resolved synchronisation of two ballistically coupled polariton condensates with separation distance $d = 8$ μm.** (a) Measured real space PL. (b) Recorded far field interference when spatially filtering the emission of both condensate centres as marked with red dashed circles in (a). (c-e) Time-resolved and normalised far field PL for both condensates interfering (1 + 2) and individually (1, 2), recorded by projecting the PL onto the entrance slit of a streak camera (red-dashed rectangle in (b)). Extracted time-dependencies of phase difference $\theta_{12}(t)$, the modulus of the complex degree of coherence $g_{12}(t)$, and the total emission signal $\Gamma_{11}(t) + \Gamma_{22}(t)$ of both condensate nodes are shown in (f-h). The origin for the time axis in (f-h) is defined by the laser arrival time. Light green shaded area in (f-g) marks the full width at half maximum of the emission signal. Figure adapted from Reference [89].

the excitation laser pulse arrival time. The extracted time-resolved dynamics of the complex degree of coherence $g_{12}(t)$ and the total condensate occupation $\Gamma_{11}(t) + \Gamma_{22}(t)$ with $\Gamma_{ii}(t) = |\psi_i(t)|^2$ are illustrated in Figs. 5.8(f-h). Interestingly, while the measured condensate population $\Gamma_{11}(t) + \Gamma_{22}(t)$ reveals a peak signal ≈ 50 ps after the excitation pulse, the mutual coherence $g_{12}(t)$ reaches complete synchronisation $|g_{12}(t)| = 1$ at shorter time $t \approx 41$ ps, which is still during the condensate growth time. A difference in dynamics between condensate population and spatial correlations is also noticeable in the subsequent temporal decay of the condensate. Exponential fits yield $1/e$ decay times of ≈ 80 ps and ≈ 13 ps for the coherence factor $|g_{12}(t)|$ and the condensate population $\Gamma_{11}(t) + \Gamma_{22}(t)$, respectively. Differences in growth and decay dynamics between condensate population and coherence in single-condensate systems have previously been observed in Ref. [108] and Ref. [109].

5.3.5 Spatial coherence

Due to the spatial decay of ballistically expanding condensates [Eq. 5.3] it is expected that the coupling strength between spatially separated condensates is decaying with

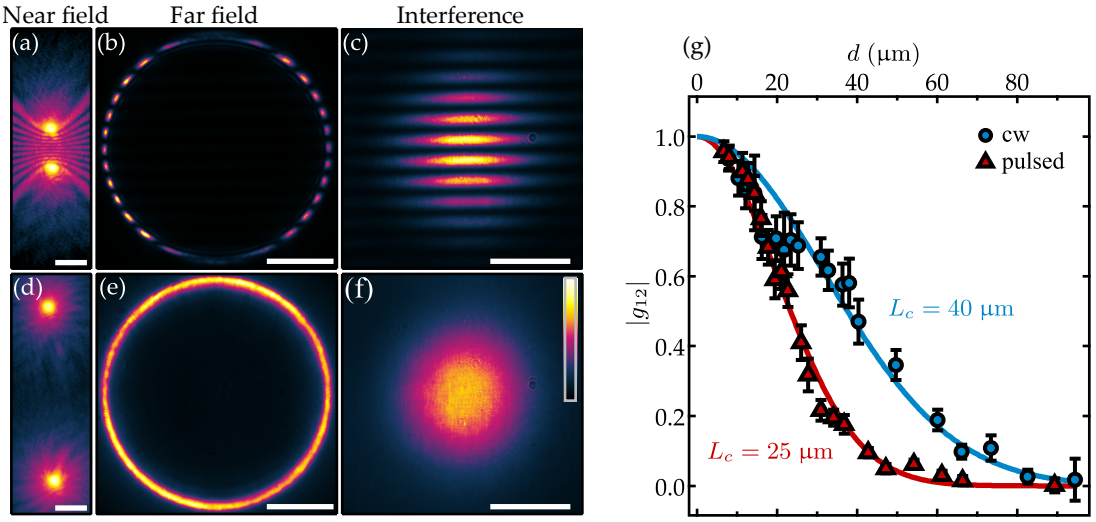

FIGURE 5.9: **Mutual coherence of two ballistically coupled polariton condensates.** Measured (a,d) real space and (b,e) momentum space PL of two condensates under cw laser excitation and with separation distances $d \approx 25$ μm and $d \approx 110$ μm. (c,f) Corresponding Young's double hole interference patterns, realised by spatially filtering the central ≈ 2 μm FWHM of each condensate node in real space. (g) Dependence of the extracted mutual coherence factor g_{12} on the condensate separation distance d for cw excitation (blue circles) and pulsed excitation (red triangles). Solid lines represent Gaussian curve fits to the experimental data. Data shown in (g) are extracted at constant pump power, which is set at $P = 1.6\ P_{\mathrm{thr,cw}}^{(12\mu\mathrm{m})}$ and $P = 1.2\ P_{\mathrm{thr,p}}^{(12.7\mu\mathrm{m})}$ for cw and pulsed excitation, respectively. Figure adapted from Reference [89].

increasing distance d. From our stability analysis of two coupled phase oscillators described in Section 2.3 and illustrated in Fig. 2.2(d) we therefore expect reduced coherence properties between two condensates with large distance d, because relaxation of perturbations to the synchronised state is less efficient. In the limit of $d \to \infty$ the uncoupled polariton condensates are incoherent with $g_{12} = 0$.

In our experimental study of mutual coherence across a ballistic polariton dyad for varying separation distance d we focus on stationary configurations with single-mode condensation only. For all distances d we set the total non-resonant cw pump power to the same value $P = 1.6 P_{\mathrm{thr}}^{(12\mu\mathrm{m})}$, where $P_{\mathrm{thr}}^{(12\mu\mathrm{m})}$ is the threshold pump power of a dyad with separation distance $d = 12$ μm [see Fig. 5.4]. Recorded real space and momentum space PL of two configurations with $d \approx 25$ μm and $d \approx 110$ μm are shown in Figs. 5.9(a,d) and Figs. 5.9(b,e), respectively. The presence of mutual coherence between the two ballistically expanding polariton condensates for the smaller distance is visible in the formation of interference fringes in both real and momentum space [Figs. 5.9(a,b)]. On the other hand, the absence of interference fringes in the emission patterns of the large ballistic polariton dyad with $d \approx 110$ μm [Figs. 5.9(d,e)] indicates a desynchronised state. In fact, the far field radiation pattern shown in Fig. 5.9(e) is the incoherent superposition of two ring-like emission patterns originating from both polariton condensates. It is important to note that each of the uncoupled condensates in the large polariton dyad is still pumped above condensation threshold.

To determine the complex coherence factor g_{12} between the two condensates we measured the corresponding Young's double hole interference patterns [methods detailed in Section 4.4.4]. The far field interference of the two condensation centers for small ($d \approx 25$ μm) and large ($d \approx 110$ μm) distance are illustrated in Figs. 5.9(c) and (f), respectively. The extracted modulus of the complex coherence factor $|g_{12}|$ for single-mode polariton dyad configurations with varying separation distance d and under cw excitation are shown in Fig. 5.9(g) using blue circles. We quantify the length over which synchronisation of the two-condensate system is possible by the effective coherence length L_c,

$$L_c = \int_0^\infty |g(x)| \mathrm{d}x, \tag{5.11}$$

where $|g(x)|$ is the extracted mutual coherence of a dyad with separation distance x. A Gaussian curve [blue solid line in Fig. 5.9(g)] is fitted to the experimental data yielding an effective coherence length $L_c = 40$ μm. We note that an increase in coherence length of two ballistically expanding polariton codensates is realisable through an increase of pump power, i.e. an increase of particle fluxes, and synchronisation of two condensates beyond 100 μm separation distance has been demonstrated [78].

In Fig. 5.9(g) we also show the measured time-integrated modulus of the complex coherence factor $|g_{12}|$ for two condensates under non-resonant sub-picosecond pulsed laser excitation. While both excitation schemes demonstrate similar coherence properties for small separation distances $d < 20$ μm, the measured coherence $|g_{12}|$ of the stationary system under cw excitation is enhanced for larger distances $d > 20$ μm as compared to the pulsed excitation scheme. A Gaussian curve fit [red solid line in Fig. 5.9(g)] yields a reduced effective coherence length $L_c = 25$ μm as opposed to cw excitation. For small separation distances $d < 20$ μm, i.e. short inter-condensate travel distances, the build-up of coherence $g_{12}(t)$ under pulsed excitation is fast enough as to efficiently synchronise the two-condensate system [see Section 5.3.4] and approximately reach the same coherence as in steady state operation. For larger distances, however, the increased time-of-flight of particles travelling in-between the two condensate nodes becomes noticeable and reduces the complex coherence factor g_{12} of the non-stationary system with finite life-time. More detailed studies on coupled ballistic polariton condensates under non-resonant pulsed excitation are presented in Chapter 6.

5.3.6 Multi-mode condensation

While at moderate pump powers ($P < 2P_{\mathrm{thr}}$) we observe dominant occupation of only one or two modes in the spectra of two coupled polariton condensates, for larger pump powers ($P > 2P_{\mathrm{thr}}$) and, hence, increased non-linear interaction energy a transition into

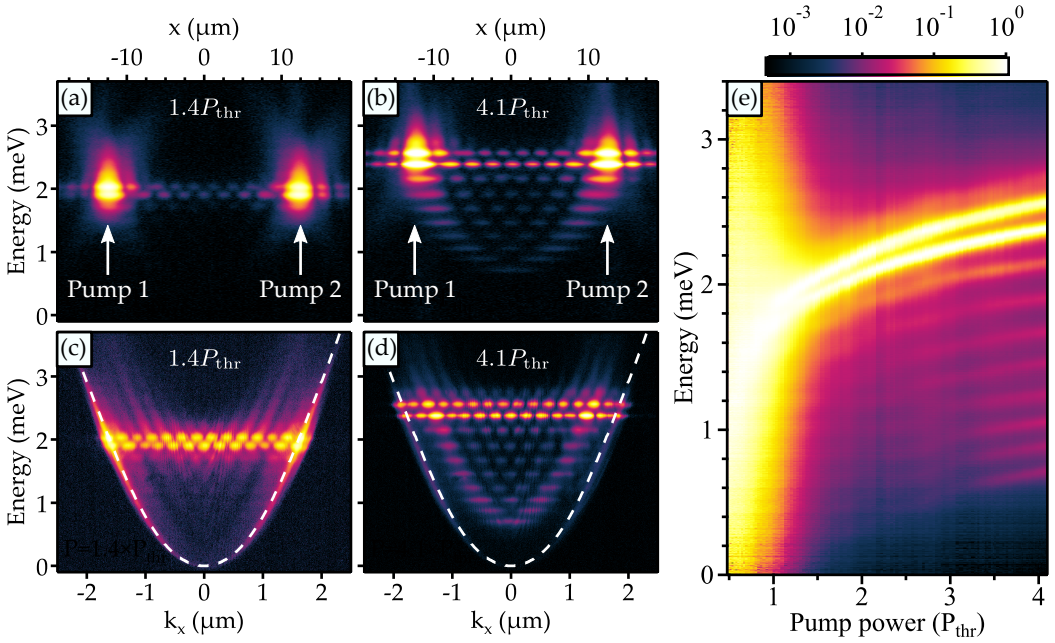

FIGURE 5.10: **Multi-mode condensation of polariton condensates at large pump powers.** (a,b) Spectrally resolved real space emission and (c,d) spectrally resolved momentum space emission of two condensates with pump spot separation distance $d \approx 25$ μm for pump powers $P = 1.4P_{thr}$ and $P = 4.1P_{thr}$. White arrows in (a,b) mark the pump spot locations, and white dashed curves in (c,d) represent the LP branch in the linear regime. (e) Normalised spectra of the two-condensate system with continuously increasing pump power P indicating the transition to multi-mode emission.

multi-mode condensation becomes apparent. Spectrally resolved real space and momentum space emission images of a polariton dyad with pump spot separation distance $d \approx 25$ μm are shown in Fig. 5.10(a-d) for moderate and large cw pump powers, respectively. At smaller pump power $P = 1.4P_{thr}$ [Fig. 5.10(a,c)] only two modes are macroscopically occupied, and both of them share large spatial overlap with the laser-induced pump spot locations (white arrows). This state resembles periodic population oscillations between two ballistically coupled condensation centres described in Section 5.3.3.

At larger pump power $P = 4.1P_{thr}$ [Fig. 5.10(b,d)] a clear blue-shift of the emission spectrum and the occupation of additional lower-energy modes are present. These spectral modes resemble the eigenmodes of the quantum harmonic oscillator formed by the pump-induced near-parabolic confinement potential along the dyad-axis [34]. The appearance of 'trapped condensates' [35] for increasing pump power is attributed to the increased gain of the low-energy modes penetrating into the laser-induced spatially localised gain regions, and to the increased nonlinear particle interactions facilitating efficient relaxation to the equidistant energy modes of the near-parabolic potential [34]. Mode-locking of the trapped condensation modes further leads to the formation of non-dispersive polariton wavepackets (solitons) oscillating between the two pump spots [34, 99]. The continuous transition of the two-spot system from dual-mode

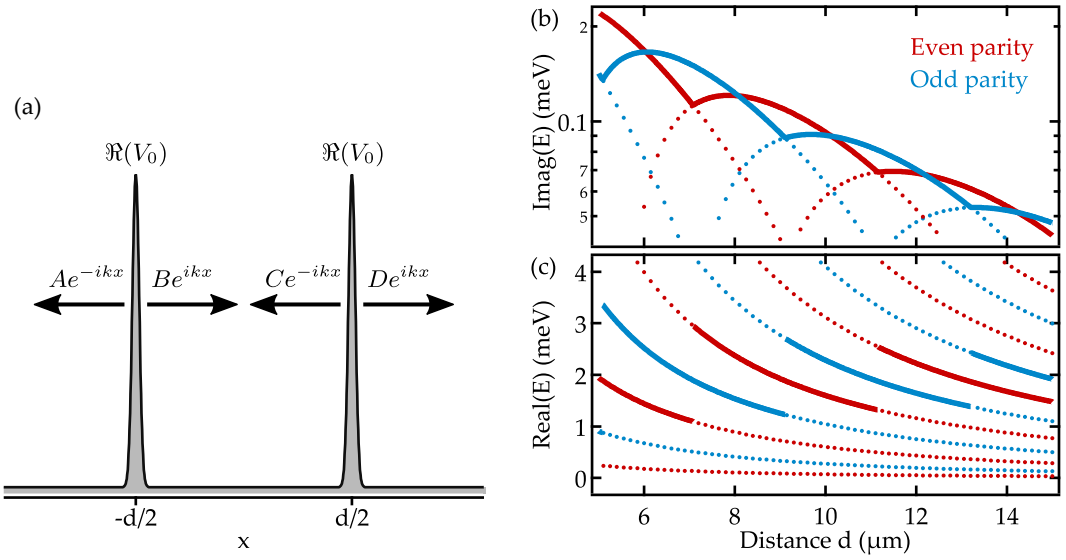

FIGURE 5.11: **Resonances of two complex-valued δ-shaped potentials.** (a) Schematic showing the potential landscape $V(x)$ of the one-dimensional Schrdinger equation. Calculated (b) imaginary and (c) real parts of the eigenvalues $E_{n,\pm}$ in Eq. 5.15. The two solutions with largest gain (imaginary part of E) are illustrated as solid lines; other solutions are shown as dotted branches. Numerical parameters: $\Re(V_0) = 1$ meV μm, $\Im(V_0) = 2$ meV μm, $m = 0.28$ meV ps^2 μm^{-2}, $\gamma = 1/5.5$ ps^{-1}. Figure adapted from Reference [78].

condensation at moderate pump powers (small particle densities) to multi-mode condensation at large pump powers (large particle densities) is illustrated in Fig. 5.10(e).

5.4 Analytical description

A simplified analytical description of the presented two-condensate system can be obtained by calculating the resonances of a one-dimensional Schrödinger equation with two complex-valued δ-potentials accounting for the two pump-induced and spatially localised gain centres. The non-hermitian time-independent problem can then be written as

$$E\Psi(x) = \left[-\frac{\hbar^2\partial_x^2}{2m} + V(x) - \frac{i\hbar\gamma}{2}\right]\Psi(x), \tag{5.12}$$

where $V(x) = V_0\delta(x - d/2) + V_0\delta(x + d/2)$ describes two δ-shaped potentials with separation distance d [see schematic in Fig. 5.11(a)]. The complex-valued parameter V_0 describes a repulsive potential wall ($\Re(V_0) > 0$) and gain ($\Im(V_0) > 0$) that is felt by the particle wave function $\Psi(x)$. Eigenfunctions of Eq. 5.12 describing outwards propagating waves with complex-valued wave number k are further written as

$$\Psi(x) = \begin{cases} Ae^{-ikx}, & x \leq -d/2, \\ Be^{ikx} + Ce^{-ikx}, & -d/2 < x < d/2, \\ De^{ikx}, & x \geq d/2. \end{cases} \tag{5.13}$$

The parameters A, B, C and D describe the complex-valued amplitudes of each particle wave depicted in Fig. 5.11(a). Solutions with even parity are described by $A = D$ and $B = C$, whereas for solutions with odd parity one finds $A = -D$ and $B = -C$. The system contains infinitely many resonances of both $(+)$ even and $(-)$ odd parity characterised by the integer number $n \in \mathbb{Z}$:

$$k_{n,\pm} = \frac{i}{d}\left[-\tilde{V} + W_n(\mp\tilde{V}e^{\tilde{V}})\right], \tag{5.14}$$

Here, we have substituted $\tilde{V} = mdV_0/\hbar^2$ and introduced W_n to describe the branches of the Lambert W function. The corresponding complex-valued energies $E_{n,\pm}$ of each resonance are given as

$$E_{n,\pm} = \frac{\hbar^2 k_{n,\pm}^2}{2m} - \frac{i\hbar\gamma}{2}. \tag{5.15}$$

Calculated solutions of the imaginary parts $\Im(E_{n,\pm})$ and real parts $\Re(E_{n,\pm})$ for varying potential separation distances d are depicted in Figs. 5.11(b) and (c). In close analogy to the experimental findings of two ballistically coupled polariton condensates [see Fig. 5.6] the simplified one-dimensional toy-model describes periodic transitions between even and odd parity resonance yielding largest gain [solid lines in Fig. 5.11(b)], as well as the formation of distinct energy branches [solid lines in Fig. 5.11(c)]. Furthermore, while there are periodically alternating regions of even and odd-parity solutions dominating the gain, the transition region is always described by two resonances having equal gain, i.e. dual-mode operation is expected in the transition region.

5.5 Delay-coupled oscillator model

Instead of solving the simplistic one-dimensional Schrdinger equation in Eq. 5.12 exactly, we aim to reformulate the problem as a system of two coupled (condensate) oscillators, where each condensate $i = 1, 2$ causes a ballistically propagating wave $\psi_i(x)$ emerging from the condensation centres. We rewrite the time-dependent wave function $\Psi(x,t)$ as the superposition

$$\Psi(x,t) = c_1(t)\psi(x) + c_2(t)\psi_2(x), \tag{5.16}$$

where $c_{1,2}(t)$ describe the state of each condensate (or oscillator). Normalised forms for the one-dimensional spatial wave functions are given as $\psi_{1,2}(x) = \sqrt{\kappa}\exp\left(ik|x \pm d/2|\right)$ with complex-valued wave number $k = k_c + i\kappa$. In a next step we assume weak coupling between both condensates, i.e. small overlap terms $\xi = \exp(-\kappa d)$, such that any terms of order $\mathcal{O}(\xi^2)$ or higher can be neglected. By substituting Eq. 5.16 into the time-dependent form of Eq. 5.12, and integrating out the spatial degrees of freedom [78], one

obtains

$$i\hbar\dot{c}_i = \left[\frac{\hbar^2k^2}{2m} - \frac{i\hbar\gamma}{2} + \kappa\left(V_0 - \frac{i\hbar^2k}{m}\right)\right]c_i + V_0e^{ikd}c_j, \tag{5.17}$$

where $j = 3 - i$ and $i = 1, 2$ are the two condensate indices. Importantly, the last term in Eq. 5.17 shows that the coupling in-between the two condensates is mediated by a coherent flux of particles with phase-retardation k_cd as opposed to evanescent coupling (tunnelling) in trapped condensate systems. When the amplitudes $c_i(t)$ and $c_j(t)$ are oscillating at a fixed frequency ω, the phase shifting-term k_cd can be transformed into an effective time-delay, i.e.

$$e^{ikd}c_j(t) = e^{-\kappa d}c_j(t - \tau). \tag{5.18}$$

The time-delay $\tau = k_cd/\omega$ represents an interaction lag between both condensation centres due to their spatial separation, and the exponential term $\exp(-\kappa d)$ accounts for the spatial decay of the polariton flux.

By re-introducing polariton non-linear interactions, and the dynamics of reservoirs n_i [see Eq. 3.27 and Eq. 3.28] one can write the full non-linear equation of motion for the two delay-coupled condensates as

$$i\dot{c}_i(t) = \left[\Omega - i\Gamma + \left(g + \frac{iR}{2}\right)n_i(t) + \alpha|c_i(t)|^2\right]c_i(t) + Je^{i\beta}c_j(t - \tau), \tag{5.19a}$$

$$\dot{n}_i(t) = -\left(\Gamma_A + R|c_i(t)|^2\right)n_i(t) + P. \tag{5.19b}$$

Here, Ω and Γ are the condensate eigenfrequency (self-energy) and loss rate, g and R represent reservoir-induced blue-shift and stimulated scattering rate, α is the effective polariton nonlinearity, J and β are magnitude and phase of the coupling term, and Γ_A and P are reservoir loss and pump rate. It is not surprising that equations 5.19 have strong similarity with the Lang-Kobayashi equations [102, 103] used to describe externally coupled lasers subject to time-delayed interaction. While in the case of two externally coupled lasers there is propagation of photons in-between the two cavities, in our case there is propagation of polaritons in-between two gain-centres localised in a two-dimensional microcavity.

The spectra of two ballistically coupled polaritons [see Fig. 5.6] can be reproduced using the delay-coupled oscillator model [Eqs. 5.19] by scaling the coupling strength parameter J with the approximate spatial amplitude of a ballistic polariton condensate,

$$J(d) = J_0|H_0^{(1)}(kd)|, \tag{5.20}$$

and assuming that the time-delay approximately scales proportional to the separation distance, i.e. $\tau = d/v$. Excellent agreement between the spectra obtained from experiment and from the delay-coupled oscillator model is shown in Fig. 5.12 (a), where we illustrate the normalised PSD from experiment (false colour scale), and the numerically

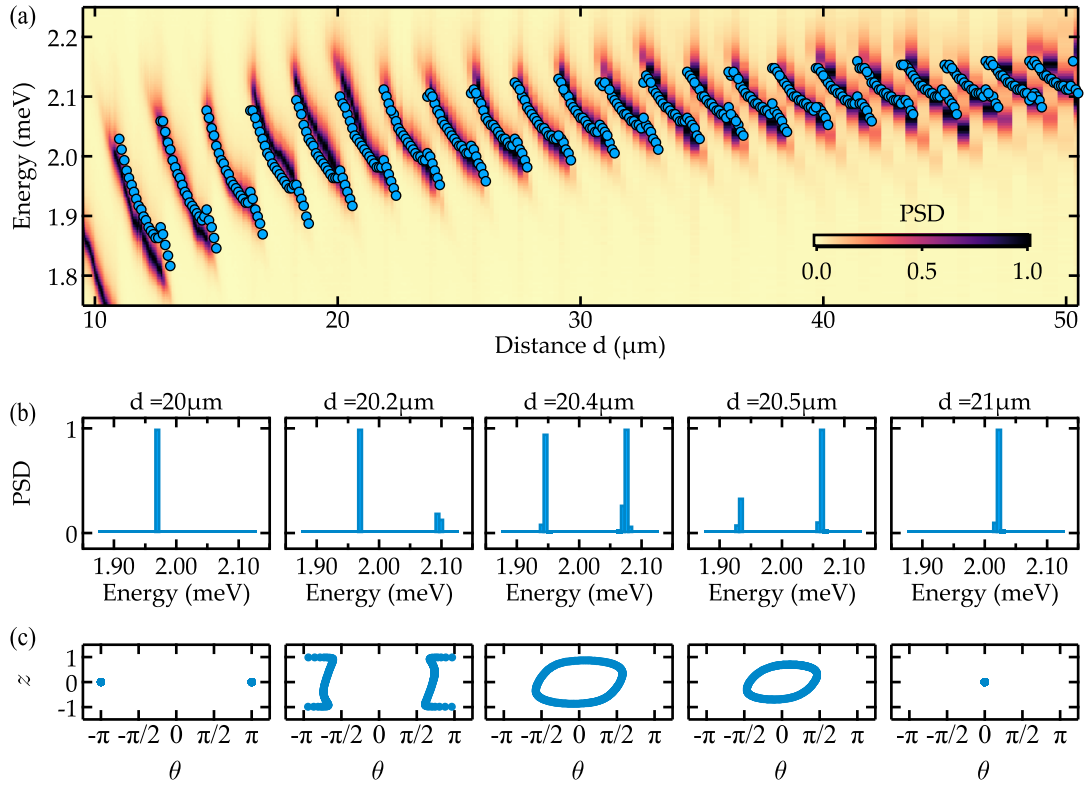

FIGURE 5.12: **Time-delayed coupled polariton condensates.** (a) Comparison of experimentally measured power spectral densities (false colour scale) of two ballistically coupled polariton condensates with separation distance d, and numerically calculated spectral peaks (blue dots) of two delay-coupled oscillators [Eqs. 5.19] with time-delay $\tau = d/v$. (b) Power spectral densities and (c) phase-space diagrams for the anti-phase to in-phase transition of the numerically calculated delay-coupled system for increasing separation distance $d = 20$ μm to $d = 21$ μm. Numerical parameters: $\hbar\Omega = 1.22$ meV, $\hbar\Gamma = 0.5$ meV, $\hbar g = 0.5$ μeV, $\hbar R = 0.5$ μeV, $\hbar\alpha = 0.1$ μeV, $v = 1.9$ μm ps^{-1}, $P = 100$ ps^{-1}, $\Gamma_A = 0.05$ ps^{-1}, $\hbar J_0 = 1.1$ meV, $\beta = -1$, and $k = (1.7 + 0.014)$ μm^{-1}. Figure adapted from Reference [78].

calculated spectral peak from Eqs. 5.19 (blue dots) when in single mode operation, or the two most dominant spectral peaks when multiple spectral components exist.

Numerical integration of Eqs. 5.19 for increasing separation d also reproduces the experimental findings of periodic parity-flip transitions accompanied by periodic solutions (population oscillations) in the transition region. In particular, we illustrate the spectral transition of the delay-coupled oscillator system from an anti-phase to an in-phase synchronisation configuration in Fig. 5.12(b). The corresponding phase-space diagrams are pictured Fig. 5.12(c) showing periodic orbits in the transition region, and involve oscillations in the population imbalance $z = (|c_1|^2 - |c_2|^2)/(|c_1|^2 + |c_2|^2)$ and the phase difference $\theta = \arg(c_1^* c_2)$.

5.6 Conclusion

Ballistically expanding polariton condensates offer a platform for exploring optically controllable synchronous phases in coupled condensate networks. Synchronisation of two condensates over macroscopic distances $d > 100$ μm have been realised [78], highlighting the prospect for applications in extended configurations. We observe that the dynamics of two ballistically coupled polariton condensation centres is not dictated by two hybridized (binding and anti-binding) modes [111], but by an infinite amount of coupled modes that can be considered as the Fabry-Perot resonances of an effective complex-valued double-δ-potential. The introduction of time-delay into a set of coupled oscillator equations fully reproduces the experimentally observed phenomena, and describes polariton condensates as picosecond, nonlinear oscillators subject to time-delayed interactions. The intrinsic high-dimensional state space of delay-coupled systems makes ballistically coupled polariton condensates a promising platform to investigate neuro-inspired classification tasks such as pattern and speech recognition [112, 113, 114].

5.7 Disclaimer

Experimental studies presented in this Chapter were conducted by J. D. Töpfer, L. Pickup, and T. Cookson. Theoretical description and numerical simulations were carried out by J. D. Töpfer, and H. Sigurdsson. Figures and text description presented in this Chapter are adapted from published References [78] and [89].

Chapter 6

Engineering Coherence In Networks Of Polariton Condensates

The transition into synchrony and the formation of coherence between coupled elements is a universal concept arising in nature and technology [5]. In our previous discussions we have detailed on the synchronisation of macroscopic entities such as two coupled metronomes [see Section 2.3], as well as the emergence of spatial coherence across a driven-dissipative quantum system realised in semiconductor microcavities [see Chapter 5]. In either case, synchronisation between two oscillating mechanical pendulums or between two ballistically expanding polariton condensates is manifested in the formation of a fixed phase relationship between the two nonlinear oscillating elements [see Section 2.2]. Stability of such phase-locked states generally depends on the inter-element coupling strength in competition with any present dephasing mechanisms and, therefore, limiting noise sources and reducing any oscillator frequency mismatch is key to improve synchrony. Furthermore, in larger systems consisting of many coupled elements the underlying coupling topology (or network architecture) is known to critically influence the system dynamics and formation of coherence [115]. In technological applications the engineering of spatial coherence in large coupled networks is then an important element for increasing system performances as in power-grid networks [116], neuroinspired computational devices [117], and laser arrays [118].

Coherent phenomena in networks and lattices of coupled condensates are investigated for the study and simulation of phase transitions and computationally complex tasks such as in atomic [30, 119], photonic [97] and polaritonic [39, 41, 120] platforms. While the performance of these laboratory systems is ultimately limited by the systems spatial coherence length (i.e. how many condensates can coherently be coupled), large-scale synchronisation in lattices is often hindered by an inhomogeneous distribution of natural frequencies (energies), e.g. due to an unavoidable disorder potential [121].

In this Chapter we detail on the application of a feedback laser scheme [see Section 4.2.2] to balance the condensate density across networks and lattices of ballistically coupled polariton condensates. By doing so we overcome the challenges of mode localization and condensate dephasing due to sample non-uniformities and non-homogeneous gain distribution. Density-stabilisation of polariton lattices results in a homogeneous and macroscopically coherent state with near-diffraction limited far field emission. Furthermore, we detail on the critical implications of dimensionality and connectivity of the lattice architecture (i.e. number of neighbouring condensate sites) onto power consumption and spatial coherence properties in lattices of driven-dissipative condensates. The results presented in this Chapter have been published in Reference [89].

6.1 Experimental methods

The experimental techniques for both excitation and detection of coupled polariton condensates are described in Section 4.3 and Section 4.4 of this thesis. The iterative algorithm for active stabilisation of the condensate node emission intensities in optically excited networks and lattices is described in Section 4.2.2. All experimental results presented in this Chapter are acquired using non-resonant sub-picosecond pulsed laser excitation with circular polarisation. While we are typically limited to structures of < 100 condensates with cw laser excitation, the use of pulsed excitation allows for the generation of coherent lattices with > 100 condensates. The sample in use is a GaAs-based planar microcavity, which is described in Section 4.3, and operated at a negative (photonic) detuning ($\Delta \approx -5$ meV).

6.2 Condensate density stabilisation

The iterative algorithm for homogenisation of spatial laser profiles described in Section 4.2.2 of this thesis is applied to the emission intensities of non-resonantly excited and ballistically coupled polariton condensates. A schematic of the experimental implementation is illustrated in Fig. 6.1(a). We operate a phase-only SLM in the Fourier plane of the optical excitation setup allowing for holographic control over the (pump) laser spatial profile on the microcavity sample plane. Iterative read-out of the condensate emission, and nonlinear adjustment of the excitation pump profile allows us to engineer macroscopic polariton lattices (> 100 nodes) with homogeneous condensate node density distribution (typically < 1 % RSD).

We find good results for stabilising the density distribution in coupled polariton networks pumped at condensation threshold $P \gtrsim P_{\text{thr}}$. Stabilisation at larger pump powers $P \gg P_{\text{thr}}$, however, is impeded using the presented technique - which operates at

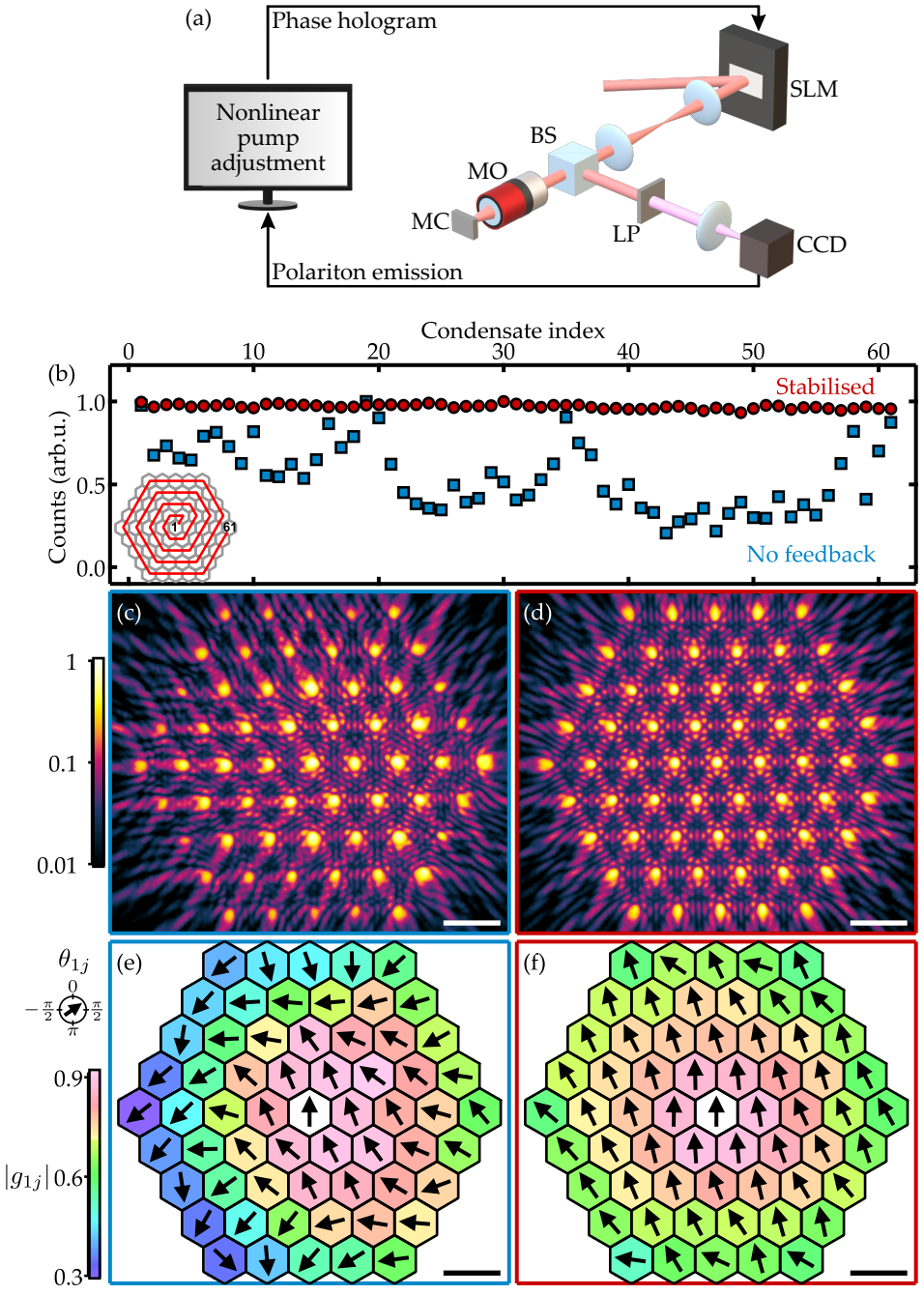

FIGURE 6.1: **Condensate density stabilisation in polariton lattices.** (a) Schematic of the experimental feedback loop that iteratively analyses the condensate emission and adjusts the spatial pump profile in order to equalise the condensate emission intensity across the whole lattice. (b) Integrated emission intensities of 61 condensates at condensation threshold ($P = P_{\text{thr}}$) arranged in a triangular configuration with lattice constant $a = 14.9$ μm for (blue squares) no condensate density stabilisation and (red circles) with stabilisation. Inset shows the condensate number indexing. (c,d) Recorded real space emission and (e,f) measured complex coherence factor g_{1j} between the central condensate node 1 and each other condensate node $j = 2, ..., 61$ without and with condensate density stabilization, respectively. False colour-scale and pseudo-spins (black arrows) in (e) and (f) depict magnitude g_{1j} and phase $\theta_{1j} = \arg(g_{12})$. Data shown in (c-f) are extracted at a total pump power $P = 1.2P_{\text{thr}}$. Scale bars in (c-f) correspond to 20 μm. The Figure is adapted from Reference [89].

a typical rate of 60 Hz - because of stronger nonlinear effects resulting in nonstationary condensate dynamics on a picosecond timescale [see Section 5.3.6]. We note that the described method of iterative condensate density stabilisation is applicable to both periodic and non-periodic structures of polariton condensates.

A comparison of an experimentally realised polariton triangular lattice (61 condensate nodes, lattice constant $a = 14.9$ μm) with and without density stabilisation is summarised in Figs. 6.1(b-f). In particular, the averaged emission intensities within the FWHM of each condensate node at condensation threshold $P = P_{\text{thr}}$ is illustrated in Fig. 6.1(b). Without condensate feedback, i.e. by using the conventional GS algorithm for generation of pump laser profiles, a broad distribution of condensate emission intensities becomes apparent with large spread $\approx$ 37 % (RSD). It originates from a non-homogeneous distribution of effective gain for each condensate node and is caused by multiple factors, such as the finite accuracy of the GS algorithm, optical aberrations in the excitation system, an unavoidable sample disorder potential, and edge-effects due to the finite size of the lattice [101]. Compensation of these detrimental effects is achieved by active stabilisation of the lattice node densities via the described closed-loop feedback mechanism with density distribution spread of $\approx$ 1 % (RSD), which is only limited by noise in the experimental system.

The effects of density stabilisation onto symmetry and coherence of the macroscopic polariton system are particularly perceivable in the real space condensate emission images displayed in Figs. 6.1(c) and (d) for system realisations without and with stabilisation, respectively. In both cases, the presence of interference fringes in-between the ballistically expanding condensates is a result of phase-locking between nearest neighbour (NN) condensates. However, in case of no active density stabilisation [Fig. 6.1(c)] there is a lack of symmetry in spatial orientation of interference fringes across the lattice, indicating a broad distribution of relative phase differences θ_{ij} between condensation centres. The striking homogeneity of node densities and interference fringe patterns in case of active stabilisation [Fig. 6.1(d)] implies in-phase synchronisation ($\theta_{ij} = 0$) and the presence of long-range order across the whole triangular lattice.

Enhanced coherence properties of the stabilised condensate lattice are revealed by direct measurements of the complex coherence factor g_{ij} between pairs of condensate nodes [see Section 4.4.4 for methods]. In Fig. 6.1(e) and (f) we illustrate magnitude $|g_{1j}|$ and phase θ_{1j} of the coherence factor between the central condensate node (index 1) and each other condensate node (index j) within the triangular lattice using false colour scale and pseudo-spins (black arrows). In case of active density stabilisation [Fig. 6.1(f)], there is an enhanced and isotropic decay of spatial coherence $|g_{1j}|$, as well as a more homogeneous distribution of relative phase differences θ_{1j}. The reduced coherence properties and broader distribution of phase differences for the non-stabilised polariton lattice [Fig. 6.1(e)] are the result of the spatially varying density distribution, causing different blue-shifts (or eigenenergies) and different particle fluxes across the

lattice nodes. We note that similar results have been described in Section 2.3 for the case of two coupled phase-oscillators, where unequal oscillator properties in the form of a frequency detuning Δ was shown to cause both a phase drift, and reduced coherence properties.

The slight increase of phase differences θ_{1j} (or rotation of pseudo-spins) towards the edges of the stabilised triangular polariton lattice [Fig. 6.1(f)] is an expected finite-size effect and is related to the finite flux of particles escaping the system [101]. In the case of an ideal triangular lattice of infinite size, one would expect a homogeneous distribution of phases with $\theta_{ij} = 0$ for all condensate pairs due to translational invariance [see Section 6.3.3 for details].

6.2.1 Near-diffraction limited emission of stabilised condensate networks

In close analogy to 'time-of-flight' expansion measurements utilised in cold-atom systems [70] and beam interference experiments in coupled laser arrays [122], the global coherence properties in polariton condensate lattices can be probed by far field measurements. To remove residual PL coming from polaritons outside the condensation (gain-)centers we spatially filter the emission of each condensation centre using a programmable aperture described in Section 4.4.4, and measure the interference of the masked condensate emission in the far field.

As schematically shown in Fig. 6.2(a) we project the condensate near field PL [Fig. 6.2(b)] onto the programmable aperture consisting of a triangular lattice of point-like holes [Fig. 6.2(c)], and subsequently image the diffraction pattern (far field interference) onto a recording CCD sensor [Fig. 6.2(d)]. The measurable intensity pattern $I(\mathbf{k})$, expressed in reciprocal space coordinates $\mathbf{k}$, is innately linked to the coherence properties of the condensate lattice [see Eq. 4.18],

$$\hat{I}(\mathbf{k}) = A^2 \sum_{i,j} \Gamma_{ij} e^{i\mathbf{k}\mathbf{d}_{ij}}, \tag{6.1}$$

where A expresses the finite physical size of each aperture hole, and Γ_{ij} and $\mathbf{d}_{ij} = \mathbf{x}_i - \mathbf{x}_j$ are mutual intensity and displacement of each pair of condensates. Of particular interest is the limiting case of a fully-coherent lattice with $\Gamma_{ij} = I_0$ for all pairs of condensates, such that the far field diffraction pattern reduces to the well-known Fraunhofer diffraction formula,

$$\hat{I}(\mathbf{k}) = A^2 I_0 \left| \sum_i e^{i\mathbf{k}\mathbf{x}_i} \right|^2. \tag{6.2}$$

It is apparent from Eq. 6.2 that in case of a periodic structure (lattice) of identical and fully-coherent light sources sampled at locations x_i, the far field intensity pattern $\hat{I}(\mathbf{k})$ displays the system's reciprocal lattice. The appearance of the reciprocal triangular

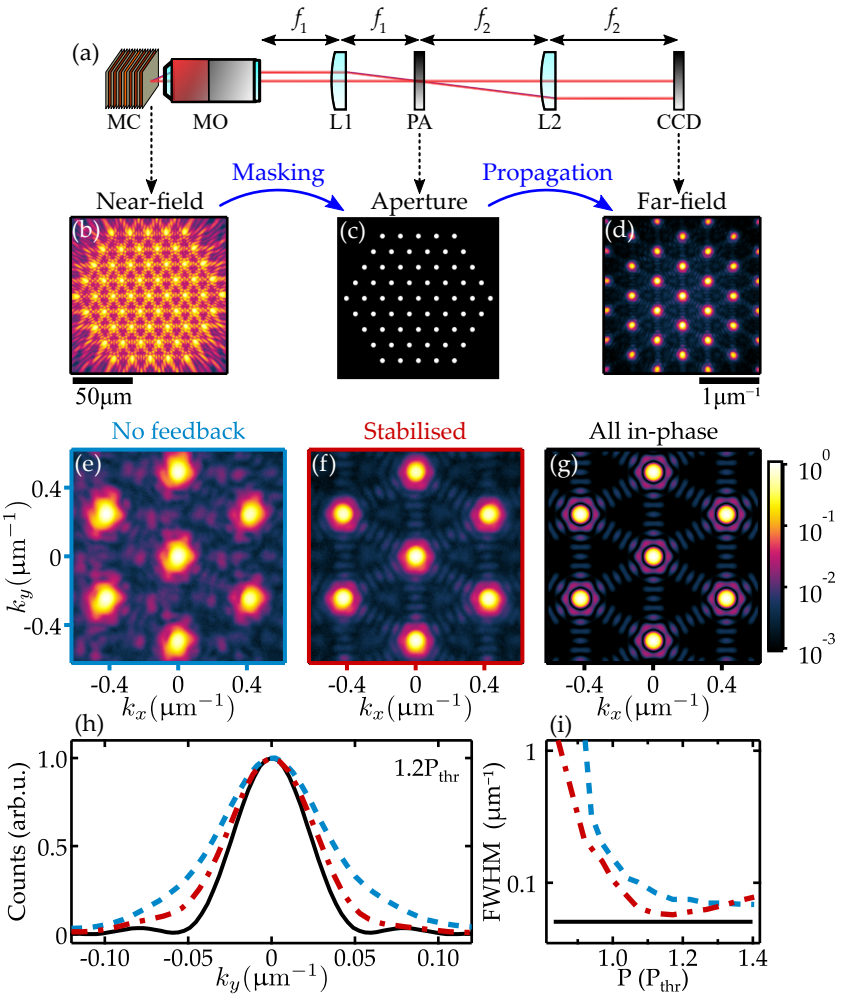

FIGURE 6.2: **Near-diffraction limited emission of a stabilised polariton lattice.** (a) Schematic of the experimental detection setup with microcavity (MC), microscope objective lens (MO), lenses (L1,L2), programmable aperture (PA) and charge-coupled device (CCD). (b) Real space PL, (c) real space masking aperture and (d) corresponding far field interference pattern of a triangular polariton lattice consisting of 61 condensate nodes. Zoom into the first Brillouin zones of the far field condensate emission for excitation (e) without feedback and (f) with feedback. (g) Analogous far field emission of a calculated ideal system consisting of 61 fully-coherent point sources. (h) Intensity profiles of the central Bragg peak along the symmetry axis $k_x = 0$ for the far field emission of (blue dashed) the non-stabilised lattice, (red dash-dotted) the stabilised lattice, and (black solid) the diffraction limited case of a fully-coherent lattice. (i) Corresponding pump power dependencies of the central Bragg peaks' FWHM. Data shown in (b,d,e,f) are recorded at pump power $P = 1.2P_{\text{thr}}$ and are illustrated using the same logarithmic colour scale shown for (g). The Figure is adapted from Reference [89].

lattice shown in Fig. 6.2(d), therefore, indicates the presence of long-range coherence across the lattice of condensation nodes [Fig. 6.2(b)].

A zoom into the first Brillouin zones of the recorded far-field emission pattern for the triangular condensate lattice excited without and with density stabilisation are illustrated in Figs. 6.2(e) and (f), and compared to the calculated far-field emission pattern of 61 superimposed fully coherent point-sources in equivalent periodic arrangement

[Eq. 6.2] as shown in Fig. 6.2(g). While there is good agreement between the measured far field emission of the stabilised polariton condensate lattice and the calculated reciprocal space intensity of a fully-coherent in-phase lattice, deviations of the non-stabilised lattice from the ideal fully-coherent system highlight its reduced coherence properties.

Comparison of the lobe intensity profiles of the central far field emission (Bragg) peak located at $\mathbf{k} = 0$ is shown in Fig. 6.2(h). We note that the presented emission lobe profile of the ideal full-coherent system (black line) represents the diffraction limited interference peak. The increased widths of the experimentally measured peaks with (red dash-dotted line) and without (blue dashed line) density stabilisation are then the result of finite coherence length. The extracted FWHM of the central interference peak for varying laser pump power P is shown in Fig. 6.2(i). Near-diffraction limited emission of the stabilised condensate lattice is found at $P = 1.17P_{\text{thr}}$ with an emission lobe width that is ≈ 14 % larger than the diffraction limited spot size. Reduced coherence in the non-stabilised lattice result in a spot width that is ≈ 49 % larger than in the case of a fully-coherent system.

6.3 Spatial coherence in polariton lattices

By utilising the described methods for all-optical generation of homogeneous (density-stabilised) arrangements of polariton condensation centres, we engineer various networks and lattice types of ballistically coupled condensates within the same defect-free sample area. Therefore, by eliminating physical differences between different microcavity samples or different sample locations, we can accurately study the dependency of system power efficiency and coherence properties on the underlying coupling topology.

6.3.1 A polariton chain

In a first step, we investigate a stabilised linear array (chain) of 11 equidistant polariton condensates with lattice constant $a = 12.1$ μm. The chosen condensate spacing yields single-mode emission and favours anti-phase synchronisation between NN condensation centres. Experimentally recorded real space and momentum space emission patterns of the polariton chain pumped at $P = 1.2P_{\text{thr}}$ are shown in Figs. 6.3(a) and (b). The real space periodic interference pattern appearing in horizontal direction depicts a polaritonic analogue of the optical Talbot effect [123].

Measured magnitude $|g_{ij}|$ and phase θ_{ij} of the complex coherence factor between any pair of condensates is shown in matrix form in Fig. 6.3(c). Row and column indices i and j denote the the pair of condensates [indices denoted in Fig. 6.3(a)], and due to Hermiticity of the correlation matrix we make use of the relation $g_{ij} = g_{ji}^{*}$. While the system

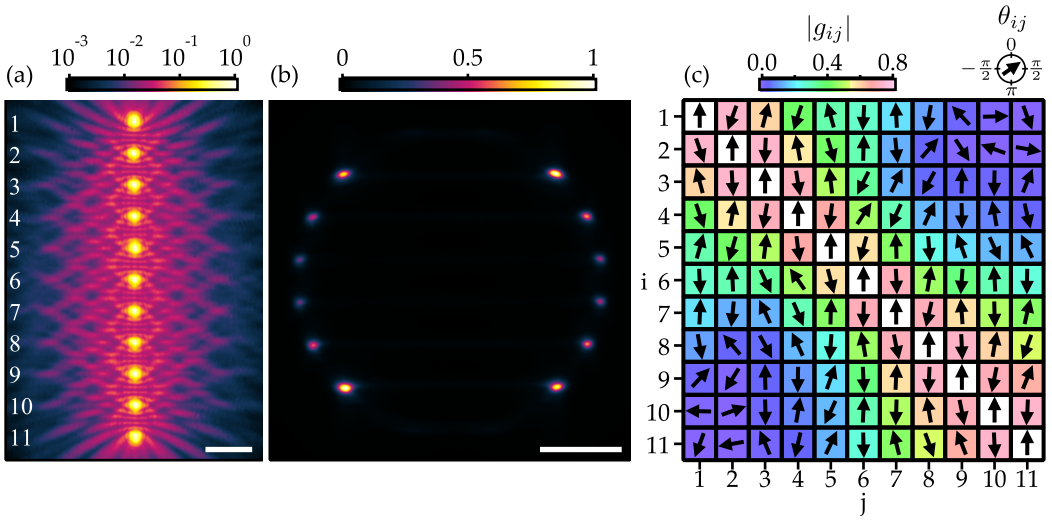

FIGURE 6.3: **A polariton chain of ballistically coupled condensate nodes.** Recorded (a) real space and (b) momentum space emission of 11 density-stabilised condensate nodes arranged in a chain with separation distance $a = 12.1$ μm. The pump power is kept at $P = 1.2P_{\text{thr}}$ for all data shown. (c) Correlation matrix showing magnitude and phase of the measured complex coherence factor g_{ij} between any pair of condensate nodes. Condensate indexing is shown in (a). Scale bars in (a) and (b) correspond to 20 μm and 1 μm^{-1}, respectively. The Figure is adapted from Reference [89].

exhibits strong anti-phase synchronisation between NNs, there is a loss of anti-phase order for increasing separation distances $|i - j| \gg 1$, i.e. towards the off-diagonal matrix elements. The spatial decay of coherence in the polariton chain is further described in Section 6.3.4 and compared to other lattice types.

6.3.2 A polariton square lattice

In a next step, we increase the dimensionality of the coupled condensate network by investigating an 11×11 polariton square lattice of equivalent lattice constant $a = 12.1$ μm. Recorded real space and momentum space condensate emission patterns are shown in Figs. 6.4(a) and (b) for an excitation laser pump power $P = 1.2P_{\text{thr}}$. The regularity and large visibility of real space interference patterns, as well as the distinct diffraction pattern appearing in reciprocal space both indicate anti-phase synchronisation between NNs and macroscopic coherence across the lattice.

Measured magnitude $|g_{1j}|$ and phase θ_{1j} of the complex coherence factor between the central condensate node located at $\mathbf{x} = 0$ (index 1) and each other condensate node (index $j = 2, ..., 121$) are shown in the correlation map in Fig. 6.4(c). The observed anti-phase ordering for NNs is isotropically decaying with increasing condensate node separation distance, i.e. towards the edges of the lattice. However, we note that coherence $|g_{1j}|$ does not drop below 0.3 for the given separation distances as large as $d_{1j} \approx 86$ μm (center-to-edge distance). Further discussion of the spatial decay of coherence in the polariton square lattice and comparison to other systems is given in Section 6.3.4.

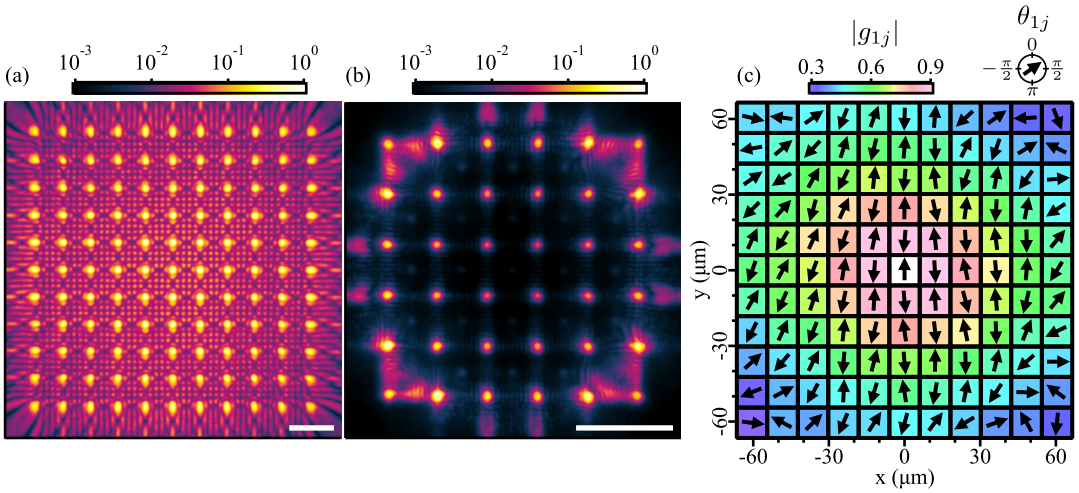

FIGURE 6.4: **A two-dimensional polariton lattice of ballistically coupled condensate nodes.** Recorded (a) real space and (b) momentum space emission of 121 density-stabilised condensate nodes arranged in a square lattice with lattice constant $a = 12.1$ μm. The pump power is kept at $P = 1.2P_{\text{thr}}$ for all data shown. (c) Spatial coherence map showing magnitude and phase of the measured complex coherence factor g_{1j} between the central condensate node (index 1) and any other condensate node (index $j = 2, ..., 121$). Scale bars in (a) and (b) correspond to 20 μm and 1 μm^{-1}, respectively. The Figure is adapted from Reference [89].

6.3.3 Finite-size versus infinite lattices

Finite-size effects in polariton condensate lattices cannot be avoided in an experimental setting, but can effectively be reduced by increasing the lattice size. In coherence measurements presented in Fig. 6.1(f) and Fig. 6.4(c) a loss of phase-coherence (or rotation of pseudo-spins) towards the edges is observed and attributed to the finite system size and its concomitant finite flux of particles through the boundaries of the system [101].

For numerical simulations finite system sizes must be taken into account as well, although edge effects can effectively be avoided by applying periodic boundary conditions. A comparison of numerical simulations of the two dimensional GPE for a square lattice of ballistically expanding polariton condensates without and with periodic boundary conditions is shown in Fig. 6.5. In case of no periodic boundary conditions ('finite size lattice') there is a distinct rotation of phases θ_{1j} towards the edges of the lattice, which is in good agreement with experiment [Fig. 6.4(c)]. When removing the non-zero flux of particles escaping the system by applying periodic boundary conditions ('infinite lattice') to the numerical simulations, a homogeneous distribution of phases $\theta_{1j} = 0, \pi$ emerges as shown in Fig. 6.5(d). In fact, the translational invariance present in the infinite system (realised by periodic boundary conditions) leads to spatially invariant coherence properties.

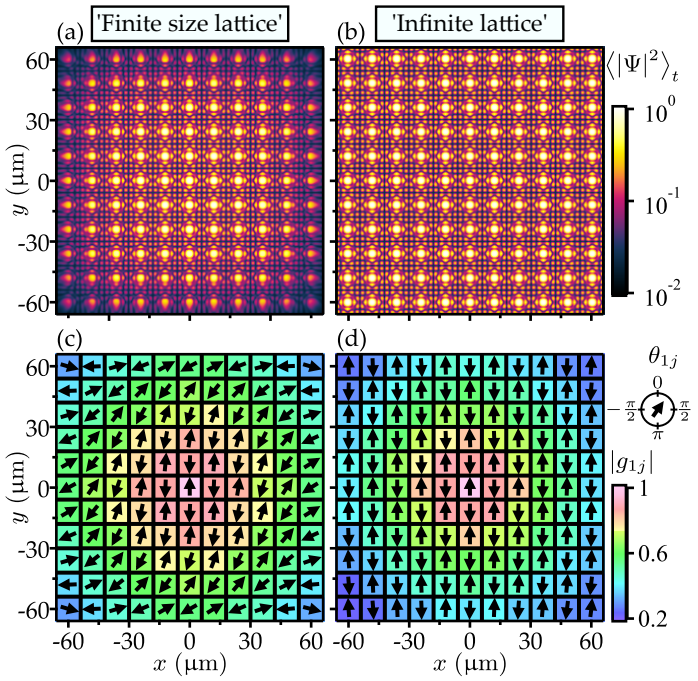

FIGURE 6.5: **Finite-size effects in polariton lattices.** Numerical simulation of the GPE for a square lattice of ballistically expanding polariton condensates with damped (a,c) and periodic boundary conditions (b,d) under non-resonant pulsed excitation. (a,b) Time-integrated condensate density $\langle|\Psi|\rangle_t$ and (c,d) complex coherence factor g_{1j} between the central condensate node (index 1) and each other node (index j). The lattice constant is $a = 12$ μm. The Figure is adapted from Reference [89].

6.3.4 Enhanced coherence in coupled lattices

Comparison of the experimentally determined spatial coherence properties of ballistically coupled polariton condensates is summarised in Fig. 6.6 for the previously described network architectures; two coupled condensates (dyad, see Fig. 5.9), a 1D chain [see Fig. 6.3], and 2D square (see Fig. 6.4) and triangular lattices (see Fig. 6.1). In particular, the effective spatial decay of coherence $|g_{ij}|$ with increasing condensate node separation distance d_{ij} in each network is shown in Fig. 6.6(a). In case of the 1D and 2D periodic structures, the data points for different distances d_{ij} correspond to different pairs of condensates $\{i, j\}$ within each system. For the polariton dyad, the physical separation distance d_{12} between two condensation nodes is varied while keeping the pump power P constant.

As previously described in Section 5.3.5 the spatial decay of coherence $|g_{12}|$ for the two-condensate system with varying separation distance d_{12} is well described by a Gaussian decay [grey solid curve in Fig. 6.6(a)] and an effective coherence length $L_c \approx 25$ μm (see Eq. 5.11). While this effective coherence length does not describe the spatial coherence properties within one system realisation, it is a measure for the distance over which coherent coupling of the two condensates is possible. On the other hand, the experimentally determined spatial decay of coherence $|g_{ij}|$ in 1D and 2D periodic structures

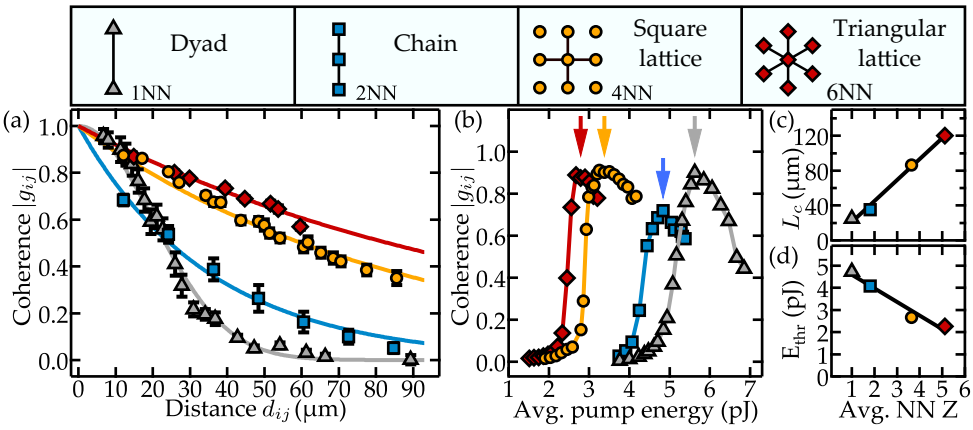

FIGURE 6.6: **Comparison of spatial coherence in different networks and lattices of ballistically coupled polariton condensates.** (a) Measured spatial decay of (grey triangles) a two-condensate system with variable separation distance, (blue square) a chain with lattice constant $a = 12.1$ μm, (yellow circles) a square lattice with lattice constant $a = 12.1$ μm, and (red diamonds) a triangular lattice with lattice constant $a = 14.9$ μm. Solid curves represent a Gaussian fit for the two-condensate system, and exponential fits for the 1D and 2D periodic structures, respectively. (b) Excitation pulse energy dependence of the coherence $|g_{12}|$ between the central-most condensate node (index 1) and one of its NNs (index 2) for the 1D and 2D periodic structures, and between two condensates with distance $d_{12} = 12.7$ μm for the case of a dyad. Arrows in (b) indicate the pump power $P \approx 1.2P_{\text{thr}}$ used for measurements presented in (a). Extracted (c) effective coherence length L_c and (d) threshold pump energy E_{thr} versus the average number of NNs Z of each network type. Figure adapted from Reference [89].

is well described by an exponential decay, which is in agreement with previous results on trapped polariton lattices [121]. Fitting of the experimental data with exponential curves [see Fig. 6.6(a)] yield coherence lengths of $L_c \approx 35$ μm, $L_c \approx 87$ μm, and $L_c \approx 120$ μm for the polariton chain, square lattice, and triangular lattice, respectively.

Differences in system performances between the studied condensate networks become further visible in their respective pump power dependencies. Figure 6.6(b) shows the measured absolute value of coherence $|g_{12}|$ between a NN condensate pair versus the average pump pulse energy per condensate node. In case of the polariton dyad, a condensate separation distance of $d_{12} = 12.7$ μm is chosen, and is comparable to the NN distances (lattice constant) of the investigated 1D and 2D periodic structures. While all configurations show a similar pump-dependency of their coherence properties with a coherence maximum appearing at $P \approx 1.2P_{\text{thr}}$, their threshold pump energy per condensate node can strongly deviate. In particular, we find a threshold pulse energy of ≈ 4.7 pJ and ≈ 2.3 pJ per condensate node for the polariton dyad and the polariton triangular lattice, respectively.

Importantly, as summarised in Figs. 6.6(c) and (d), polariton networks are characterised by both, an increase of the (effective) coherence length L_c, and by a decrease in threshold pump energy per condensate node for network architectures with larger connectivity, i.e. larger number of NN couplings Z. As we argue in the following, both effects

originate from an increased coherent exchange of particles between neighbouring condensates.

For simplicity in our analysis we project the whole system dynamics onto a discretised set of equations consisting of coupled condensates c_i and reservoirs n_i [see Eqs. 5.19], and write the steady state solution of frequency ω as

$$\omega c_i = \left[\Omega - i\Gamma + \left(g + \frac{iR}{2}\right) n_i + \alpha|c_i|^2\right] c_i + (J_R + iJ_I) \sum_{j \in \mathrm{NN}} c_j, \tag{6.3a}$$

$$n_i = \frac{P}{\Gamma_A + R|c_i|^2}. \tag{6.3b}$$

Here, we have neglected any couplings beyond nearest neighbours, and split the NN coupling strength into its real part J_R and imaginary part J_I. Further, we do not allow for any geometric phase frustration, e.g. by assuming a positive imaginary coupling strength $J_I > 0$ producing a symmetric (in-phase) state, i.e. $c_i = c_j$ and $n_i = n_j$ for all i and j. In this simplistic model the threshold pump power P_{thr} per condensate node, as well as the reservoir populations n_i are determined from Eqs. 6.3 by the interplay of intrinsic condensate loss rate Γ and coherent gain provided by Z coupled condensates,

$$P_{\mathrm{thr}} = \frac{2\Gamma_A}{R} \left(\Gamma - ZJ_I\right), \tag{6.4a}$$

$$n_i = \frac{2}{R} \left(\Gamma - ZJ_I\right). \tag{6.4b}$$

It is apparent that an increase in coupling strength J_I and/or increase in the number of coherently coupled NN condensates Z is therefore innately linked to both, a reduction of threshold pump power P_{thr}, and a reduction in the number of uncondensed reservoir particles n_i.

It is well known that interactions between polaritons and uncondensed particles play a dominant role in the condensate decoherence processes [124, 125, 126]. Therefore, and in agreement with experimental results shown in Fig. 6.6(c) and in Fig. 5.7(d), the coherent coupling of non-resonantly excited polariton condensates is generally expected to enhance spatial and temporal coherence properties. We note that in a similar principle, reduced condensate-reservoir interaction energy is realised in optically trapped structures and shown to yield improved coherence times exceeding 1 ns [127].

The strengthening of spatial correlations in densely connected polariton lattices, mediated through the coherent coupling of condensate nodes, is well visualised in Fig. 6.7. Here, we compare the mutual coherence between two macroscopically separated condensates ($d_{12} = 172$ μm) in a polariton dyad [Fig. 6.7(a)] and a square lattice [Fig. 6.7(b)]. In case of the two-condensate system, the measured far field interference pattern shown in Fig. 6.7(c) reveals the incoherent superposition of both condensate signals. The coupling between the two macroscopically separated condensates, which is limited by the

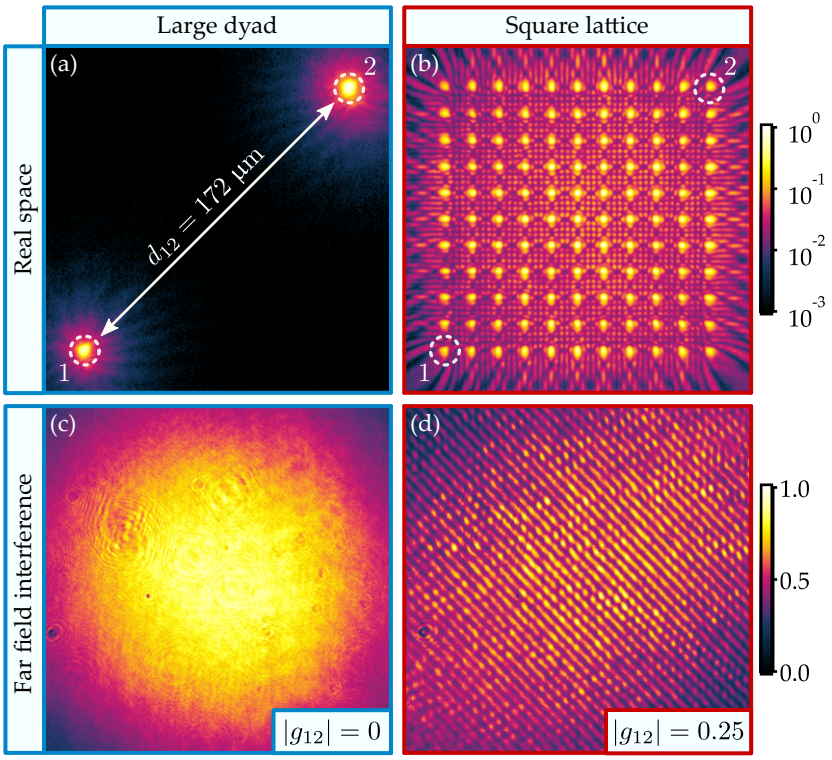

FIGURE 6.7: **Macroscopic coherence in polariton lattices.** Real space emission of (a) two polariton condensates with separation distance $d_{12} = 172$ µm and (b) an 11×11 square lattice with lattice constant $a \approx 12.1$ µm. Young's double hole interference pattern of (c) the two-condensate system, and (d) between the two out-most condensates within the square lattice (labelled as 1 and 2) and the same distance $d_{12} \approx 172$ µm. Image area displayed in (a,b) corresponds to an effective area of 160µm × 160µm, and image area displayed in (c,d) corresponds to an effective area of $1.4\mu m^{-1} \times 1.4\mu m^{-1}$.

spatially decaying particle flux, is too weak to establish mutual coherence and hence, $g_{12} = 0$. However, an indirect link between the two condensation centres is established by creating a connected path with additional closely spaced condensates [see Fig. 6.7(b)]. The presence of condensates in the bulk of the square lattice then mediate the formation of coherence between the edge condensates with $g_{12} = 0.25$ and clearly visible interference fringes in Fig. 6.7(d).

6.4 Conclusion

The presented closed-loop feedback scheme is suitable for balancing the condensate emission intensity across optically generated networks and lattices of polariton condensates. Optical stabilisation counteracts photon-mode localisation caused by sample nonuniformities [128], reduces the effects of optical aberrations in the experimental system, and compensates non-homogeneous gain distribution in coupled condensate networks. The scheme allows generation of both, periodic and non-periodic networks

with striking homogeneity and enhanced coherence properties with examples shown in Fig. 6.8.

It is well known that dynamics and synchronisation in coupled oscillator systems is critically affected by the underlying network architecture [115]. Our results show, that a larger number of couplings in lattices of ballistically coupled condensates generally amplifies the formation of coherence across the system, and at the same time reduces the operational pump power per condensate node. Similar results (i.e. enhanced coherence properties with larger connectivity in arrays of coupled elements) have been observed in various technological platforms such as in VCSEL arrays [128], in micromechanical oscillator networks [129], and in arrays of fiber lasers [130].

Importantly, the presented methods for active mode-stabilisation qualify for other open-dissipative systems such as photon condensates and laser arrays, and therefore, lay out directions for the design of power-efficient devices of coherently coupled polaritonic or photonic lattices.

6.5 Disclaimer

Experimental studies presented in this Chapter were conducted by J. D. Töpfer, I. Chatzopoulos, and T. Cookson. Theoretical analysis was carried out by H. Sigurdsson and Y. G. Rubo, and numerical simulations were calculated by H. Sigurdsson. Figures and text description presented in this Chapter are adapted from published Reference [89].

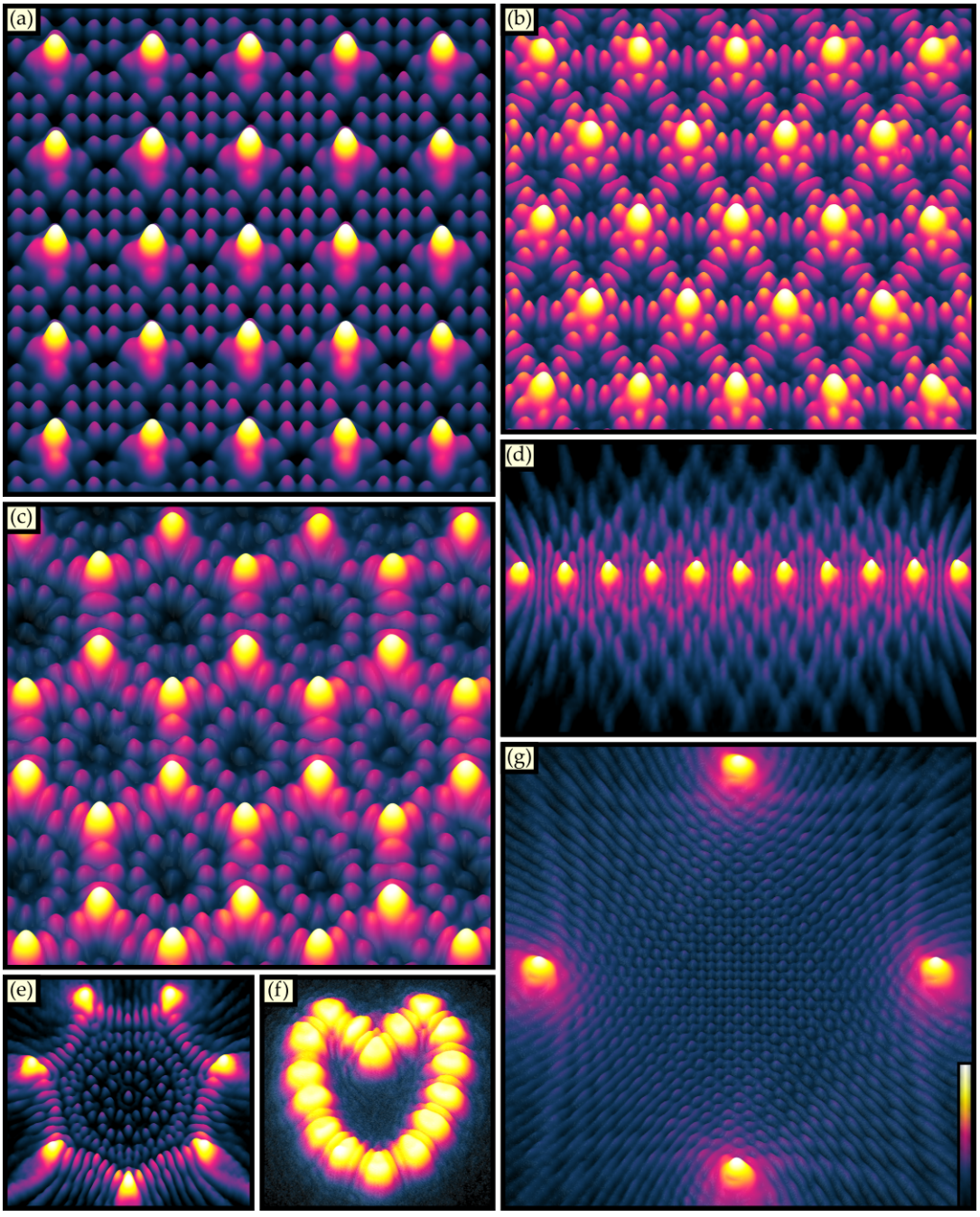

FIGURE 6.8: **Coherent networks of polariton condensates realised by active stabilisation of the condensate node densities.** Three-dimensional plots of the experimentally recorded real space emission of a stabilised (a) square lattice, (b) triangular lattice, (c) honeycomb lattice, (d) chain, (e) polygon, (f) heart structure, and a (g) square of polariton condensates. Plot elevation and false colour scale [shown in (g)] in each panel represent the condensate density on a logarithmic scale. Panels (a) and (b) are adapted from Reference [89].

Chapter 7

Optical Control Of Couplings In Networks Of Polariton Condensates

A growing interest into the study of many-body optical networks is boosted by the experimental accessibility of open-dissipative lattices such as in coupled laser systems [131], and photon [97] and polariton [89] condensates. Successful realisations of extended polaritonic systems underline the versatile potential of polariton condensates for optical processing units and circuitry [132, 133, 134], simulation of many-body spin systems [41, 135] and the study of geometric frustration [136], neuromorphic computing [39], studies on synchronisation dynamics of coupled oscillator systems [89, 121], and topological states [37, 38]. Performance of these systems depends on the accuracy of control over the couplings between individual condensate elements. Moreover, the realisation of complex device structures requires advanced engineering techniques and, ultimately flexible control over individual couplings is desired.

As we have detailed in Chapter 5 the interactions between ballistically coupled polariton condensates can readily be controlled by changing their physical in-plane separation distance d. Hereby, the change in optical path length between two condensates - alternatively interpreted as a modified time-of-flight of particle fluxes - is the decisive factor for the configuration of phase synchronised states. The methods can be extended to condensate lattices, where control over the lattice constant (i.e. NN distance) allows realisation of various synchronisation states [41]. However, individual couplings cannot be controlled in extended systems because the physical displacement of one condensate will inevitably affect all couplings associated with this condensate.

In this Chapter, we describe an all-optical and reversible technique to control individual couplings in polariton lattices by non-resonant imprinting of potential barriers (i.e. exciton reservoirs below condensation threshold) [93, 133]. Generation of a potential barrier, which is located in-between two ballistically coupled polariton condensates, modifies the effective optical path length separating the condensates (see Schematic in

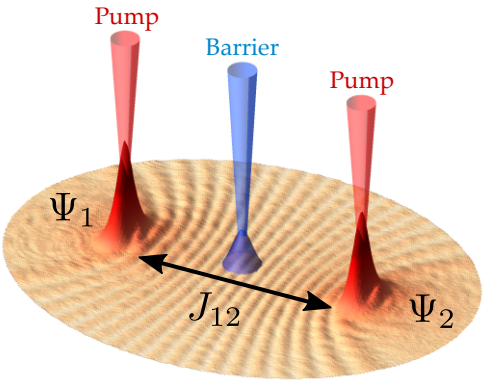

FIGURE 7.1: **Optical control over the ballistic coupling of polariton condensates.** Non-resonant imprinting of a potential barrier modulates the polariton flux in magnitude and phase in-between two ballistically coupled condensates.

Fig. 7.1). This method can readily be extended to larger and more complex systems and therefore, allows for manipulation of pairwise interactions of NNs.

In the following, we begin with a summary of the key experimental tools for generation and advanced control over coupled polariton condensates. Then, we detail on the modified flow properties of a single ballistically expanding polariton condensate, which is impinging onto an optically injected potential barrier. It is shown that the phase modulation of the polariton flux is strong enough to control the synchronised states in smaller systems of two condensates, as well as in larger 1D and 2D lattices. Spectral analysis of the coupled condensate system reveals that the system dynamics can adequately be described by a delay-coupled oscillator model with variable control over the phase of the complex coupling parameter. The results presented in this Chapter have been published in Reference [90].

7.1 Experimental methods

In-depth descriptions of the experimental techniques for generation and read-out of networks and lattices of polariton condensates are described in Chapter 4. The experimental investigations presented in the following are conducted on a strain-compensated GaAs-based microcavity (see Section 4.3) at an exciton-photon detuning $\Delta \approx -3.8$ meV. The non-resonant cw laser is split into two beams, modulated by two separate SLMs, and recombined to form a digitally-controllable and reconfigurable excitation geometry (see Fig. 4.1). One of the modulated laser beams forms the pump geometry of ballistically expanding condensates, i.e. each of the nodes of this laser beam are pumped above condensation threshold. The second laser beam however, injects a spatial pattern of localised incoherent exciton reservoirs below condensation threshold. Density-stabilisation of both, the condensate networks and the laser-induced potential barriers is possible via the closed-loop feedback technique described in Section 4.2.2.

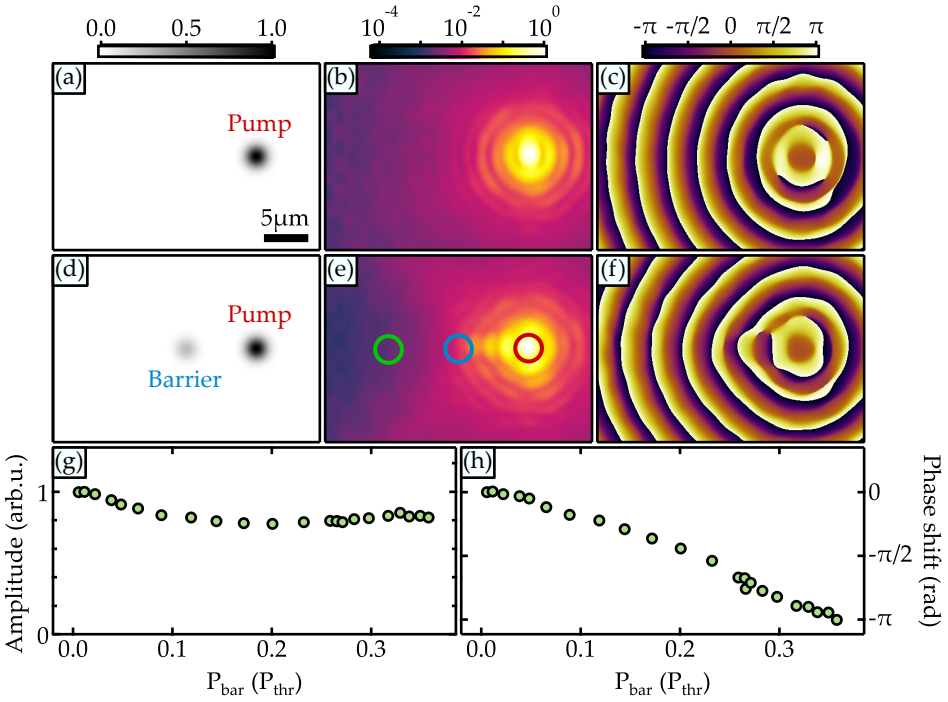

FIGURE 7.2: **Modulation of a ballistically expanding condensate subject to an optically injected potential barrier.** (a,d) Real space laser pump profile, (b,e) recorded real space PL, and (c,f) reconstructed phase map of a ballistically expanding condensate (a-c) without and (d-f) with potential barrier. The barrier is displaced from the condensate node by $d/2 \approx 7.9$ μm, and is pumped below threshold $P_{\text{bar}} \approx 0.36P_{\text{thr}}$. Condensate pump spot and potential barrier locations are shown as red and blue circles in (e), respectively. Extracted (g) magnitude and (h) phase shift of the condensate wave function at a distance $d \approx 15.7$ μm away from the condensate node [green circle in (e)]. The Figure is adapted from Reference [90].

7.2 Optically-induced potential barriers for polaritons

Previous studies have detailed on the use of optically imprinted potential barriers in microcavities for control of particle flows in polariton transistors [137], polariton interferometers [133], and for generation of artificial defects [138]. In this section we describe the effects of a non-resonantly generated potential barrier onto the flow properties of a single ballistically expanding polariton condensate, which is summarised in Fig. 7.2. Detailed characteristics of a radially expanding condensate without any potential barrier were presented in Fig. 5.2. Here, we only show the recorded real space condensate density [Fig. 7.2(b)] and the extracted condensate phase distribution [Fig. 7.2(c)] for a single condensate node pumped above condensation threshold ($P = 1.3P_{\text{thr}}$). The visible radial phase gradient is innately linked to an isotropic radial condensate expansion with non-zero outflow wave vector $k_c = 1.9$ μm^{-1}.

The impact of a non-resonantly injected barrier onto density and phase distribution of the radially expanding condensate node are shown in Fig. 7.2(e) and Fig. 7.2(f), respectively. The barrier is displaced from the condensate centre by a distance $d/2 \approx 7.9$ μm and is pumped below condensation threshold with pump power $P = 0.36P_{\text{thr}}$. It is

apparent that the incoherent exciton reservoir, which is generated at the barrier laser spot location, indeed acts as a potential barrier and leads to scattering of the incoming coherent particle flux. In particular, there is a noticeable shadow (i.e. reduced density) forming behind the barrier, and the condensate phase is shifted by the presence of the barrier. In the linear regime the repulsive barrier potential $V(\mathbf{x})$ [see Eq. 5.1] felt by polaritons leads to a local blue-shift and is proportional to the locally generated exciton population, i.e. $V(\mathbf{x}) = g_R n(\mathbf{x})$.

To quantify the impact of the barrier onto the condensate flow properties we measure both, density and phase of the 'transmitted' condensate wave function at a distance $d/2 \approx 7.9$ µm behind the barrier location [see green circle in Fig. 7.2(e)]. The extracted change in magnitude $|\Psi|$ and phase $\arg(\Psi)$ of the condensate for increasing barrier pump power P_{bar} are shown in Fig. 7.2(g) and Fig. 7.2(h), respectively. We note that there is only a minor change in the amplitude of the transmitted condensate wave due to an interplay of repulsion and gain provided by the localised incoherent exciton reservoir. The transmitted condensate amplitude does not drop below ≈ 77 % of the amplitude of a freely expanding condensate (i.e. no barrier) in the given range of barrier pump powers $P_{\text{bar}} \leq 0.36 P_{\text{thr}}$. Within this limited power range there is negligible PL originating from the barrier itself, and within the experimental resolution there is no discernable change in emission energy of the ballistic condensate node. Consequently, the barrier can be seen as a weak perturbation to the ballistically expanding condensate, with negligible back-action (reflection) onto the condensation centre. Nevertheless, a large impact of the potential barrier onto the condensate flow dynamics can be seen by the near-linear phase shift Δ_ϕ of the transmitted particle wave [see Fig. 7.2(h)] reaching $\Delta_\phi = -\pi$ for a barrier pump power $P_{\text{bar}} = 0.36 P_{\text{thr}}$.

By approximating the barrier as a square-shaped repulsive potential of width L and height V_0, the phase shift Δ_ϕ of the transmitted particle wave with wave number k and particle mass m can be written as

$$\Delta_\phi = -kL \left(1 - \sqrt{1 - \frac{2mV_0}{\hbar^2 k^2}} \right). \tag{7.1}$$

Since for small barrier pump powers $P_{\text{bar}} \ll P_{\text{thr}}$ one expects a small potential V_0 that grows approximately linear with pump power, from Eq. 7.1 indeed follows a linearly decreasing phase shift Δ_ϕ with increasing power P_{bar}.

We note that - within the accuracy of the experimental system - there is no notable difference in the particle flow properties opposite to the direction of the potential barrier, qualifying the method for directional control of particle flows in extended networks or lattices. The observed changes in optical path length up to $\Delta_\phi = -\pi$ further prompt the idea of using an optically imprinted barrier to manipulate the phase locking of ballistically coupled polariton condensates.

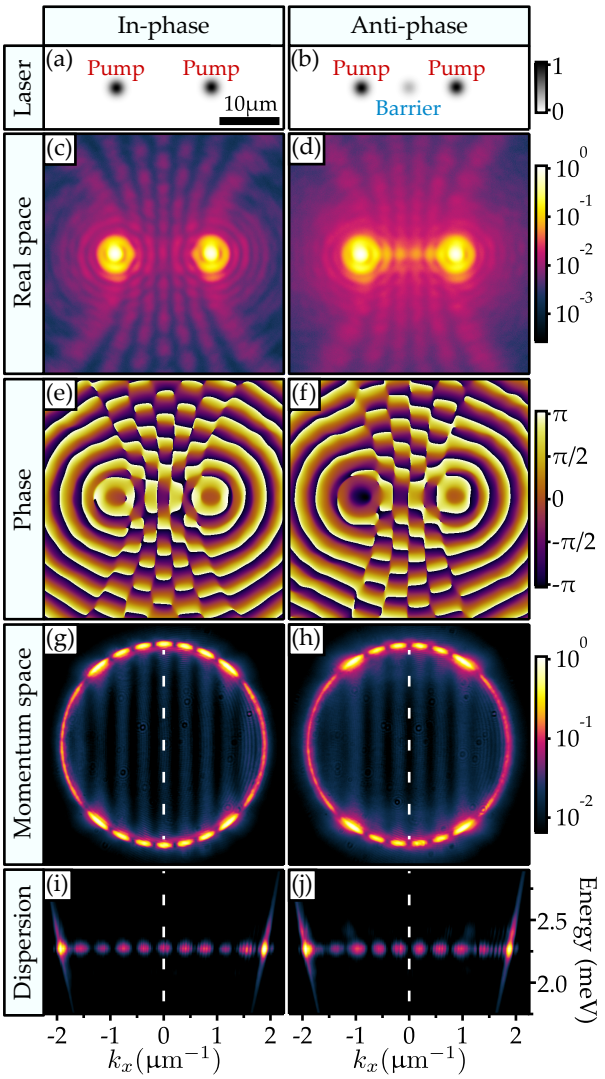

FIGURE 7.3: **Optical control of couplings between two polariton condensates.** Real space (a,b) laser pump profile, (c,d) condensate density, and (e,f) phase distribution for two condensates (a,c,e) without and (b,d,h) with additional potential barrier ($P_{\text{bar}} = 0.36P_{\text{thr}}$). Corresponding (g,h) momentum space and (i,j) dispersion images reveal an even or odd parity state by showing a bright or dark interference fringe at $k_x = 0$ (white dashed line). Energy is scaled with respect to the ground state of the lower polariton branch. The Figure is adapted from Reference [90].

7.3 Control of couplings between two condensates

In the following we detail on the implementation of an optically induced potential barrier to control the synchronous phases in a polariton dyad. The experimental conditions in the two-condensate systems are equivalent to those of the single condensate system described in the previous Section: Each condensate node is pumped at $P = 1.3\ P_{\text{thr}}$, the condensate separation distance is chosen as $d \approx 15.7$ μm, and the barrier is imprinted at the geometrical centre of the system at a distance $d/2 \approx 7.9$ μm from each condensate. Hence, the phase shifts Δ_ϕ determined for an expanding condensate [see Fig. 7.2(h)] are transferable to the description of particle flows across the polariton dyad.

The particular polariton dyad configuration without any potential barrier [$P_{\text{bar}} = 0$, Fig. 7.3(a)] results in a synchronised state with zero phase difference between the two condensate nodes. The condensate emission is probed by density measurements in real space [Fig. 7.3(c)], in momentum space [Fig. 7.3(g)], and in energy-resolved momentum space [Fig. 7.3(i)] revealing macroscopic occupation of a single quantum state. The measured real space phase distribution [Fig. 7.3(e)] exposes the even parity mode characteristics and the vanishing condensate centres phase difference $\theta_{12} = 0$.

Optical injection of a potential barrier [$P_{\text{bar}} = 0.36P_{\text{thr}}$, Fig. 7.3(b)] via non-resonant generation of a localised exciton reservoir in-between the two condensate nodes then leads to a transition of their synchronised state. Real space and momentum space PL measurements [shown in Figs. 7.3(d,f,h,j)]] indicate single-mode emission of an odd-parity state, i.e. phase-locking of the two condensation centres with stable phase difference $\theta_{12} = \pi$. The observed in-phase to anti-phase synchronisation transition can readily be explained by the generated optical path difference $\Delta_\phi = -\pi$ leading to a change in the system's resonance condition. It is analogous to the previously described synchronisation transitions in Chapter 5, but does not require a change in condensate separation distance d. We note that the observed mode transition, which is realised by the generation of a potential barrier between the condensates, can equivalently be obtained by a decrease of the condensate separation distance by $\Delta_d \approx \pi/k_c$.

Importantly, within the system's emission linewidth ($\Delta_E \approx 70$ μeV) there is no notable difference in energy between the two stationary systems with and without potential barrier, respectively. This is in line with the small modifications of the amplitude of transmitted particle waves [see Fig. 7.2(g)] and therefore, implies that the barrier has a small impact onto the coupling strength between the condensates only.

The continuous transition of the two coupled condensate system from in-phase to anti-phase synchronised states is shown in Fig. 7.4(a), where we plot the recorded energy spectral densities for increasing barrier pump power P_{bar}. It is apparent that the transition is interleaved by a region involving macroscopic occupation of two resonant modes and thus, involves periodic population oscillations between the two condensation centres. The transitions between stationary and non-stationary dynamical behaviour of two ballistically coupled condensates has been described in Section 5.3.3 and can be reproduced by a time-delayed coupled oscillator model [see Section 5.5]. It is straightforward to adjust the coupled oscillator equations [Eqs. 5.19] in order to include the investigated potential barriers for control over couplings.

7.3.1 Coupled oscillator model

The coupled oscillator model presented in Section 5.5 describes the state of each condensate by a complex-valued amplitude $c_i(t)$ and includes coupling of each condensate

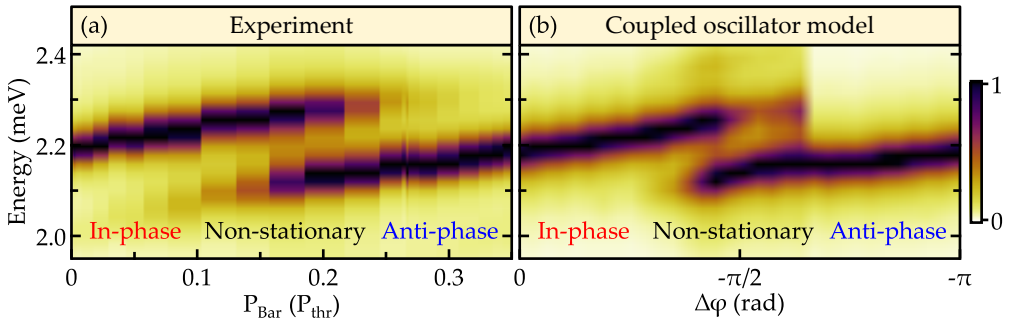

FIGURE 7.4: **Optically controlled synchronous phase of two ballistically coupled polariton condensates.** (a) Experimentally recorded spectra of two condensates with increasing barrier pump power P_{bar}. (b) Numerically calculated spectra of two coupled nonlinear oscillators [see Eq. 7.2] as a function of phase lag Δ_ϕ. The numerical spectra are convoluted with a Lorentzian profile to match the experimental linewidth. Energy is scaled with respect to the ground state of the lower polariton branch. Numerical parameters: $\hbar\Omega = 1.45$ meV, $\hbar\Gamma = 0.5$ meV, $\hbar g = 0.5$ μeV, $\hbar R = 0.5$ μeV, $\hbar\alpha = 0.1$ μeV, $\hbar J = 0.15$ meV, $\beta = -0.8$ rad, $\tau = 12.1$ ps, $\Gamma_A = 0.05$ ps^{-1}, and $P = 100$ ps^{-1} . The Figure is adapted from Reference [90].

with its underlying exciton reservoir $n_i(t)$. Time-delayed interactions between spatially separated condensates depend on the inter-element particle currents, and are described by a complex-valued coupling term $J\exp(i\beta)$. Small modifications of the effective optical path length Δ_ϕ between ballistically coupled condensates, e.g. due to a weak potential barrier, cause a change in coupling phase, i.e. $\beta \to \beta + \Delta_\phi$. Ultimately, a π phase shift of the coupling phase reverses the sign of the effective coupling term leading to the observed change in synchronisation between two condensates. We note that such a coupling phase lag can equivalently be described by a small time-delay [139].

The coupled condensate equations including variable coupling phases then read as

$$i\dot{c}_i(t) = \left[\Omega - i\Gamma + \left(g + \frac{iR}{2}\right) n_i(t) + \alpha|c_i(t)|^2\right] c_i(t) + Je^{i\beta}e^{i\Delta_\phi}c_j(t-\tau), \tag{7.2a}$$

$$\dot{n}_i(t) = -\left(\Gamma_A + R|c_i(t)|^2\right) n_i(t) + P. \tag{7.2b}$$

The experimentally observed transition of the two-condensate system from an in-phase to anti-phase state is well reproduced by numerical integration of Eqs. 7.2. Spectral densities of the simulated condensate oscillators are shown in Fig. 7.4(b), where an increasing barrier pump power $P_{\text{bar}} = 0 \ldots 0.36 P_{\text{thr}}$ is represented by a decreasing phase shift $\Delta_\phi = 0 \ldots -\pi$. The numerical results have been convoluted with a Lorentzian profile in order to match the experimental linewidth. The calculated spectra reveal both, stationary (synchronised) states and non-stationary (periodic) states, in good agreement with the experimentally observed dynamical regimes.

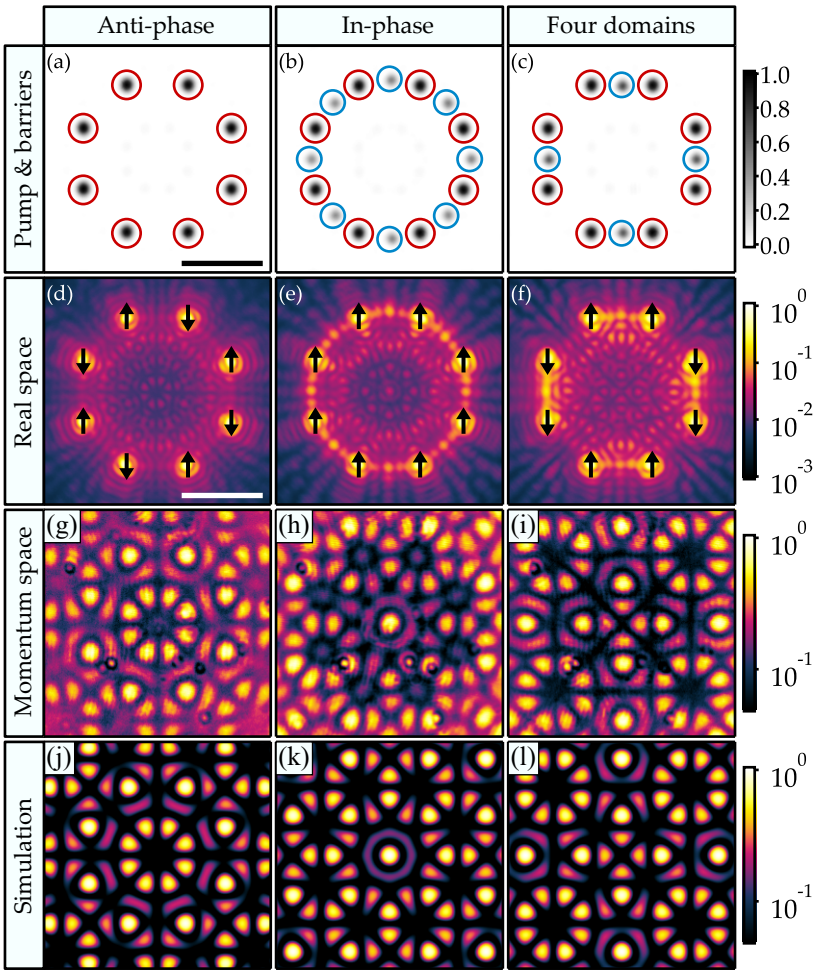

FIGURE 7.5: **Optical control of couplings in a polygon of polariton condensates.** (a-c) Laser pump profile, (d-f) real space condensate density, and (g-i) momentum space condensate density for three different synchronisation states realised by individual control of NN couplings via optically imprinted potential barriers. (j-l) Simulated far-field emission pattern for fully-coherent point sources with the same spatial geometry and phase distribution as in experiment. Red and blue circles in (a-c) mark the position of condensate pump and barrier pump spots, respectively. Black arrows in (d-e) depict the phase-locked polygon configuration. Scale bars shown in (a) and (d) amount for 20 μm. and 1 μm^{-1}. Images (g-l) show the central 1 $\mu m^{-1} \times 1\ \mu m^{-1}$ emission area.

7.4 Synchronisation control in polariton lattices

Optical control over the ballistic flow of polaritons via engineering of a repulsive potential landscape can be applied to larger coupled condensate geometries, and enables flexible control over the NN interactions in lattices of polariton condensates. A proof of concept is presented in the following, where we show experimental results on the synchronisation control in 1D and 2D lattices of polariton condensates.

7.4.1 A one-dimensional lattice

A 1D lattice with periodic boundary conditions is realised by non-resonant optical excitation of 8 polariton condensates arranged in a polygon structure (octagon). The recorded laser pump profile and condensate real space density map are illustrated in Figs. 7.5(a) and (d), respectively. The condensate NN separation distance (lattice constant) is chosen as $a \approx 15.2$ μm, and renders a stable coherent state with anti-phase synchronisation between NNs. While an even number of nodes within the polygon can yield a stable anti-phase configuration, geometric frustration prevents the formation of such a state in odd-numbered polygons and leads to the formation of vortex states instead [136]. The stable octagon phase configuration is indicated in Fig. 7.5(d) using black pseudo-spins for each condensate node, with anti-parallel spins denoting anti-phase configurations, and parallel spins resembling in-phase configurations. Destructive interference of all emitted matter waves leads to the visible density minimum at the system's centre of symmetry.

The octagon of polariton condensates is then modified by introducing additional potential barriers ($P_{\text{bar}} < P_{\text{thr}}$) located either in-between each pair of NNs [Fig. 7.5(b)], or in-between every second pair of NNs [Fig. 7.5(c)]. While in the former case the change in couplings leads to synchronisation of condensates with zero phase differences [see Fig. 7.5(e)], in the latter case the system transitions into a stable configuration with 4 synchronised 'domains' [see Fig. 7.5(f)]. A bright interference peak emerges at the system's centre of symmetry in case of the in-phase synchronised octagon [Fig. 7.5(e)] due to constructive interference of all expanding condensates. The splitting of the clustered polygon structure [Fig. 7.5(f)] causes the formation of 2 intersecting nodal lines dividing the condensate density into 4 synchronised regions. The phase transitions are reproducible by numerical simulations of the GPE [Eq. 3.27] and the coupled oscillator model [Eq. 7.2], and emerge due to alterations of the pairwise interactions between NN condensates.

Coherence and phase configuration of the coupled condensate system are further probed by far field (momentum space) density measurements of the condensate PL as shown in Fig. 7.5(g-i). One can see that the recorded intricate far field PL patterns strongly depend on the symmetry of the synchronisation state. We point out the reduced (4-fold) rotational symmetry in the recorded far field emission pattern of the clustered octagon structure, as opposed to the 8-fold rotational symmetry for the anti-phase and in-phase condensate structures. We recall that the far field intensity pattern $\hat{I}(\mathbf{k})$ is formed by the interference of all condensates and thus, is innately linked to the systems coherence properties [see Eq. 3.37]. There is excellent agreement between the measured far field emission and the numerically calculated emission patterns of fully-coherent octagons as depicted in Figs. 7.5(g-l).

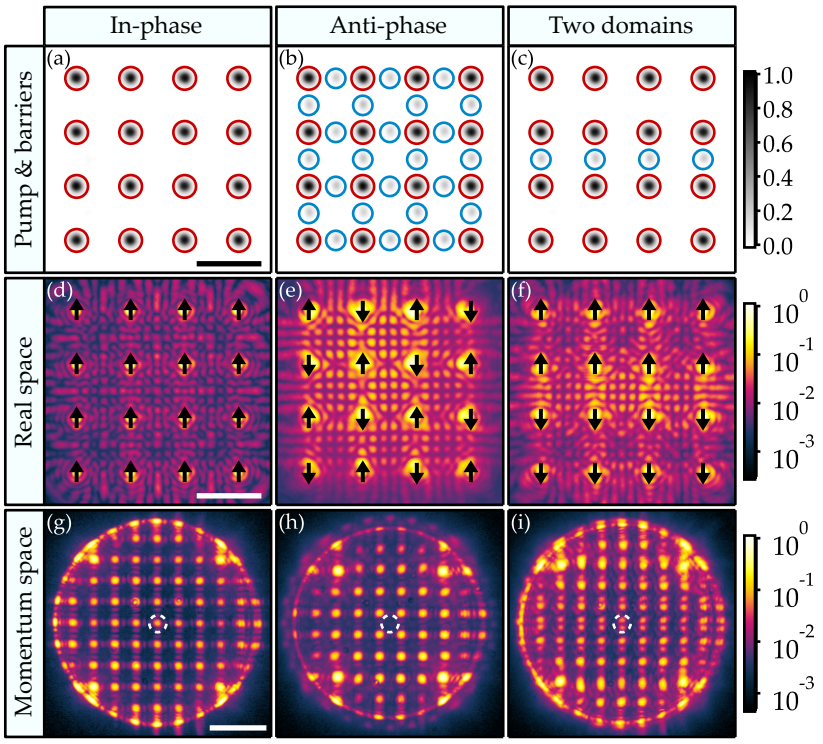

FIGURE 7.6: **Optical control of couplings in a polariton square lattice.** (a-c) Laser pump profile, (d-f) real space condensate density, and (g-i) momentum space condensate density for three different synchronisation states realised by individual control of NN couplings via optically imprinted potential barriers. Red and blue circles in (a-c) mark the position of condensate pump and barrier pump spots, respectively. Black arrows in (d-e) depict the phase-locked lattice configuration. White dashed circles in (g-i) indicate the centre of origin $\mathbf{k} = 0$. Scale bars shown in (a,d), and (g) amount for 20 μm and 1 μm^{-1}, respectively. The Figure is adapted from Reference [90].

7.4.2 A two-dimensional lattice

Optical control over the NN interactions in a 2D polariton lattice is demonstrated for a 4×4 square lattice with lattice constant $a \approx 16.6$ μm. Figure 7.6(d) depicts the recorded real space PL of the system condensing into a state with all condensates synchronised in-phase. Macroscopic coherence is revealed by the appearance of periodic interference peaks in the far field as shown in Fig. 7.6(g). The spacing between neighbouring interference peaks is matching the reciprocal lattice constant $2\pi/a$. The particular synchronisation state, which is described by zero phase differences between individual condensates, leads to the appearance of a distinct bright 'Bragg' peak located at the origin $\mathbf{k} = 0$.

Inversion of all NN interactions is then realised by implementation of potential barriers ($P_{\text{bar}} < P_{\text{thr}}$) between every pair of neighbouring condensates [see pump profile in Fig. 7.6(b)]. The induced change in pairwise interactions causes a transition into a coherent state described by anti-phase synchronisation between NN as illustrated in Fig. 7.6(e). The phase configuration is characterised by a lateral shift of the reciprocal lattice [see Fig. 7.6(h)] and produces a density minimum at the origin $\mathbf{k} = 0$. Similar

transitioning between in-phase and anti-phase synchronisation states in a square lattices of polariton condensates has been demonstrated in Reference [41] by tuning of the lattice constant a.

A more complex lattice synchronisation state is implemented by adding only 4 potential barriers into the system as illustrated in Fig. 7.6(c). The barrier-induced changes in couplings along one horizontal line can be seen as an effective 'line defect' within the square lattice. Indeed, the recorded real space PL shown in Fig. 7.6(f) reveals the formation of 2 synchronised domains that appear out-of-phase with respect to each other. It is important to note that although the two domains are out-of-phase, they are still coherent, i.e. their phase relationship is a dynamically stable solution. The splitting into two coherent domains is further evidenced by a distinct vertical splitting of the interference Bragg peaks in momentum space as shown in Fig. 7.6(i). This particular synchronisation state can alternatively be realised by local compression of the lattice constant along the described horizontal line.

7.5 Conclusion

Control over coupling phases has been shown to be a crucial parameter for generation of synchrony in general networks of nonlinear oscillators [140, 141]. Here, we have successfully demonstrated an experimental strategy for tuning of coupling phases in networks and lattices of coupled polariton condensates. The technique harnesses optical control over the inter-element particle flows in microcavities, and facilitates flexible, adjustable, and reversible generation of complex network architectures. Various synchronised states of ballistic polariton condensates were realised by engineering of coupling topologies in 1D and 2D periodic structures.

Optical tuning of couplings in networks and lattices of polariton condensates potentially advances current strategies of designing systems for analogue simulation of spin-Hamiltonians [41], novel neuro-inspired computing schemes [39], or for the generation of topological states [37, 40]. In a broader application scheme it opens up an ultrafast platform for the study of synchronisation dynamics in nonlinear oscillator networks with malleable properties of coupled elements and network architectures.

7.6 Disclaimer

Experimental studies presented in this Chapter were conducted by S. Alyatkin, J. D. Töpfer, and A. Askitopoulos. Numerical simulations were carried out by H. Sigurdsson. Figures and text description presented in this Chapter are adapted from published References [90].

Chapter 8

Concluding Remarks And Future Perspectives

The hybrid nature of exciton-polaritons makes microcavities an interesting and interdisciplinary platform combining both photonics and solid state physics onto a micro- to millimetre device scale. Particle properties are tunable and characterised by a small effective mass, strong nonlinearities, short particle lifetimes, and a non-parabolic dispersion relation. Most notably, polaritons are excellent candidates for the study of macroscopically occupied single quantum states (condensates) at elevated temperatures. The intrinsic driven-dissipative nature and low-dimensional confinement of polariton condensates separates them from conventional BECs and superfluids, opening an interesting window for the study of non-equilibrium quantum fluids and non-Hermitian physics [11].

Optical malleability of the underlying non-Hermitian potential landscape offer a versatile method for the manipulation of polariton condensates [142], with wide-ranging applications such as trapping of polariton condensates [143], sculpting of oscillators [34], generation of non-equilibrium spin lattices [135], polariton circuitry [133], creation of arrays of artificial two-level systems [144], and band-structure engineering [40]. Moreover, the ease of generation and spatial structuring of polariton condensates has led to recent developments of lattices of coupled polariton condensates for the realisation of analogue simulators [41], topological devices [37, 38], and computational machines [39]. In a more general context, networks of coupled polariton condensates may represent a paradigmatic platform for the realisation and study of coupled nonlinear oscillator systems [43] with realisations in trapping geometries [121], as freely-expanding condensate nodes [89], and as oscillatory units [144].

Key results

Optical control over the spatial structure and potential landscape in networks of polariton condensates is at the heart of the studies conducted in this thesis. **Advancements in design and manipulation of optically generated polariton lattices** presented throughout this thesis were key for the experimental results obtained. The most important tool introduced for the conducted work is the **active density stabilisation method** for laser and condensate structures as described in Sections 4.2.2 and 6.2 of this thesis.

In Chaper 5 the **dynamics and synchronisation of ballistically expanding polariton condensates** was studied. Increasing the separation distance between two symmetrically pumped condensates was shown to periodically alter the system dynamics between **in-phase and anti-phase synchronisation regimes**, with additionally appearing **non-stationary periodic solutions**. These non-stationary states resemble picosecond-timescale **population oscillations** between both condensation centres, and have been probed via auto- and cross correlation measurements. In contrast to the low-dimensional state space of two tunneling-coupled condensates [111], the ballistically coupled system is described by an infinite amount of coupled modes. It was shown, that the system dynamics is well described by a **delay-coupled oscillator model** accounting for the ballistic flow of particles between the condensates.

Non-resonant optical excitation and characterisation of different 1D and 2D periodic structures of polariton condensates was described in Chapter 6. It was shown that the closed-loop density stabilisation method reduces the detrimental effects of sample non-uniformities and optical aberrations onto the system's spatial coherence properties, allowing for the **generation of macroscopically coherent polariton lattices** with **near-diffraction limited emission**. The advanced optical engineering of **homogeneous polariton lattices** further made it possible to accurately study the **spatial coherence properties** on the system's network architecture. It was shown that an increasing number of coupling both, increases the system's spatial coherence properties, and reduces the operational pump power per condensate node. The developed methods for generation and spatial characterisation of polariton lattices are not limited to the field of microcavity polaritons, but are transferable to other open-dissipative systems such as photon condensates, and coupled lasers.

In Chapter 7 the engineering of ballistically coupled polariton lattices was advanced by the introduction of an additional **optically imprinted potential landscape**. It was shown that the local injection of tunable potential barriers in-between ballistically coupled polariton condensates facilitates an additional degree of freedom for experimental **control of individual couplings in polariton lattices**. In particular, it was demonstrated experimentally that **optically tunable coupling phases** give flexible control over system dynamics and synchronisation in two-condensate systems, as well as in larger 1D and 2D condensate lattices.

Future perspectives

The methods and results presented in this work lay out interesting directions for future research in open-dissipative network structures. With advanced precision in generation and optical tunability of artificial lattices it is possible to explore the rich physics and complicated dynamics of non-Hermitian many-body systems. Moreover, ballistic polariton condensates represent a malleable experimental platform for the study of coupled oscillator networks with tunable elements, adjustable time-delays and optically controllable coupling phases. The advancements in sample fabrication [76], and the possibilities of macroscopic particle propagation lengths [145] and long-range couplings [78] point out the future potential of extended systems containing 1000*s* of coupled condensates.

While this work has mainly focused on the generation of homogeneous and highly-coherent (synchronised) lattice structures, it is also possible to apply its methods for the generation of inhomogeneities (i.e. controllable defects) and explore the occurring system dynamics. Furthermore, it is of interest to investigate desynchronised and partially-synchronised configurations, potentially exhibiting complex phenomena such as chimera states, cluster synchronisation, chaotic dynamics, and the cross-over between synchronised and desynchronised regimes [121]. Although not explored yet, time-resolved measurements of spatial coherence in polariton lattices can give interesting insights into the build-up of correlations in many-body system, and reveal the temporal formation of synchronisation in spatially extended systems.

Advancements in optical shaping of potential landscapes can be further explored for extended control of condensate structures and particle flows. Hereby, the non-Hermitian nature of polaritons facilitates spatial patterning of both, the repulsive potential and gain distribution within the microcavity plane. All-optical design of complex geometries such as in-plane waveguides, resonators, and logic gates therefore, might offer promising applications in future polariton microprocessors and circuitry [146].

References

[1] Steven H Strogatz, *Nonlinear dynamics and chaos: With applications to physics, biology, chemistry, and engineering* (CRC Press, 2014).

[2] Fatihcan M Atay, *Complex Time-Delay Systems: Theory and Applications* (Springer-Verlag, Berlin Heidelberg, 2010).

[3] Richard P Feynman, Simulating physics with computers, Int. J. Theor. Phys **21**, 467–488 (1982).

[4] Susanna C Manrubia, Alexander S Mikhailov, and Damián H Zanette, *Emergence of dynamical order: Synchronization phenomena in complex systems* (World Scientific, Singapore, 2004).

[5] Arkady Pikovsky, Jurgen Kurths, Michael Rosenblum, and Jürgen Kurths, *Synchronization: a universal concept in nonlinear sciences*, Vol. 12 (Cambridge University Press, 2003).

[6] Pyotr Kapitza, Viscosity of liquid helium below the λ-point, Nature **141**, 74 (1938).

[7] John F Allen and AD Misener, Flow of liquid helium II, Nature **141**, 75 (1938).

[8] J George Bednorz and K Alex Müller, Possible high T_c superconductivity in the Ba-La-Cu-O system, Zeitschrift für Physik B Condensed Matter **64**, 189–193 (1986).

[9] Mike H Anderson, Jason R Ensher, Michael R Matthews, Carl E Wieman, and Eric A Cornell, Observation of Bose-Einstein condensation in a dilute atomic vapor, Science **269**, 198–201 (1995).

[10] K. B. Davis, M. O. Mewes, M. R. Andrews, N. J. van Druten, D. S. Durfee, D. M. Kurn, and W. Ketterle, Bose-Einstein condensation in a gas of sodium atoms, Phys. Rev. Lett. **75**, 3969–3973 (1995).

[11] Tim Byrnes, Na Young Kim, and Yoshihisa Yamamoto, Exciton–polariton condensates, Nature Physics **10**, 803–813 (2014).

[12] C. Weisbuch, M. Nishioka, A. Ishikawa, and Y. Arakawa, Observation of the coupled exciton-photon mode splitting in a semiconductor quantum microcavity, Phys. Rev. Lett. **69**, 3314–3317 (1992).

[13] Alexey Kavokin, Jeremy J Baumberg, Guillaume Malpuech, and Fabrice P Laussy, *Microcavities* (Oxford university press, Oxford, 2017).

[14] Hui Deng, Gregor Weihs, Charles Santori, Jacqueline Bloch, and Yoshihisa Yamamoto, Condensation of semiconductor microcavity exciton polaritons, Science **298**, 199–202 (2002).

[15] Jacek Kasprzak, M Richard, S Kundermann, A Baas, P Jeambrun, Jonathan Mark James Keeling, FM Marchetti, MH Szymańska, R André, JL Staehli, *et al.*, Bose-Einstein condensation of exciton polaritons, Nature **443**, 409–414 (2006).

[16] A. Imamoğlu, R. J. Ram, S. Pau, and Y. Yamamoto, Nonequilibrium condensates and lasers without inversion: Exciton-polariton lasers, Phys. Rev. A **53**, 4250–4253 (1996).

[17] Daniele Sanvitto and Stéphane Kéna-Cohen, The road towards polaritonic devices, Nature Materials **15**, 1061–1073 (2016).

[18] Christian Schneider, Arash Rahimi-Iman, Na Young Kim, Julian Fischer, Ivan G Savenko, Matthias Amthor, Matthias Lermer, Adriana Wolf, Lukas Worschech, Vladimir D Kulakovskii, *et al.*, An electrically pumped polariton laser, Nature **497**, 348–352 (2013).

[19] S. Christopoulos, G. Baldassarri Höger von Högersthal, A. J. D. Grundy, P. G. Lagoudakis, A. V. Kavokin, J. J. Baumberg, G. Christmann, R. Butté, E. Feltin, J.-F. Carlin, and N. Grandjean, Room-temperature polariton lasing in semiconductor microcavities, Phys. Rev. Lett. **98**, 126405 (2007).

[20] J. J. Baumberg, A. V. Kavokin, S. Christopoulos, A. J. D. Grundy, R. Butté, G. Christmann, D. D. Solnyshkov, G. Malpuech, G. Baldassarri Höger von Högersthal, E. Feltin, J.-F. Carlin, and N. Grandjean, Spontaneous polarization buildup in a room-temperature polariton laser, Phys. Rev. Lett. **101**, 136409 (2008).

[21] S Kéna-Cohen and SR Forrest, Room-temperature polariton lasing in an organic single-crystal microcavity, Nature Photonics **4**, 371 (2010).

[22] Johannes D Plumhof, Thilo Stöferle, Lijian Mai, Ullrich Scherf, and Rainer F Mahrt, Room-temperature Bose-Einstein condensation of cavity exciton-polaritons in a polymer, Nature Materials **13**, 247–252 (2014).

[23] Alberto Amo, Jérôme Lefrère, Simon Pigeon, Claire Adrados, Cristiano Ciuti, Iacopo Carusotto, Romuald Houdré, Elisabeth Giacobino, and Alberto Bramati, Superfluidity of polaritons in semiconductor microcavities, Nature Physics **5**, 805–810 (2009).

[24] Konstantinos G Lagoudakis, Michiel Wouters, Maxime Richard, Augustin Baas, Iacopo Carusotto, Regis André, Le Si Dang, and B Deveaud-Plédran, Quantized vortices in an exciton–polariton condensate, Nature Physics **4**, 706–710 (2008).

[25] M Sich, DN Krizhanovskii, MS Skolnick, Andriy V Gorbach, Robin Hartley, Dmitry V Skryabin, EA Cerda-Méndez, K Biermann, R Hey, and PV Santos, Observation of bright polariton solitons in a semiconductor microcavity, Nature Photonics **6**, 50–55 (2012).

[26] K. G. Lagoudakis, B. Pietka, M. Wouters, R. André, and B. Deveaud-Plédran, Coherent oscillations in an exciton-polariton josephson junction, Phys. Rev. Lett. **105**, 120403 (2010).

[27] M Abbarchi, A Amo, VG Sala, DD Solnyshkov, H Flayac, L Ferrier, I Sagnes, E Galopin, A Lemaître, G Malpuech, *et al.*, Macroscopic quantum self-trapping and josephson oscillations of exciton polaritons, Nature Physics **9**, 275–279 (2013).

[28] Markus Greiner, Olaf Mandel, Tilman Esslinger, Theodor W Hänsch, and Immanuel Bloch, Quantum phase transition from a superfluid to a Mott insulator in a gas of ultracold atoms, Nature **415**, 39–44 (2002).

[29] Iulia Buluta and Franco Nori, Quantum simulators, Science **326**, 108–111 (2009).

[30] Immanuel Bloch, Jean Dalibard, and Sylvain Nascimbene, Quantum simulations with ultracold quantum gases, Nature Physics **8**, 267–276 (2012).

[31] CW Lai, NY Kim, S Utsunomiya, G Roumpos, H Deng, MD Fraser, T Byrnes, P Recher, N Kumada, T Fujisawa, *et al.*, Coherent zero-state and π-state in an exciton–polariton condensate array, Nature **450**, 529–532 (2007).

[32] T. Jacqmin, I. Carusotto, I. Sagnes, M. Abbarchi, D. D. Solnyshkov, G. Malpuech, E. Galopin, A. Lemaître, J. Bloch, and A. Amo, Direct observation of dirac cones and a flatband in a honeycomb lattice for polaritons, Phys. Rev. Lett. **112**, 116402 (2014).

[33] G Tosi, G Christmann, NG Berloff, P Tsotsis, Tingge Gao, Z Hatzopoulos, PG Savvidis, and JJ Baumberg, Geometrically locked vortex lattices in semiconductor quantum fluids, Nature Communications **3**, 1243 (2012).

[34] G Tosi, G Christmann, NG Berloff, P Tsotsis, T Gao, Z Hatzopoulos, PG Savvidis, and JJ Baumberg, Sculpting oscillators with light within a nonlinear quantum fluid, Nature Physics **8**, 190–194 (2012).

[35] P. Cristofolini, A. Dreismann, G. Christmann, G. Franchetti, N. G. Berloff, P. Tsotsis, Z. Hatzopoulos, P. G. Savvidis, and J. J. Baumberg, Optical superfluid phase transitions and trapping of polariton condensates, Phys. Rev. Lett. **110**, 186403 (2013).

[36] Na Young Kim, Kenichiro Kusudo, Congjun Wu, Naoyuki Masumoto, Andreas Löffler, Sven Höfling, Norio Kumada, Lukas Worschech, Alfred Forchel, and Yoshihisa Yamamoto, Dynamical d-wave condensation of exciton–polaritons in a two-dimensional square-lattice potential, Nature Physics **7**, 681–686 (2011).

[37] P St-Jean, V Goblot, E Galopin, A Lemaître, T Ozawa, L Le Gratiet, I Sagnes, J Bloch, and A Amo, Lasing in topological edge states of a one-dimensional lattice, Nature Photonics **11**, 651–656 (2017).

[38] S Klembt, TH Harder, OA Egorov, K Winkler, R Ge, MA Bandres, M Emmerling, L Worschech, TCH Liew, M Segev, *et al.*, Exciton-polariton topological insulator, Nature **562**, 552–556 (2018).

[39] Dario Ballarini, Antonio Gianfrate, Riccardo Panico, Andrzej Opala, Sanjib Ghosh, Lorenzo Dominici, Vincenzo Ardizzone, Milena De Giorgi, Giovanni Lerario, Giuseppe Gigli, *et al.*, Polaritonic neuromorphic computing outperforms linear classifiers, Nano Letters **20**, 3506–3512 (2020).

[40] Lucy Pickup, Helgi Sigurdsson, Janne Ruostekoski, and Pavlos G Lagoudakis, Synthetic band-structure engineering in polariton crystals with non-hermitian topological phases, Nature Communications **11**, 4431 (2020).

[41] Natalia G Berloff, Matteo Silva, Kirill Kalinin, Alexis Askitopoulos, Julian D Töpfer, Pasquale Cilibrizzi, Wolfgang Langbein, and Pavlos G Lagoudakis, Realizing the classical XY Hamiltonian in polariton simulators, Nature Materials **16**, 1120–1126 (2017).

[42] Pavlos G Lagoudakis and Natalia G Berloff, A polariton graph simulator, New Journal of Physics **19**, 125008 (2017).

[43] Kirill P. Kalinin and Natalia G. Berloff, Polaritonic network as a paradigm for dynamics of coupled oscillators, Phys. Rev. B **100**, 245306 (2019).

[44] Vladimir Garca-Morales and Katharina Krischer, The complex GinzburgLandau equation: An introduction, Contemporary Physics **53**, 79–95 (2012).

[45] Anton A. Selivanov, Judith Lehnert, Thomas Dahms, Philipp Hövel, Alexander L. Fradkov, and Eckehard Schöll, Adaptive synchronization in delay-coupled networks of Stuart-Landau oscillators, Phys. Rev. E **85**, 016201 (2012).

[46] Hongjie Bi, Xin Hu, Xiyun Zhang, Yong Zou, Zonghua Liu, and Shuguang Guan, Explosive oscillation death in coupled Stuart-Landau oscillators, EPL (Europhysics Letters) **108**, 50003 (2014).

[47] K. Sathiyadevi, V. K. Chandrasekar, and D. V. Senthilkumar, Stable amplitude chimera in a network of coupled Stuart-Landau oscillators, Phys. Rev. E **98**, 032301 (2018).

[48] Matthew Bennett, Michael F Schatz, Heidi Rockwood, and Kurt Wiesenfeld, Huygens's clocks, Proceedings of the Royal Society of London. Series A: Mathematical, Physical and Engineering Sciences **458**, 563–579 (2002).

[49] James Pantaleone, Synchronization of metronomes, American Journal of Physics **70**, 992–1000 (2002).

[50] Andr Rhm, Kathy Ldge, and Isabelle Schneider, Bistability in two simple symmetrically coupled oscillators with symmetry-broken amplitude- and phase-locking, Chaos: An Interdisciplinary Journal of Nonlinear Science **28**, 063114 (2018).

[51] Lucia Valentina Gambuzza, Jesus Gómez-Gardeñes, and Mattia Frasca, Amplitude dynamics favors synchronization in complex networks, Scientific reports **6**, 1–9 (2016).

[52] Juan A. Acebrón, L. L. Bonilla, Conrad J. Pérez Vicente, Félix Ritort, and Renato Spigler, The Kuramoto model: A simple paradigm for synchronization phenomena, Rev. Mod. Phys. **77**, 137–185 (2005).

[53] Yoshiki Kuramoto, *Chemical Oscillations, Waves, and Turbulence* (Springer-Verlag, Berlin Heidelberg, 1984).

[54] Steven H. Strogatz, From Kuramoto to Crawford: exploring the onset of synchronization in populations of coupled oscillators, Physica D: Nonlinear Phenomena **143**, 1 – 20 (2000).

[55] Michael C Mackey and Leon Glass, Oscillation and chaos in physiological control systems, Science **197**, 287–289 (1977).

[56] Heinz Georg Schuster and Peter Wagner, Mutual entrainment of two limit cycle oscillators with time delayed coupling, Progress of Theoretical Physics **81**, 939–945 (1989).

[57] Awadhesh Prasad, Amplitude death in coupled chaotic oscillators, Phys. Rev. E **72**, 056204 (2005).

[58] Awadhesh Prasad, Jürgen Kurths, Syamal Kumar Dana, and Ramakrishna Ramaswamy, Phase-flip bifurcation induced by time delay, Phys. Rev. E **74**, 035204 (2006).

[59] Laurent Larger, Bogdan Penkovsky, and Yuri Maistrenko, Virtual chimera states for delayed-feedback systems, Phys. Rev. Lett. **111**, 054103 (2013).

[60] Otti DHuys, Raul Vicente, Thomas Erneux, Jan Danckaert, and Ingo Fischer, Synchronization properties of network motifs: Influence of coupling delay and symmetry, Chaos: An Interdisciplinary Journal of Nonlinear Science **18**, 037116 (2008).

[61] Kerry J Vahala, Optical microcavities, Nature **424**, 839–846 (2003).

[62] Claus F Klingshirn, *Semiconductor optics* (Springer-Verlag, Berlin Heidelberg, 2012).

[63] Dirk Van Delft and Peter Kes, The discovery of superconductivity, Physics Today **63**, 38–43 (2010).

[64] Oliver Penrose and Lars Onsager, Bose-Einstein condensation and liquid helium, Physical Review **104**, 576 (1956).

[65] Chen Ning Yang, Concept of off-diagonal long-range order and the quantum phases of liquid he and of superconductors, Reviews of Modern Physics **34**, 694 (1962).

[66] Anthony J. Leggett, Bose-Einstein condensation in the alkali gases: Some fundamental concepts, Rev. Mod. Phys. **73**, 307–356 (2001).

[67] M. Naraschewski and R. J. Glauber, Spatial coherence and density correlations of trapped Bose gases, Phys. Rev. A **59**, 4595–4607 (1999).

[68] Tobias Donner, Stephan Ritter, Thomas Bourdel, Anton Öttl, Michael Köhl, and Tilman Esslinger, Critical behavior of a trapped interacting Bose gas, Science **315**, 1556–1558 (2007).

[69] Dallin S Durfee and Wolfgang Ketterle, Experimental studies of Bose-Einstein condensation, Optics Express **2**, 299–313 (1998).

[70] Zoran Hadzibabic, Peter Krüger, Marc Cheneau, Baptiste Battelier, and Jean Dalibard, Berezinskii–Kosterlitz–Thouless crossover in a trapped atomic gas, Nature **441**, 1118–1121 (2006).

[71] Hui Deng, Glenn S. Solomon, Rudolf Hey, Klaus H. Ploog, and Yoshihisa Yamamoto, Spatial coherence of a polariton condensate, Phys. Rev. Lett. **99**, 126403 (2007).

[72] R Balili, V Hartwell, D Snoke, L Pfeiffer, and K West, Bose-Einstein condensation of microcavity polaritons in a trap, Science **316**, 1007–1010 (2007).

[73] Maxime Richard, Jacek Kasprzak, Robert Romestain, Régis André, and Le Si Dang, Spontaneous coherent phase transition of polaritons in CdTe microcavities, Phys. Rev. Lett. **94**, 187401 (2005).

[74] F. Tassone, C. Piermarocchi, V. Savona, A. Quattropani, and P. Schwendimann, Bottleneck effects in the relaxation and photoluminescence of microcavity polaritons, Phys. Rev. B **56**, 7554–7563 (1997).

[75] Esther Wertz, Lydie Ferrier, Dmitry D Solnyshkov, Pascale Senellart, Daniele Bajoni, Audrey Miard, Aristide Lemaître, Guillaume Malpuech, and Jacqueline Bloch, Spontaneous formation of a polariton condensate in a planar gaas microcavity, Applied Physics Letters **95**, 051108 (2009).

[76] Yongbao Sun, Patrick Wen, Yoseob Yoon, Gangqiang Liu, Mark Steger, Loren N. Pfeiffer, Ken West, David W. Snoke, and Keith A. Nelson, Bose-Einstein Condensation of long-lifetime polaritons in thermal equilibrium, Phys. Rev. Lett. **118**, 016602 (2017).

[77] P. R. Eastham, Mode locking and mode competition in a nonequilibrium solid-state condensate, Phys. Rev. B **78**, 035319 (2008).

[78] Julian D Töpfer, Helgi Sigurdsson, Lucinda Pickup, and Pavlos G Lagoudakis, Time-delay polaritonics, Communications Physics **3**, 2 (2020).

[79] E. Estrecho, T. Gao, N. Bobrovska, D. Comber-Todd, M. D. Fraser, M. Steger, K. West, L. N. Pfeiffer, J. Levinsen, M. M. Parish, T. C. H. Liew, M. Matuszewski, D. W. Snoke, A. G. Truscott, and E. A. Ostrovskaya, Direct measurement of polariton-polariton interaction strength in the Thomas-Fermi regime of exciton-polariton condensation, Phys. Rev. B **100**, 035306 (2019).

[80] Nikolai B Kopnin, Introduction to Ginzburg-Landau and Gross-Pitaevskii theories for superconductors and superfluids, Journal of low temperature physics **129**, 219–262 (2002).

[81] Michiel Wouters and Iacopo Carusotto, Excitations in a nonequilibrium Bose-Einstein condensate of exciton polaritons, Phys. Rev. Lett. **99**, 140402 (2007).

[82] Joseph W Goodman, *Statistical optics* (John Wiley & Sons, Hoboken, New Jersey, 2015).

[83] Joanna M. Zajac, Wolfgang Langbein, Maxime Hugues, and Mark Hopkinson, Polariton states bound to defects in GaAs/AlAs planar microcavities, Phys. Rev. B **85**, 165309 (2012).

[84] Joanna M. Zajac, Edmund Clarke, and Wolfgang Langbein, Suppression of cross-hatched polariton disorder in GaAs/AlAs microcavities by strain compensation, Applied Physics Letters **101**, 041114 (2012).

[85] Pasquale Cilibrizzi, Alexis Askitopoulos, Matteo Silva, Faebian Bastiman, Edmund Clarke, Joanna M. Zajac, Wolfgang Langbein, and Pavlos G. Lagoudakis, Polariton condensation in a strain-compensated planar microcavity with ingaas quantum wells, Applied Physics Letters **105**, 191118 (2014).

[86] RW Gerchberg and WO Saxton, A practical algorithm for the determination of phase from image and diffraction plane pictures, Optik **35**, 237–246 (1972).

[87] F. Nogrette, H. Labuhn, S. Ravets, D. Barredo, L. Béguin, A. Vernier, T. Lahaye, and A. Browaeys, Single-atom trapping in holographic 2d arrays of microtraps with arbitrary geometries, Phys. Rev. X **4**, 021034 (2014).

[88] Hikaru Tamura, Tomoyuki Unakami, Jun He, Yoko Miyamoto, and Ken'ichi Nakagawa, Highly uniform holographic microtrap arrays for single atom trapping using a feedback optimization of in-trap fluorescence measurements, Opt. Express **24**, 8132–8141 (2016).

[89] J. D. Töpfer, I. Chatzopoulos, H. Sigurdsson, T. Cookson, Y. G. Rubo, and P. G. Lagoudakis, Engineering spatial coherence in lattices of polariton condensates, Optica **8**, 106–113 (2021).

[90] S. Alyatkin, J. D. Töpfer, A. Askitopoulos, H. Sigurdsson, and P. G. Lagoudakis, Optical control of couplings in polariton condensate lattices, Phys. Rev. Lett. **124**, 207402 (2020).

[91] Gregory P. Lousberg, Lars D. Lundeberg, Dmitri L. Boiko, and Eli Kapon, Space-domain lock-in amplifier based on a liquid-crystal spatial light modulator, Opt. Lett. **31**, 990–992 (2006).

[92] Thomas Erneux, *Applied delay differential equations*, Vol. 3 (Springer Science & Business Media, New York, 2009).

[93] Michiel Wouters, Iacopo Carusotto, and Cristiano Ciuti, Spatial and spectral shape of inhomogeneous nonequilibrium exciton-polariton condensates, Phys. Rev. B **77**, 115340 (2008).

[94] M. Wouters, T. C. H. Liew, and V. Savona, Energy relaxation in one-dimensional polariton condensates, Phys. Rev. B **82**, 245315 (2010).

[95] Immanuel Bloch, Ultracold quantum gases in optical lattices, Nature Physics **1**, 23–30 (2005).

[96] FS Cataliotti, Sven Burger, C Fort, P Maddaloni, Francesco Minardi, Andrea Trombettoni, Augusto Smerzi, and M Inguscio, Josephson junction arrays with Bose-Einstein condensates, Science **293**, 843–846 (2001).

[97] David Dung, Christian Kurtscheid, Tobias Damm, Julian Schmitt, Frank Vewinger, Martin Weitz, and Jan Klaers, Variable potentials for thermalized light and coupled condensates, Nature Photonics **11**, 565 (2017).

[98] Miguel C. Soriano, Jordi García-Ojalvo, Claudio R. Mirasso, and Ingo Fischer, Complex photonics: Dynamics and applications of delay-coupled semiconductors lasers, Rev. Mod. Phys. **85**, 421–470 (2013).

[99] Gabriel Christmann, Guilherme Tosi, Natalia G Berloff, Panagiotis Tsotsis, Peter S Eldridge, Zacharias Hatzopoulos, Pavlos G Savvidis, and Jeremy J Baumberg, Oscillatory solitons and time-resolved phase locking of two polariton condensates, New Journal of Physics **16**, 103039 (2014).

[100] H. Ohadi, R. L. Gregory, T. Freegarde, Y. G. Rubo, A. V. Kavokin, N. G. Berloff, and P. G. Lagoudakis, Nontrivial phase coupling in polariton multiplets, Phys. Rev. X **6**, 031032 (2016).

[101] Kirill P Kalinin and Natalia G Berloff, Networks of non-equilibrium condensates for global optimization, New Journal of Physics **20**, 113023 (2018).

[102] Roy Lang and Kohroh Kobayashi, External optical feedback effects on semiconductor injection laser properties, IEEE journal of Quantum Electronics **16**, 347–355 (1980).

[103] G. Kozyreff, A. G. Vladimirov, and Paul Mandel, Global coupling with time delay in an array of semiconductor lasers, Phys. Rev. Lett. **85**, 3809–3812 (2000).

[104] Awadhesh Prasad, Syamal Kumar Dana, Rajat Karnatak, Jürgen Kurths, Bernd Blasius, and Ramakrishna Ramaswamy, Universal occurrence of the phase-flip bifurcation in time-delay coupled systems, Chaos: An Interdisciplinary Journal of Nonlinear Science **18**, 023111 (2008).

[105] Atsuko Takamatsu, Teruo Fujii, and Isao Endo, Time delay effect in a living coupled oscillator system with the plasmodium of physarum polycephalum, Phys. Rev. Lett. **85**, 2026–2029 (2000).

[106] J. M. Cruz, J. Escalona, P. Parmananda, R. Karnatak, A. Prasad, and R. Ramaswamy, Phase-flip transition in coupled electrochemical cells, Phys. Rev. E **81**, 046213 (2010).

[107] Krishna Manoj, Samadhan A Pawar, and RI Sujith, Experimental evidence of amplitude death and phase-flip bifurcation between in-phase and anti-phase synchronization, Scientific reports **8**, 11626 (2018).

[108] E. del Valle, D. Sanvitto, A. Amo, F. P. Laussy, R. André, C. Tejedor, and L. Viña, Dynamics of the formation and decay of coherence in a polariton condensate, Phys. Rev. Lett. **103**, 096404 (2009).

[109] G. Nardin, K. G. Lagoudakis, M. Wouters, M. Richard, A. Baas, R. André, Le Si Dang, B. Pietka, and B. Deveaud-Plédran, Dynamics of long-range ordering in an exciton-polariton condensate, Phys. Rev. Lett. **103**, 256402 (2009).

[110] V. V. Belykh, N. N. Sibeldin, V. D. Kulakovskii, M. M. Glazov, M. A. Semina, C. Schneider, S. Höfling, M. Kamp, and A. Forchel, Coherence expansion and

polariton condensate formation in a semiconductor microcavity, Phys. Rev. Lett. **110**, 137402 (2013).

[111] Marta Galbiati, Lydie Ferrier, Dmitry D. Solnyshkov, Dimitrii Tanese, Esther Wertz, Alberto Amo, Marco Abbarchi, Pascale Senellart, Isabelle Sagnes, Aristide Lemaître, Elisabeth Galopin, Guillaume Malpuech, and Jacqueline Bloch, Polariton condensation in photonic molecules, Phys. Rev. Lett. **108**, 126403 (2012).

[112] Lennert Appeltant, Miguel Cornelles Soriano, Guy Van der Sande, Jan Danckaert, Serge Massar, Joni Dambre, Benjamin Schrauwen, Claudio R Mirasso, and Ingo Fischer, Information processing using a single dynamical node as complex system, Nature Communications **2**, 468 (2011).

[113] Daniel Brunner, Miguel C Soriano, Claudio R Mirasso, and Ingo Fischer, Parallel photonic information processing at gigabyte per second data rates using transient states, Nature Communications **4**, 1364 (2013).

[114] Laurent Larger, Antonio Baylón-Fuentes, Romain Martinenghi, Vladimir S. Udaltsov, Yanne K. Chembo, and Maxime Jacquot, High-speed photonic reservoir computing using a time-delay-based architecture: Million words per second classification, Phys. Rev. X **7**, 011015 (2017).

[115] Duncan J Watts and Steven H Strogatz, Collective dynamics of small-worldnetworks, Nature **393**, 440–442 (1998).

[116] Adilson E Motter, Seth A Myers, Marian Anghel, and Takashi Nishikawa, Spontaneous synchrony in power-grid networks, Nature Physics **9**, 191–197 (2013).

[117] Miguel Romera, Philippe Talatchian, Sumito Tsunegi, Flavio Abreu Araujo, Vincent Cros, Paolo Bortolotti, Juan Trastoy, Kay Yakushiji, Akio Fukushima, Hitoshi Kubota, *et al.*, Vowel recognition with four coupled spin-torque nano-oscillators, Nature **563**, 230–234 (2018).

[118] Tsung-Yu Kao, John L Reno, and Qing Hu, Phase-locked laser arrays through global antenna mutual coupling, Nature Photonics **10**, 541–546 (2016).

[119] Julian Struck, Christoph Ölschläger, R Le Targat, Parvis Soltan-Panahi, André Eckardt, Maciej Lewenstein, Patrick Windpassinger, and Klaus Sengstock, Quantum simulation of frustrated classical magnetism in triangular optical lattices, Science **333**, 996–999 (2011).

[120] Alberto Amo and Jacqueline Bloch, Exciton-polaritons in lattices: A non-linear photonic simulator, Comptes Rendus Physique **17**, 934–945 (2016).

[121] H. Ohadi, Y. del Valle-Inclan Redondo, A. J. Ramsay, Z. Hatzopoulos, T. C. H. Liew, P. R. Eastham, P. G. Savvidis, and J. J. Baumberg, Synchronization crossover

of polariton condensates in weakly disordered lattices, Phys. Rev. B **97**, 195109 (2018).

[122] Simon Mahler, Matthew L. Goh, Chene Tradonsky, Asher A. Friesem, and Nir Davidson, Improved phase locking of laser arrays with nonlinear coupling, Phys. Rev. Lett. **124**, 133901 (2020).

[123] T. Gao, E. Estrecho, G. Li, O. A. Egorov, X. Ma, K. Winkler, M. Kamp, C. Schneider, S. Höfling, A. G. Truscott, and E. A. Ostrovskaya, Talbot effect for exciton polaritons, Phys. Rev. Lett. **117**, 097403 (2016).

[124] Michiel Wouters and Vincenzo Savona, Stochastic classical field model for polariton condensates, Phys. Rev. B **79**, 165302 (2009).

[125] Johannes Schmutzler, Tomasz Kazimierczuk, Ömer Bayraktar, Marc Aßmann, Manfred Bayer, Sebastian Brodbeck, Martin Kamp, Christian Schneider, and Sven Höfling, Influence of interactions with noncondensed particles on the coherence of a one-dimensional polariton condensate, Phys. Rev. B **89**, 115119 (2014).

[126] A. A. Demenev, Ya. V. Grishina, S. I. Novikov, V. D. Kulakovskii, C. Schneider, and S. Höfling, Loss of coherence in cavity-polariton condensates: Effect of disorder versus exciton reservoir, Phys. Rev. B **94**, 195302 (2016).

[127] Alexis Askitopoulos, Lucy Pickup, Sergey Alyatkin, Anton Zasedatelev, Konstantinos G Lagoudakis, Wolfgang Langbein, and Pavlos G Lagoudakis, Giant increase of temporal coherence in optically trapped polariton condensate, arXiv preprint arXiv:1911.08981 (2019).

[128] Harald Pier and Eli Kapon, Photon localization in lattices of coupled vertical-cavity surface-emitting lasers with dimensionalities between one and two, Optics letters **22**, 546–548 (1997).

[129] Mian Zhang, Shreyas Shah, Jaime Cardenas, and Michal Lipson, Synchronization and phase noise reduction in micromechanical oscillator arrays coupled through light, Phys. Rev. Lett. **115**, 163902 (2015).

[130] Moti Fridman, Micha Nixon, Nir Davidson, and Asher A Friesem, Passive phase locking of 25 fiber lasers, Optics letters **35**, 1434–1436 (2010).

[131] Micha Nixon, Eitan Ronen, Asher A. Friesem, and Nir Davidson, Observing geometric frustration with thousands of coupled lasers, Phys. Rev. Lett. **110**, 184102 (2013).

[132] Dario Ballarini, Milena De Giorgi, Emiliano Cancellieri, Romuald Houdré, Elisabeth Giacobino, Roberto Cingolani, Alberto Bramati, Giuseppe Gigli, and Daniele Sanvitto, All-optical polariton transistor, Nature Communications **4**, 1778 (2013).

[133] C Sturm, D Tanese, HS Nguyen, H Flayac, E Galopin, A Lemaître, I Sagnes, D Solnyshkov, A Amo, G Malpuech, *et al.*, All-optical phase modulation in a cavity-polariton Mach–Zehnder interferometer, Nature Communications **5**, 3278 (2014).

[134] Félix Marsault, Hai Son Nguyen, Dimitrii Tanese, Aristide Lemaître, Elisabeth Galopin, Isabelle Sagnes, Alberto Amo, and Jacqueline Bloch, Realization of an all optical exciton-polariton router, Applied Physics Letters **107**, 201115 (2015).

[135] H. Ohadi, A. J. Ramsay, H. Sigurdsson, Y. del Valle-Inclan Redondo, S. I. Tsintzos, Z. Hatzopoulos, T. C. H. Liew, I. A. Shelykh, Y. G. Rubo, P. G. Savvidis, and J. J. Baumberg, Spin order and phase transitions in chains of polariton condensates, Phys. Rev. Lett. **119**, 067401 (2017).

[136] T. Cookson, K. P. Kalinin, H. Sigurdsson, J. D. Töpfer, S. Alyatkin, M. Silva, W.Langbein, N. G. Berloff, and P. G. Lagoudakis, Geometric frustration in polygons of polariton condensates creating vortices of varying topological charge, Nature Communications **12**, 2120 (2021).

[137] T. Gao, P. S. Eldridge, T. C. H. Liew, S. I. Tsintzos, G. Stavrinidis, G. Deligeorgis, Z. Hatzopoulos, and P. G. Savvidis, Polariton condensate transistor switch, Phys. Rev. B **85**, 235102 (2012).

[138] D Sanvitto, S Pigeon, A Amo, D Ballarini, M De Giorgi, I Carusotto, R Hivet, F Pisanello, VG Sala, PSS Guimaraes, *et al.*, All-optical control of the quantum flow of a polariton condensate, Nature Photonics **5**, 610–614 (2011).

[139] Mark J Panaggio and Daniel M Abrams, Chimera states: coexistence of coherence and incoherence in networks of coupled oscillators, Nonlinearity **28**, R67 (2015).

[140] Chol-Ung Choe, Thomas Dahms, Philipp Hövel, and Eckehard Schöll, Controlling synchrony by delay coupling in networks: From in-phase to splay and cluster states, Phys. Rev. E **81**, 025205 (2010).

[141] Anton A. Selivanov, Judith Lehnert, Thomas Dahms, Philipp Hövel, Alexander L. Fradkov, and Eckehard Schöll, Adaptive synchronization in delay-coupled networks of stuart-landau oscillators, Phys. Rev. E **85**, 016201 (2012).

[142] Esther Wertz, Lydie Ferrier, DD Solnyshkov, Robert Johne, Daniele Sanvitto, Aristide Lemaître, Isabelle Sagnes, Roger Grousson, Alexey V Kavokin, Pascale Senellart, *et al.*, Spontaneous formation and optical manipulation of extended polariton condensates, Nature Physics **6**, 860–864 (2010).

[143] A. Askitopoulos, H. Ohadi, A. V. Kavokin, Z. Hatzopoulos, P. G. Savvidis, and P. G. Lagoudakis, Polariton condensation in an optically induced two-dimensional potential, Phys. Rev. B **88**, 041308 (2013).

[144] J. D. Töpfer, H. Sigurdsson, S. Alyatkin, and P. G. Lagoudakis, Lotka-volterra population dynamics in coherent and tunable oscillators of trapped polariton condensates, Phys. Rev. B **102**, 195428 (2020).

[145] Dario Ballarini, Davide Caputo, Carlos Sánchez Muñoz, Milena De Giorgi, Lorenzo Dominici, Marzena H. Szymańska, Kenneth West, Loren N. Pfeiffer, Giuseppe Gigli, Fabrice P. Laussy, and Daniele Sanvitto, Macroscopic two-dimensional polariton condensates, Phys. Rev. Lett. **118**, 215301 (2017).

[146] T. C. H. Liew, A. V. Kavokin, and I. A. Shelykh, Optical circuits based on polariton neurons in semiconductor microcavities, Phys. Rev. Lett. **101**, 016402 (2008).